Energy cascade analysis in a viscoelastic turbulent flow

António Pedro Fernandes Caeiro Mósca

Thesis to obtain the Master of Science Degree in

Mechanical Engineering

Examination Committee

Chairperson: Prof. Luis Rego da Cunha Eça
Supervisor: Prof. Carlos Frederico Neves Bettencourt da Silva
Co-supervisor: Prof. José Carlos Fernandes Pereira
Member of the Committee: Prof. Viriato Sérgio de Almeida Semião

November 2012

Acknowledgments

I would like to start thanking to several people that were crucial to this thesis:

- Professor Carlos Silva and Professor José Carlos Pereira, for giving me such an opportunity to work in this area. Also for their availability to explain everything again and again and for teaching me so many interesting things
- Professor Fernando Pinho, for following my learning process so well and for the very important discussions that clarified so many things
- All LASEF workers, specially to Ricardo Marques with whom I worked closer
- All my colleagues at IST
- Friends
- Last but not the least, to my family, Manuel, Cristina and João, whom I would like to devote this work

Abstract

Direct numerical simulations (DNS) of homogeneous and isotropic turbulence in a viscoelastic fluid are done in order to study the kinetic energy transfers and the structures of the correspondent turbulent field, in both physical and Fourier spaces. The numerical algorithm is based on pseudo-spectral methods and the rheology of the fluid is represented by using the finitely extensible non-linear elastic rheological constitutive model with Peterlin approximation (FENE-P). The energy cascade is studied by analysing the energy transfer between large and small flow scales in different zones of the energy spectrum. The separation between scales is done using filtering operations in the physical space and the results are analysed using statistical tools. With the results obtained is possible to plan how to do LES of viscoelastic turbulent flows.

Keywords

Viscoelastic turbulence, energy cascade, isotropic turbulence, DNS, FENE-P

Resumo

Simulações numéricas directas (direct numerical simulation - DNS) de turbulência homogénea e isotrópica num fluido viscoelástico são levadas a cabo para estudar as transferências de energia cinética turbulenta e as estruturas do campo turbulento associado, no espaço físico e no espaço de Fourier. O algoritmo numérico assenta no uso de métodos pseudo-espectrais e a reologia do fluido é modelada usando o modelo constitutivo reológico de extensibilidade elástica finita não linear na variante de Peterlin (FENE-P do inglês 'Finitely extensible nonlinear elastic-Peterlin'). A cascata de energia é estudada analisando a transferência de energia entre as grandes e as pequenas escalas do escoamento em diferentes zonas do espectro de energia. A separação de escalas é conseguida usando operações de filtragem no espaço físico e os resultados são interpretados através de ferramentas estatísticas. Os resultados obtidos permitem delinear estratégias para a simulação das grandes escalas (large-eddy simulation - LES) de escoamentos turbulentos viscoelásticos.

Palavras Chave

Turbulência Viscoelástica, cascata de energia, turbulência isotrópica, DNS, FENE-P

Contents

List of Figures

List of Tables

List of Symbols

Acronyms

2D	two dimensions, two-dimensional
3D	three dimensions, three-dimensional
DHIT	Decaying Homogeneous Isotropic Turbulence
DNS	Direct Numerical Simulation
DR	Drag Reduction
EDP	Energy Decay Period
EPP	Energy Propagation Period
FENE	Finitely Extensible Non-linear Elastic
FENE-P	Finitely Extensible Non-linear Elastic with Peterlin approximation
FCT	Fundação para a Ciência e Tecnologia
FHIT	Forced Homogeneous Isotropic Turbulence
FFT	Fast Fourier Transform
GS	Grid-Scale
HIT	Homogeneous Isotropic Turbulence
KT	Kurganov-Tadmor
LES	Large Eddy Simulation
MDR	Maximum Drag Reduction
PDE	Partial Differential Equation

PDF	Probability Density Function
ppm	parts per million
RACE	Reynolds-Average Constitutive Equation
RANS	Reynolds-Average Navier-Stokes
SGS	Subgrid-Scale
SPD	Symmetric Positive Definite
TURBELAST	Turbulence modelling for viscoelastic fluids

Math operators

$\langle a \rangle$	Average of a
a'	Fluctuation of a
i	Imaginary unit
$\nabla\cdot$	Divergence operator
$\nabla\times$	Rotational operator
$\frac{D}{Dt}$	Material derivative
$\frac{\partial}{\partial x_i}$	Derivative with respect to coordinate x_i
$\frac{\partial}{\partial t}$	Derivative with respect to time
$\ln$	Natural logarithm
$\star$	Convolution product
$*$	Complex conjugate
$\bar{\phi}$	Filtered variable
$\mathcal{F}$	Direct Fourier transform
$\mathcal{F}^{-1}$	Inverse Fourier transform
$Tr(\mathbf{C})$	Trace of the Conformation tensor

Alphanumeric symbols

C	Generic constant
$\mathbf{C}$	Conformation tensor
C_{ij}	Component i, j of the Conformation tensor
$C_{(X,Y)}$	Correlation coefficient between X and Y
D	Pipe diameter
$E(k)$	Kinetic energy density function
f	Friction factor
$f(r)$	Peterlin function
f_f	Flatness factor
$\hat{G}_i$	Auxiliary function in the spectral space
$G_\Delta(x)$	Spatial filter
H	Unit of length used in the code
$\mathbf{H}$	Convective flux
k	Wave number
k_x, k_y, k_z	Wave number in the x, y, z direction
K	von Karman constant
l	Pipe length
L	Maximum polymer extension
$\mathbb{L}$	Spatial domain
L_x, L_y, L_z	Size of the computational domain in the x, y, z direction
N	Number of monomers in a polymer molecule
p	Pressure
q	End-to-end vector of the molecule

Qi	Second invariant of the velocity gradient tensor
Re	Reynolds number
$\mathbf{r}$	Configuration of the elastic dumbbell
r_i	Instantaneous orientation of the polymer dumbbell
r_{eq}	Equilibrium separation distance of the polymer dumbbell
s_f	Skewness factor
$\mathbf{S}$	Rate of strain tensor
S_{ij}	Component i, j of the rate of strain tensor
t	Time
$\mathbf{T}$	Stress tensor
T_{ij}	Component i, j of the stress tensor
$\mathbf{u}$	Velocity vector
u_i	Component i of the velocity vector
u	Instantaneous streamwise velocity
u^+, U^+	Dimensionless velocity (parallel to the wall)
U	Centreline velocity of the fully developed laminar flow
v	Instantaneous normal velocity
V	Generic term
w	Instantaneous spanwise velocity
We	Weissenberg number
$\mathbf{x}$	Position vector
x_i	Cartesian component i of the position
x, y, z	Cartesian component x, y, z of the position
y^+	Wall coordinate

Greek symbols

α_k, β_k	Runge-Kutta coefficients
β	Polymer concentration
δ	Channel half-height
δ_{ij}	Kronecker's delta
Δ	Filter width
Δx, Δy, Δz	Grid size in the x, y, z direction
Δt	Time step
ε	Energy dissipation rate
λ	Taylor microscale
λ_i	Eigenvalues of C_{ij}
λ_w	Wavelength
μ	Dynamic viscosity
ν	kinematic viscosity
ω	Vorticity vector
Ω	Enstrophy
ρ	Density
τ_{ij}	Subgrid-stress tensor
$\tau_{ijk}^{[p]}$	Subgrid-stress polymer tensor
τ_p	Zimm relaxation time of the polymer
ξ	Total turbulent kinetic energy

Superscripts symbols

$[0]$	Solvent and Polymer
k	Current sub-step
$k-1, k-2$	Last two sub-steps
n	Current step
$n-1$	Previous step
$[N]$	Newtonian case
$[p]$	Polymer
$[P]$	Viscoelastic case
$[s]$	Solvent

1

Introduction

Contents

In 1948, B. A. Toms (Toms [1]) discovered that the addition of small quantities of polymer to flowing liquids can produce profound effects on the flow phenomena. He also observed drag reductions of 30-40% upon adding only 10 *ppm* by weight of polymer (methylmethacrylate, in that case) (Diamond et al. [2], White and Mungal [3]).

Since this discovery made by Toms, there has been extensive and continuing research on the subject, because it has tremendous effects in many industrial applications as for e.g. pipe flows. Although the experiments show this effect, the details of the mechanism of polymer drag reduction still remain an enigma.

Advancements in understanding this phenomenon come largely from numerical simulations of viscoelastic turbulent flows and detailed turbulence measurements in flows of dilute polymer solutions using laser-based optical techniques.

Nowadays, in many industrial processes, it is possible to find viscoelastic fluids under turbulent flow conditions. Examples of such processes are the long distance transport of fluids and the heating and cooling systems, because the pumping costs are significantly reduced.

The investment in numerical tools and numerical simulations has been growing because their importance to solve real engineering problems has increased significantly in the last thirty years. Numerical techniques have been also crucial to a better understanding of viscoelastic fluids flows phenomena, mainly in the last decade. Due to this investment, recent advances have been done concerning turbulence models, rheological models, and others.

This thesis is part of a project funded by FCT (Fundação para a Ciência e Tecnologia) called ”TURBELAST - Turbulence modelling for viscoelastic fluids: RANS and LES approaches”. Extension of the existing RANS/RACE turbulence model to maximum DR, in particular the development of improved first and second order closures for the Reynolds stresses, of a closure to deal with turbulent scalar fluxes and the development of a new LES turbulence model for FENE-P fluids, the first of its kind, constitute the main objectives of this project. This thesis aims to contribute for the second aim identified above.

1.1 Motivation

It is estimated that 5% of all the energy spent in the world is due to wall turbulence!

This number is meaningful of the importance that Toms' discovery has. Since 1948, it is known that researchers study polymer drag reduction for both practical and fundamental purposes. Both fields have motivated a strong demand of knowledge.

Starting with the practical field, examples of industrial applications are pipe flows and marine vehicles.

Fundamentally, studying the effects of polymers on turbulence provides valuable insight into physics of fluid turbulence, particularly the self-sustaining mechanisms of wall turbulence. Moreover, if a detailed understanding of the mechanics of polymer drag reduction can be determined, it is conceivable that the effect can be reproduced by other means, such as surface modification, sensor actuation, or additives, among other strategies.

The work here presented aims to contribute to the understanding of the fundamentals. However, success on this front has tremendous impact on the economics of energy propulsion and pollutant emission reduction from vehicles. Ideally, research on polymer drag reduction should lead to improved and expanded practical applications and advance our understanding of fluid turbulence and turbulence control.

Numerical tools may have here special relevance because they appear as a powerful method to improve knowledge, with lower levels of effort comparing to experimental methods.

1.2 Objectives

The main objectives of the work here presented are:

1. to adapt a three-dimensional code in order to solve a viscoelastic turbulent flow:
   (a) to adapt a two-dimensional code so that it can solve a viscoelastic turbulent flow
   (b) to do the verification of this code against Couette flow analytical solution
   (c) to extend the 2D code to a 3D code
   (d) to do the verification of the new code ”in pseudo 2D”
   (e) to compare the results obtained with the 3D code with published results in decaying homogeneous isotropic turbulence
2. to study the physical mechanism of the energy cascade in isotropic turbulence in a viscoelastic fluid using DNS

1.3 Main contributions

As referred previously, this work has mainly fundamental purposes, development, analysis and understanding. Taking this into account, this work main contribution is the analysis of the energy cascade in isotropic turbulence in a viscoelastic fluid using DNS.

As the present thesis is integrated in the project ”TURBELAST - Turbulence modelling for viscoelastic fluids: RANS and LES approaches”, it has also a large contribution to its second main aim referred in the beginning of this chapter.

1.4 Dissertation outline

This document is organized according to the following chapters:

- Chapter 1: **Introduction**
    1. **Motivation**: what makes this work useful, interesting and with possible implications in a near future in the history of two poorly understood problems: turbulence and additives dynamics
    2. **Objectives**: the main objectives of this work are systematized
    3. **Main contributions**: how this work can be helpful in the future
    4. **Dissertation outline**: how this document is organized and what is the meaning of each chapter
- Chapter 2: **State of the art**: where all the progress (at least the most relevant) of the Toms phenomenon is presented in detail. The author chose to do a full revision of the state of the art (and not only the issues related with the matter studied in this work) in order to give a full scope of the advancements done in the several fields of fluid mechanics regarding polymer additives and turbulence
- Chapter 3: **Governing equations**
    1. **Velocity filed**: the Navier-Stokes equations are presented for the viscoelastic case
    2. **Constitutive model for the polymer**: the model used within this thesis is explained and the transport equation of the conformation tensor (tensor that represents the polymer configuration) is presented
    3. **Properties of the conformation tensor**: how the tensor can be interpreted is explained.
- Chapter 4: **Numerical methods and coding**: all the numerical tools and schemes implemented are explained in detail and the numeric instabilities are considered
- Chapter 5: **Verification and code to code comparison**: the two dimensional code is verified, the analytical solution of the Couette flow is used, and the results obtained with the three dimensional code for decaying homogeneous isotropic turbulence are compared with the literature
- Chapter 5: **Results**: this is the core of the thesis; the analysis of the energy cascade in a viscoelastic turbulent flow is presented in detail
- Chapter 6: **Conclusions**: besides the conclusions drawn in all the topics addressed within this thesis, proposals of future work are also presented

2

State of the art

Contents

The phenomenon of polymer-induced drag reduction was observed for the first time, accidentally during the second world war, almost simultaneously in the US and UK, as scientists were trying to experiment with gelled gasoline (Dimitropoulos et al. [4]). As the addition of macromolecules to low molecular weight solvents increases the viscosity in laminar flows, it was quite unexpected to find that in the presence of turbulence, the opposite can sometimes take place. However, due to the secrecy surrounding the war efforts, this phenomenon was not publicly announced till several years later, when it was independently rediscovered by the British chemist Toms. In fact, the phenomenon was baptised as Toms phenomenon. Toms phenomenon is defined as the effect of reduced drag in turbulent flows of a low concentration fibrous additive suspension, in comparison to the drag in turbulent flow of the solvent alone.

2.1 Experimental and theoretical methods

In the very beginning, just after the discovery, the experiments done to prove Toms' discovery failed either because of lack of experience in this kind of experiments or because of lack of knowledge in this issue. Since then, this topic is controversial, leading to different opinions among the specialists.

It was, firstly, concluded that the low concentration suspensions mostly show negligible effect in laminar flows (Diamond et al. [2], Sher and Hetsroni [5]). This became a universal fact after several experiments had been conducted and confirmed that there is almost no effect for laminar flows (see Figure 2.1).

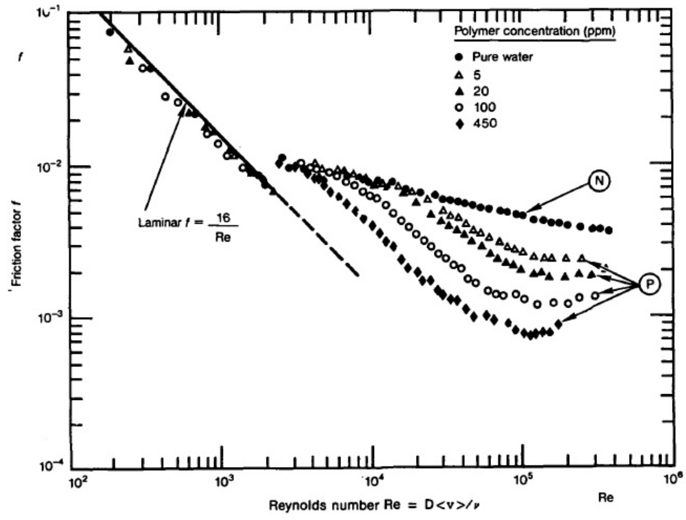

Figure 2.1: In 1992, a Moody Diagram (plot of the friction factor as function of Reynolds number for water flowing in a pipe) with several concentrations of polyethylene is presented, as a result obtained after conducting several experiments. The label "N" means with no polymer additives and the label "P" means with polymer additives with different concentrations. From Diamond et al. [2].

In Virk et al. [6], a deep investigation of the same effect in turbulent pipe flow of dilute[1] polymer additives was carried out. Virk et al. determined the main properties of Toms phenomenon which are: the existence of a universal maximum drag reduction (MDR) asymptote and the existence of an onset shear stress for drag reduction. The maximum drag reduction asymptote is observed in the velocity profile and in the friction flow rate domain. In spite of MDR asymptote was found to be universal, i.e. independent of system and additive properties, for some surfactant micellar solutions higher asymptotes have been observed (Gyr and Bewersdorff [7]). The onset shear stress, which is the minimal shear stress for the drag reduction effect to occur (as observed), was found by dimensional analysis based on some empirical observations to be related to the random-coiling effective diameter of the polymer additive.

Some years later, in 1975, Virk [8] compiled a large amount of experimental data on friction flow rate, onset shear stress, and velocity profile, and confirmed that these data are in agreement with the earlier proposed MDR asymptote and drag reduction onset shear stress relation. The data collected also allowed to draw some conclusions about the velocity profile of turbulent flow of polymer solutions: in the wall layer, the velocity profile seems to have two sub-regions, the ”elastic layer”, which exists above the viscous sub-layer, and the ”Newtonian plug”, which exists above the ”elastic layer” (Figures 2.2, 2.3 and 2.4). The ”elastic layer” has a logarithmic velocity profile with the slope of Virk’s maximum velocity profile, which is about 5 times the universal slope of the turbulent logarithmic profile (of a pure fluid). The ”Newtonian plug” has the universal slope logarithmic profile. The intersection point between these two sub-regions depends on flow and polymer additive properties.

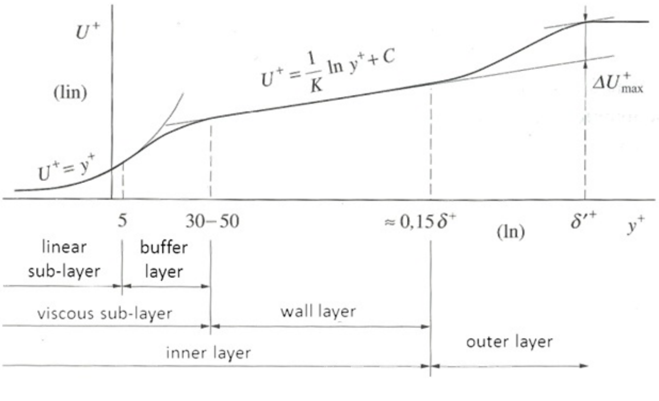

Figure 2.2: Turbulent boundary layer velocity profile for a Newtonian fluid. From Brederode [9].

Lumley, in the reviews of 1969 and 1977 (Lumley [10, 11]), said that in regions of the flow field where polymer molecules are elongated, viscosity is extremely enhanced. Lumley also postulated that: polymer molecules elongation is due to strain flow (the elongation flow component)

---

[1] Polymers are assumed to be sufficiently diluted to neglect the hydrodynamic interactions between neighbouring macro-molecules.

and vorticity diminishes polymer elongation because it reduces the relative time that the elongated polymer is aligned with the principal axis of the strain field. He further concluded that, in highly turbulent flow regions, as vorticity and strain flow rate are not correlated, stretched polymer molecules would be found in the wall layer, but not in the viscous sub-layer.

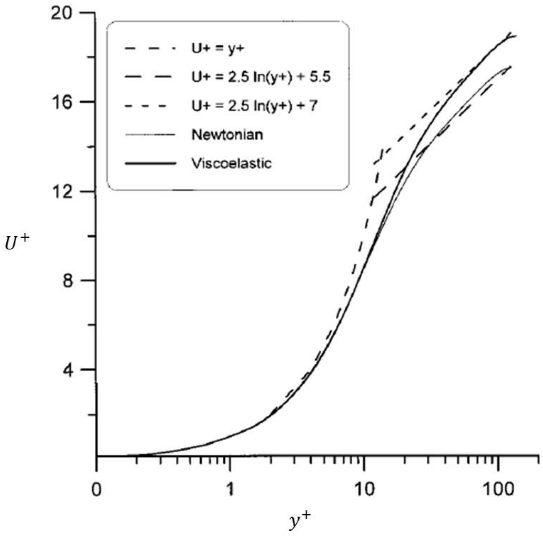

Figure 2.3: Turbulent boundary layer velocity profile for Newtonian and viscoelastic fluids. Also shown are the linear sub-layer ($U^+ = y^+$) and the wall layer ($U^+ = 2.5ln(y^+) + 5.5$) asymptotes for the Newtonian flow and a logarithmic profile, $U^+ = 2.5ln(y^+) + 7$, to fit the viscoelastic "Newtonian plug" profile. From Sureshkumar et al. [12].

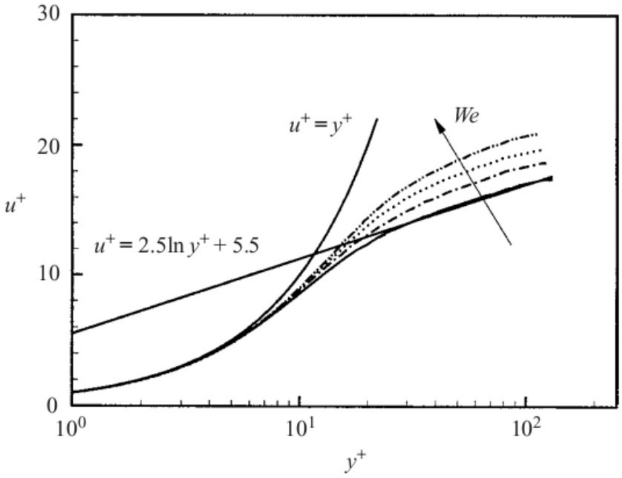

Figure 2.4: Turbulent boundary layer velocity profile for Newtonian and viscoelastic fluids. $\mathrm{Re} = 3000$ (____, Newtonian; _ _, $\mathrm{We} = 1$; _ . _, $\mathrm{We} = 2$; ...., $\mathrm{We} = 3$; _ . . _, $\mathrm{We} = 4$). The Reynolds number is given by $\mathrm{Re} = \frac{U\delta}{\nu^{[0]}}$, where U is the centreline velocity of the fully developed laminar flow, δ is the channel half-height and $\nu^{[0]}$ is the kinematic viscosity of the solution. The Weissenberg number is defined as $\mathrm{We} = \frac{\tau_p U}{\delta}$, where τ_p is the polymer relaxation time. From Min et al. [13].

Hence, increased viscosity will occur only in the wall layer, enhancing dissipation of turbulent fluctuations, leading to suppression of turbulent stresses. By this mechanism Lumley qualitatively explained the MDR phenomenon as a feedback saturation effect of turbulence causing polymer molecules to stretch (see Figure 2.5), which in turn suppress turbulence. He also defined a time scale ratio of eddies to polymer relaxation, to determine a threshold limit of the mechanism, which he associated with the onset phenomenon. Polymer relaxation time was estimated in this model as the first Zimm relaxation time (Zimm [14]).

De Gennes [15] proposed a model based on elasticity properties of the solute polymers, instead of viscosity effects as in Lumley's model. In De Gennes' model, turbulence is suppressed by elastic absorption of moderately stretched polymer molecules. He postulated that polymer elongation should be proportional to a power law of a length scale ratio, which is respective to Lumley's time scale ratio. This postulation enabled him to calculate the elastic stress in the polymer, by Pincus [16] theory, as a function of the turbulence length scale. By that he defined a threshold length scale of turbulence, as the point where turbulent stress equals elastic stress in the polymer. He argued that flow affects (stretches) polymer at length scales smaller than that respective to Lumley's time scale, but polymer affects flow at even smaller length scales, smaller than his newly defined threshold. He discussed some scenarios considering the stretching extent, and stated that his model is more appropriate for moderate stretching, whereas Lumley's model is more appropriate for full stretching.

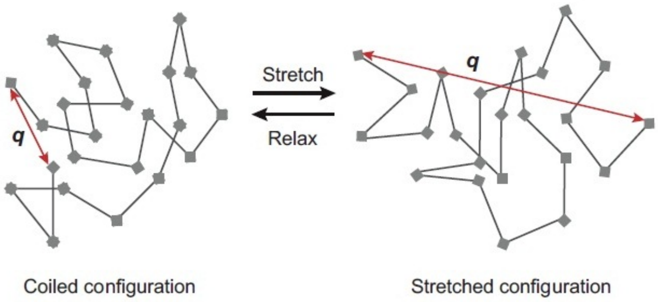

Figure 2.5: Schematic of polymer stretch (and relaxation). Polymer stretch is characterized by the change in q, which is the end-to-end vector of the molecule. From White and Mungal [3].

Sreenivasan and White [17] utilized De Gennes' descriptive model to calculate onset shear stress. They associated the onset point as a condition in which the De Gennes' threshold length scale is reached at the buffer layer, between the linear sub-layer and the wall layer. They used the elongation power law as a best-fit parameter, and obtained plausible predictions. In addition, they extended De Gennes' model to evaluate conditions for MDR to be reached (Figure 2.6). They made use of the assumption that MDR is achieved when, among other conditions, polymer concentration reaches the dilute solution limit (polymer molecules start to overlap). By further assuming that the De Gennes' threshold length scale based Reynolds number can be expressed as a power law of the friction based Reynolds number, and by letting this power to be a best-fit determined parameter, reasonable predictions for MDR conditions are shown. However, the extent of drag reduction is not evaluated by this theory, nor is by Lumley's.

Landahl [18] developed a two-scale mechanistic model of turbulence based on the classical hydrodynamic stability concept. He argued that shearing of large scale eddies by the mean flow can cause an inflection in the local velocity profile, leading to small scale instability, which in turn can further develop into a bursting event. According to his model, additive drag reduction is mainly due to inhibition (stabilization) of this instability mechanism by aligned elongated molecules, which lowers turbulent production. Based on constitutive rheological relations of fiber suspensions, the model offers explanations for onset and MDR conditions.

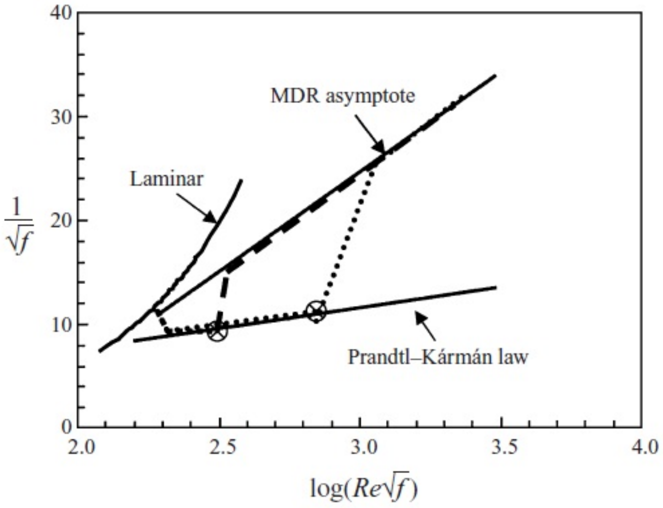

Figure 2.6: Schematic illustrating the onset of drag reduction and the maximum drag-reduction asymptote. The coordinates are those used in standard plots of pressure drop in pipe flows. The so-called Prandtl-Kármán law corresponds to the turbulent flow of Newtonian fluids. The dotted and dashed lines represent qualitatively the friction factor behaviour when a small amount of polymer is mixed with the fluid. The dashed line is for a larger polymer concentration. The line marked MDR asymptote represents the empirically observed limit on polymer drag reduction (Virk [8]). The Reynolds number and the friction factor are defined as follows: $\mathrm{Re} = \frac{2U\delta}{\nu^{[0]}}$ and $f = \frac{\Delta p}{\rho U^2}\frac{\delta}{l}$, in which δ and l are, respectively, the radius and the length of the pipe. From White and Mungal [3], Sreenivasan and White [17].

L'vov et al. [19] developed a boundary layer turbulent model, based on a momentum balance, and an approximated turbulent energy equation. The momentum balance is between viscous shearing stress, Reynolds stress, and pressure. The energy equation is a balance between turbulent energy production, and its estimated dissipation. By defining a constant ratio of Reynolds stress to turbulent kinetic energy, a logarithmic velocity profile is obtained. Experimental evidence of a logarithmic profile in the "elastic layer" suggests that this ratio should be constant for a polymer solution as well, but should assume a different empirical value in the elastic region, to match its different slope. A further *ad hoc* statement of a linear profiled effective viscosity leads to good results in numerical simulations and in calculation of the intersection point between the ”elastic layer” and the ”Newtonian plug” (De Angelis et al. [20], Benzi et al. [21]).

Maximum effective viscosity was related to polymer concentration, monomer size, and degree of polymerization, by Stokes law for a fully stretched polymer (Benzi et al. [21]). Attempts have also been made to account for the Toms’ phenomenon by means of a constitutive equation for the polymeric solution.

Hansen [22] studied transient laminar flow near a flat plate, treating the polymer solution as a continuum characterized by a constitutive equation of the Maxwell model (in which shear stress depends on shear stress rate in addition to its Newtonian shear rate dependency). He obtained theoretical results that showed lowered drag in comparison to a purely Newtonian fluid, which he associated with turbulent drag reduction (through a simple model of turbulence).

Ryskin [23] scaled relative drag reduction with effective viscosity increase, which was estimated from his ”yo-yo” model of unravelling polymer in an extensional flow. His predictions were in general agreement with Virk.

2.2 Numerical methods

Over the past 15 years, direct numerical simulation (DNS) has played an increasingly important role in the investigation of turbulent drag reduction by polymer additives, particularly for wall-bounded turbulent flows. DNS has the advantage over laboratory experiments of describing the orientation of the polymer microstructure in addition to the velocity field and Reynolds stresses.

An example study is that of Den Toonder et al. [24] who performed a DNS of polymeric solutions turbulent flow, using two different constitutive equations to describe the effect of polymers on the flow. One of the used constitutive equations modeled the viscous anisotropic effects of elongated particles suspended in a Newtonian fluid. The other was an extension of the first equation, which also accounted for an elastic component (based on the Maxwell model). By the relative accuracy of the results (in comparison to their Laser Doppler velocimetry measurements) obtained using the two constitutive equations, the authors proposed that viscous anisotropic stresses play the key role in the mechanism of drag reduction.

Many recent DNS analyses of drag reducing polymer flows make use of the FENE-P (finitely extensible non-linear elastic with Peterlin approximation) constitutive equation, to evaluate an additional stress term in the momentum equation. The FENE-P model models the polymer elastic stress as a function of its elongation, based on a finitely extensible dumbbell description of the polymer (a finitely extensible spring with beads at the ends). Beads represent blocks of monomer that are small enough that their rotational motion is highly correlated. The springs account for the tendency of the polymer chain to assume configurations that leave the molecule in a ball (Figure

2.7). The spring should be viewed as a probabilistic (or entropic) spring that restores a stretched molecule into configurations that are more probable. Example treatments by that approach can be found in Dimitropoulos et al. [4], Sureshkumar et al. [12], Dimitropoulos et al. [25], who obtained successful results of flow parameters and turbulence characteristics.

Figure 2.7: FENE-P model: a spring with beads at the ends.

Sureshkumar et al. [12] also discuss some criteria for the onset of drag reduction based on a parametric analysis of their numerical results. Dimitropoulos et al. [26] analysed by this approach the energy budgets in polymer solution turbulent flows. Unique models for drag reduction in surfactant micellar solutions have also been proposed. This kind of additive can sometimes exhibit a behaviour different (as it was already said) from that with polymer additives, such as an increased drag reduction, above Virk's maximum asymptote.

More recently, Fichman and Hetsroni [27] discussed a preliminary possible electro-kinetic mechanism, exclusive for ionic surfactants micellar solutions. No complete explanation with comprehensive quantitative results is yet available for the phenomena of turbulent drag reduction by additives. The typical common features to be explained include lowered drag, unique velocity profiles, onset shear stress, and MDR asymptotic behaviour.

This information has provided additional insight into the mechanism(s) responsible for low/high drag reduction (less/greater than 30%) as well as the maximum drag reduction limit (Virk [8]).

Polymer orientation in most dumbbell models is described by a conformation tensor (Vaithianathan et al. [28]):

$$C_{ij} \equiv \frac{\langle r_i r_j \rangle}{\frac{1}{3}\langle r^2 \rangle_{eq}} \tag{2.1}$$

where r_i is the instantaneous orientation of a polymer dumbbell, r^2_{eq} is the square of the equilibrium separation distance, and the angle brackets imply an ensemble average over the configuration space of the dumbbell.

2.2.1 Instabilities

C_{ij} is symmetric and positive definite (SPD). Early attempts at numerical simulation of viscoelastic turbulence were plagued by Hadamard instabilities that resulted from the numerical loss of the SPD property (Dupret and Marchal [29]).

Sureshkumar and Beris [30] overcame these instabilities by introducing a stress diffusion term into the equation for the conformation tensor. Vaithianathan and Collins [31] exploited the SPD property of C_{ij} to derive independent equations for the eigenvectors and eigenvalues of the conformation tensor. Positive definiteness in this formulation implies the eigenvalues of C_{ij} should remain greater than zero. Finite extensibility of the polymer implies:

$$\lambda_1 + \lambda_2 + \lambda_3 \leq L^2 \tag{2.2}$$

where λ_i are the eigenvalues of C_{ij} and L is the maximum polymer extension (Beris and Edwards [32]). Whereas the implicit formulation of Vaithianathan and Collins [31] guarantees equation (2.2) is satisfied, the compact finite-difference method (Lele [33]) they used did not guarantee the eigenvalues remain positive. Instead, realizability was enforced by setting the negative eigenvalues to zero before constructing the conformation tensor, ensuring numerical stability. However, the uncontrolled, spatially distributed adjustments of the eigenvalues destroyed overall conservation of the conformation tensor, and spatial averages of the conformation tensor contained spurious contributions from the convective term. Thus the decomposition applied in Vaithianathan and Collins [31] guaranteed stability (by providing easy access to the eigenvalues), but did not guarantee conservation.

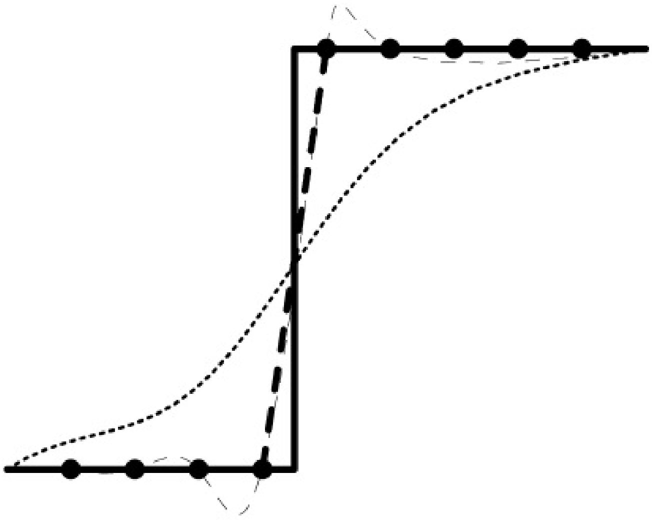

Figure 2.8: One-dimensional schematic of a shock (thick, solid line). Black dots represent the grid points. Thick dashed line is an ideal representation of the shock on the grid. A spectral representation, without an artificial stress diffusivity, would look like the thin dashed line, with overshoots and undershoots (Gibbs phenomenon). The dotted line indicates the effect of adding the stress diffusivity to the spectral representation. From Vaithianathan et al. [28].

The issue is reminiscent of early numerical approaches to compressible flows, which often suffered from loss of conservation (Laney [34]). The problem can be traced in part to the hyperbolic nature of the equation for C_{ij} in the Oldroyd-B, FENE-P and Giesekus models, which admits shocks (discontinuities) in the polymer stress tensor (El-Kareh and Gary Leal [35]). Discontinuities in the polymer stress cannot be fully resolved by a grid, and so the main responsibility of the numerical scheme is to correctly predict the jump magnitude. Jumps in the conformation tensor should satisfy the overall conservation balance to guarantee correct elastic wave propagation.

Consider, for example, the schematic shown in Figure 2.8. The solid line indicates a jump in the polymer stress tensor across a discontinuity. The other curves illustrate the equivalent numerical representation based on a finite-difference and spectral scheme. The Gibbs phenomenon observed in the spectral representation can be attenuated by introducing an artificial diffusivity. However, artificial diffusion can also reduce the magnitude of the jump. There are more sophisticated approaches to filtering the spectral modes so as to (just) eliminate the ringing, but they are still at a relatively early stage of development (Gottlieb and Hesthaven [36]). In contrast, specific finite-difference schemes have been designed to maintain the magnitude of the jump and avoid excessive spreading of the discontinuity.

Early hyperbolic solvers were first-order in space, robust and reliable, yet often-times overly dissipative (Laney [34]). More recent approaches have overcome these shortcomings while still preserving the simplicity of implementation and robustness (Van Leer [37], Nessyahu and Tadmor [38]). The approach taken in Vaithianathan et al. [28] is based on the method of Kurganov and Tadmor [39] (hereafter referred to as KT). Their unique second-order scheme guarantees that a positive scalar will remain so at all points. In that study, the authors have generalized the KT scheme to guarantee that a SPD tensor remains SPD. Spatial derivatives of the tensor are again second-order accurate. Furthermore, the method dissipates less elastic energy than methods based on artificial diffusion, resulting in stronger polymer-flow interactions.

2.2.2 Flow characteristics

In the wall-bounded turbulent flows, the inhomogeneous nature makes it difficult to analyse the interaction between turbulence and polymer micro-structures, due to the multitude of competing effects. In contrast, by removing the inhomogeneity emerging from the wall, such as for homogeneous isotropic turbulence (HIT) or bulk turbulence, it is easier to isolate and study the interactions between turbulence and polymer micro-structures. Therefore, studies of this kind of turbulence with drag-reducing additives have fundamental importance towards understanding the physics of additives-turbulence interactions. So far, several studies have been carried out based on HIT or bulk turbulence in dilute polymer or surfactant solution through experimental, theoretical and numerical methods and a preliminary understanding of the flow characteristics has been obtained.

To remove the inhomogeneity generated by the wall, the experiments were carried out on grid-generated turbulence or bulk turbulence in drag-reducing fluids. It was found that in grid-generated turbulence in dilute polymer solution, there is a significant alteration of turbulent kinetic energy distribution among scales (Fabula [40], McComb et al. [41]) and energy budget (Friehe and Schwarz [42]) compared with pure water flow and the overall turbulent intensity and pressure drop decrease (Friehe and Schwarz [42]). With the presence of polymers, the flow gives rise to a smaller dissipation rate than that expected for a corresponding Newtonian fluid flow (van Doorn et al. [43]). Besides, by flow visualization a suppression of small-scale structures was also obtained which is attributed to an elastic absorption of energy on those scales, and finally results in a truncation of energy cascade (van Doorn et al. [43], Barnard and Sellin [44]).

The above experimental studies of grid turbulence in a dilute polymer solution suggested that DR also exists even in situations where the wall plays no apparent role. A significant decrease in the Lagrangian acceleration variance and a modification of the Eulerian structure function in a dilute polymer solution also indicated the suppression of viscous dissipation and modification of the turbulent energy cascade (Crawford et al. [45], Ouellette et al. [46]).

Based on the experimental results of grid turbulence in a drag-reducing polymer solution, Tabor and De Gennes [47], De Gennes [48] proposed an elastic theory for DR and provided an alternative explanation for the drag-reducing effect in HIT based on the idea that polymers in turbulent flow exhibit elastic properties even at very low concentrations. They argued that the viscous effects which play a crucial role in Lumley's theory (Lumley [49]) are not at all relevant to the phenomenon of DR. In the theory, two scales are defined for a dilute polymer solution in HIT:

1. the trapping length, indicating the scale of the turbulence at which stretching of polymers begins; it is independent of polymer concentration, but dependent on both the relaxation time of polymers and turbulent kinetic dissipation rate,

2. the scale at which the polymer elastic energy is comparable to the turbulent kinetic energy of that scale. They concluded that polymers truncate the classical cascade when the scale becomes larger than the usual Kolmogorov scale.

3

Governing equations

Contents

In order to study the additives-turbulence interaction by DNS, an additional polymer stress term to the Navier-Stokes equation should be included. There are two major difficulties in the DNS of polymer solution flow:

1. how to model polymers accurately and efficiently
2. how to simulate the equation without incurring numerical instabilities

There is then a clear need to develop a turbulence closure for truly viscoelastic rheological constitutive equations that are able to model correctly the rheology of dilute and semi-dilute polymer solutions, such as the differential viscoelastic equations of Maxwell type like the Oldroyd-B, Giesekus or the FENE-P model (Dimitropoulos et al. [4], Sureshkumar and Beris [30], De Angelis et al. [50]). Among these models, FENE-P is the most widely used due to its relatively accurate representation of polymers dynamics, minimal computational complexity and its ability to show the drag-reducing behaviour of dilute polymer solution in wall-bounded flows analogous to the experimental results (Sureshkumar et al. [12], De Angelis et al. [50]). Therefore, FENE-P is also adopted in this thesis.

Due to the hyperbolic nature of constitutive models it is easy to generate Hadamard instabilities and cause divergence in numerical simulations (Dupret and Marchal [29]). Most studies have solved this problem based on adding an artificial diffusion term (Sureshkumar and Beris [30]), continuous decomposition (Vaithianathan and Collins [31]) or Cholesky decomposition (Vaithianathan and Collins [31]) and a high-order discrete scheme for conformation equations such as the MINMOD scheme (Yu and Kawaguchi [51]).

Vaithianathan et al. [28] discussed the remaining questions of the above methods and proposed the Kurganov-Tadmor (KT) scheme to solve the Hadamard instabilities. The scheme is second-order accurate in space everywhere except for the grid points losing symmetric positive definite (SPD) property. Where it occurs the scheme automatically becomes first-order accurate for these points to maintain the SPD property. To guarantee the SPD property of the conformation tensor at all times and all points, the KT scheme was used in the numerical simulations here presented (explained in detail in the next chapter).

3.1 Velocity field

The fluid is assumed to be an incompressible continuum, and so it satisfies a generalized form of the Navier-Stokes equations (continuity and momentum equations respectively):

$$\frac{\partial u_i}{\partial x_i} = 0, \tag{3.1}$$

$$\frac{\partial u_i}{\partial t} + u_j \frac{\partial u_i}{\partial x_j} = -\frac{1}{\rho}\frac{\partial p}{\partial x_i} + \frac{1}{\rho}\frac{\partial T_{ij}}{\partial x_j} \tag{3.2}$$

where u_i is i component of the velocity vector, ρ is the fluid density, p is the local pressure, T_{ij} is the combination of the viscous and polymer stresses.

The stress tensor can be written as a linear sum of contributions from the Newtonian solvent (superscript s) and the polymer (superscript p) as follows:

$$T_{ij} \equiv T_{ij}^{[s]} + T_{ij}^{[p]}, \tag{3.3}$$

where $T_{ij}^{[s]}$ is the Newtonian stress from the solvent defined as:

$$T_{ij}^{[s]} = 2\mu^{[0]}\beta S_{ij}, \tag{3.4}$$

being $\mu^{[s]}$ the dynamic viscosity of the solvent, and,

$$\beta \equiv \frac{\mu^{[s]}}{\mu^{[0]}}, \tag{3.5}$$

$$S_{ij} \equiv \frac{1}{2}\left(\frac{\partial u_i}{\partial x_j} + \frac{\partial u_j}{\partial x_i}\right) \tag{3.6}$$

in which, the superscript 0 means solvent plus polymer.

In equation (3.4) β is the ratio of the solvent viscosity to the solution viscosity at zero shear, S_{ij} is the rate of strain tensor and $T_{ij}^{[p]}$ the polymer stress which is defined as follows:

$$T_{ij}^{[p]} = \frac{\mu^{[p]}}{\tau_p}(f(r)C_{ij} - \delta_{ij}), \tag{3.7}$$

being the meanings of C_{ij}, r and $f(r)$ explained in detail in the following sub-section.

3.2 Constitutive model for the polymer

Although the capability to numerically simulate flow of viscoelastic fluids is relatively new (Sureshkumar et al. [12], Den Toonder et al. [24]), the technique has since been widely applied (e.g., Dimitropoulos et al. [4], Min et al. [13], De Angelis et al. [52], Dubief et al. [53], Ptasinski et al. [54], Sibilla and Baron [55]). For the most part, numerical simulations use constitutive equations derived from modelling the polymer molecule as two beads connected by an elastic spring i.e. a single dumbbell (Beris and Edwards [32], Bird et al. [56]).

The polymer dynamics are then entirely described by the evolution of the end-to-end vector connecting the two beads, represented as the phase-averaged configuration tensor defined in equation (2.1), where the r's are the components of the end-to-end vector (Figure 3.1). In a flow field, the evolution of C_{ij} is governed by the stretching and restoring forces acting on the dumbbell. The restoring force is identically the polymer stress tensor, so evaluation of the configuration tensor provides a direct measure of the modelled polymer stress tensor.

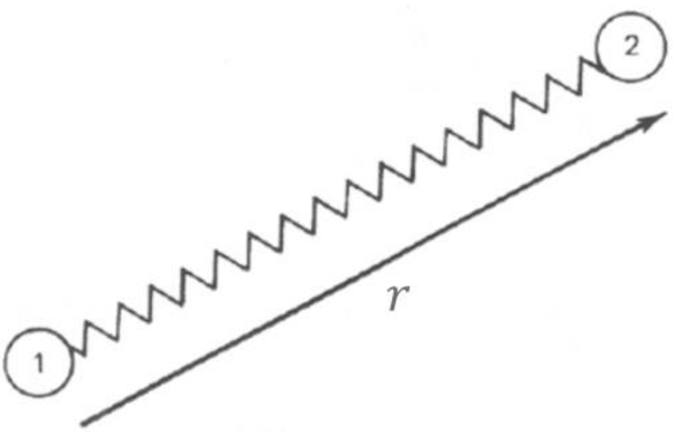

Figure 3.1: Elastic dumbbell with configuration given by vector **r**. From Resende [57].

The polymer model most often implemented for the study of DR is the FENE-P model (Bird et al. [56]). Although there are competing models (e.g., FENE, Oldroyd-B, Giesekus), the FENE-P model is preferred because it accounts for the finite extensibility of the molecule and uses a simple second-order closure model in the equation for the polymer stress tensor. The former characteristic, aside from being physically consistent with real polymers, reduces numerical instabilities, whereas the latter reduces computational costs.

Although the single dumbbell FENE-P model can capture the basic rheological properties of a polymer solution in many types of flows, there are clear circumstances in which the model does not capture the correct physics (Somasi et al. [58], Van Heel et al. [59], Vincenzi et al. [60], Wedgewood et al. [61], Zhou and Akhavan [62]).

The limitations of the model are primarily a consequence of the closure approximation (higher-order moments are not accounted for) and the fact that a polymer molecule consisting of typically $N \approx 10^5$ monomers has been reduced to a single dumbbell. In addition, the model does not incorporate polymer-polymer interactions, important even for dilute polymer solutions in which polymers have been found to organize into supermolecular structures (Kalashnikov [63]).

However, the FENE-P model has a number of features that make it suitable for describing a dilute solution of polymer molecules. In particular, finite extensibility makes the viscometric response of the polymer more agreeable with experimental observations (Azaiez and Homsy [64]).

In the FENE-P model, the polymer stress is defined as:

$$T_{ij}^{[p]} = \mu^{[0]}(1-\beta)\frac{f(r)C_{ij}-\delta_{ij}}{\tau_p} \tag{3.8}$$

where C_{ij} is the conformation tensor, δ_{ij} is the Kronecker delta, and τ_p is the Zimm relaxation time of the polymer.

The function $f(r)$ is the so-called Peterlin function defined as:

$$f(r) = \frac{L^2 - 3}{L^2 - r^2} \tag{3.9}$$

where L is the maximum extension of the polymer and $r^2 \equiv C_{kk}$ is the square of the mean separation between the beads. This function gives rise to a non-linear spring force that diverges as $r \to L$, ensuring the spring cannot extend beyond L.

Using the FENE-P model, the numerical simulation involves solving the continuity equation (3.1), the equation for the conservation of momentum (3.2) and the equation for the evolution of the conformation tensor given by:

$$\frac{\partial C_{ij}}{\partial t} + u_k \frac{\partial C_{ij}}{\partial x_k} = C_{jk} \frac{\partial u_i}{\partial x_k} + C_{ik} \frac{\partial u_j}{\partial x_k} - \frac{f(r) C_{ij} - \delta_{ij}}{\tau_p} \tag{3.10}$$

3.3 Properties of the conformation tensor

The effects of polymer stretch on the flow can be formally interpreted as an elastic effect or a viscous effect. In the framework of the FENE-P model (or similar polymer model), the elastic energy stored by a stretched polymer is proportional to the trace of the conformation tensor, $C_{kk} = C_{xx} + C_{yy} + C_{zz}$ (Min et al. [13]). If the problem is approached from the perspective of the elastic theory of DR, the transport equation for the elastic energy can be studied to understand the energy transfer between the polymers and the flow (Min et al. [13, 65]). Alternatively, and within the framework of the FENE-P model, Benzi et al. [21] approached the problem from the perspective of the viscous theory and found that an important component of the conformation tensor is C_{yy}, which appears in the momentum and kinetic energy equations as an effective viscosity.

The conformation tensor, **C**, is a measure of the second-order moment of the end-to-end distance vector of the polymer dumbbell. It can be written as in equation (2.1), where the vector **r** is the separation vector between the two beads of the dumbbell. From the definition, it follows that the conformation tensor is a symmetric positive definite (SPD) matrix. Hulsen [66] proved that during exact time evolution the conformation tensor must remain positive definite if it were initially. However, cumulative numerical errors that arise from virtually all initial value problem algorithms can give rise to negative eigenvalues. The presence of negative eigenvalues causes the unbounded growth of Hadamard instabilities that quickly overwhelm the calculation (Sureshkumar and Beris [30]).

Another important property of the conformation tensor is that the trace, which represents the square of the separation distance, must always be less than the square of the maximum extension, i.e. $r^2 \leq L^2$. The model guarantees this property through the force term, which diverges in strength as this limit is approached. Hence for flows of arbitrary strength, the restoring force is always sufficient to maintain this constraint. However, numerical errors in the evaluation of $Tr(\mathbf{C})$ can lead to violations of this constraint. Extension past L^2 causes the force to change sign, resulting in the rapid divergence of the calculation.

4

Numerical methods and coding

Contents

This chapter describes in depth the numerical simulation code used in all the simulations to be reported within this dissertation.

As it was already mentioned in the previous chapter (Chapter 3: ”Governing equations”), when solving numerically flows with polymer additives, two issues must be weighted: accuracy and time spent. Here, accuracy means not only modelling accurately the polymer but also avoiding numerical instabilities. Choosing how to model the polymer inside the flow was a matter of scientific work during the past 15 years. Among several models developed up to now, FENE-P is the one that has the best trade-off between accuracy and computational complexity.

After choosing the most appropriate model to represent polymer dynamics in a very efficient way (good ratio between time spent and accuracy), it is necessary to have a look into the numerical methods that are known to be good for each term of the Navier-Stokes Momentum and Constitutive Conformation tensor transport equations. This is done with detail in this chapter.

The numerical work here presented did not start from scratch, it started from two previous versions already tested and showing accurate results. Both versions were for DNS of newtonian fluids, one two-dimensional and the other three-dimensional. Both versions had the same numerical schemes for time and spatial discretization and they were kept constant through all the implementation process.

In the Navier-Stokes Momentum equation, a pseudo-spectral method is used for spatial discretization and fully explicit third order Runge-Kutta is used for temporal advancement. In the equation for the Conformation tensor transport, added due to presence of polymer, one term (the convective term) is discretized according to the so-called KT scheme whereas the rest of the terms are discretized using finite differences. The reason why this is done is explained in this chapter. The method used for temporal advancement was also the explicit third order Runge-Kutta method.

4.1 Spatial discretization schemes

Before going into the details of the numerical schemes and algorithms used in the numerical simulation code, it is important to take note of the computational domain, which is shown in the figure below.

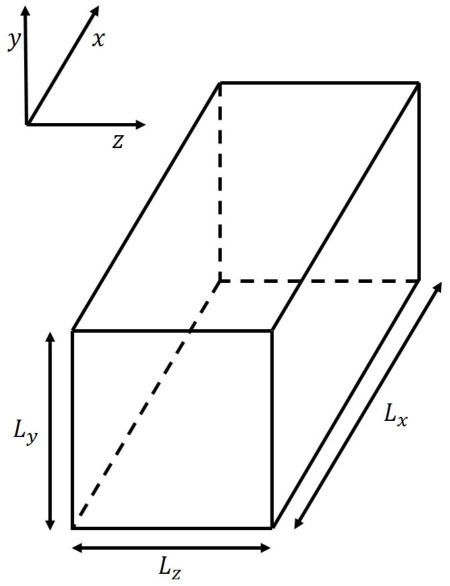

Figure 4.1: View of the computational box with reference frame and notation. For homogeneous isotropic turbulence, $L_x = L_y = L_z = 2\pi$. From da Silva [67].

To sum up, the equations to be solved are the following:

$$\underbrace{\frac{\partial u_i}{\partial x_i}}_{I} = 0, \tag{4.1}$$

$$\frac{\partial u_i}{\partial t} + u_j \frac{\partial u_i}{\partial x_j} = -\frac{1}{\rho}\frac{\partial p}{\partial x_i} + \frac{1}{\rho}\frac{\partial T_{ij}}{\partial x_j} \tag{4.2}$$

$$\underbrace{\frac{\partial C_{ij}}{\partial t}}_{VII} + \underbrace{u_k \frac{\partial C_{ij}}{\partial x_k}}_{VIII} = \underbrace{C_{jk}\frac{\partial u_i}{\partial x_k}}_{IX} + \underbrace{C_{ik}\frac{\partial u_j}{\partial x_k}}_{X} - \underbrace{\frac{f(r)C_{ij} - \delta_{ij}}{\tau_p}}_{XI} \tag{4.3}$$

Equation (4.2) can also be written in a more detailed way:

$$\underbrace{\frac{\partial u_i}{\partial t}}_{II} + \underbrace{u_j \frac{\partial u_i}{\partial x_j}}_{III} = \underbrace{-\frac{1}{\rho}\frac{\partial p}{\partial x_i}}_{IV} + \underbrace{\nu^{[s]}\frac{\partial}{\partial x_j}\left(\frac{\partial u_i}{\partial x_j} + \frac{\partial u_j}{\partial x_i}\right)}_{V} + \underbrace{\frac{\nu^{[p]}}{\tau_p}\frac{\partial}{\partial x_j}\left(f(r)C_{ij} - \delta_{ij}\right)}_{VI} \tag{4.4}$$

Following the notation written in the equations (4.1), (4.3) and (4.4), terms I to VI are solved with the pseudo-spectral method, term $VIII$ is solved using the KT method while terms VII, IX and X are solved with central finite differences. Term XI is referred in the sub-section ”Conformation-velocity coupling”.

4.1.1 Pseudo-spectral method

Pseudo-spectral methods appeared in 1970 and are a class of numerical methods used in applied mathematics and scientific computing for the solution of partial differential equations (PDEs), such as the direct simulation of a particle with an arbitrary wavefunction interacting with an arbitrary potential. They are used extensively in computational fluid dynamics - such as turbulence modelling and weather predictions - non-linear waves, seismic modelling and other areas.

They are related to spectral methods and the 'pseudo-spectral' in the method refers to the spatial part of a PDE.

Spectral solutions to time-dependent PDEs are formulated in the frequency-wavenumber domain and solutions are obtained in terms of spectra.

In the pseudo-spectral approach, the PDEs are solved pointwise in physical space. However, the space derivatives are calculated using orthogonal functions (e.g. Fourier Integrals, Chebyshev polynomials). They are either evaluated using matrix-matrix multiplications, fast Fourier transform (FFT), or convolutions.

There are two important aspects that have to be respected in order to fulfil the requirements of the method. These requirements are:

- functions must be periodic: periodic box of length 2π and periodic boundary conditions
- it is necessary to take aliasing errors into account: in this thesis, the rule applied is the $2/3$ rule

Important points that make this method different form the others are:

- high accuracy
- periodic boundary conditions
- expensive method
- storage is reduced to half due to the Hermitian property which states, for f real, that $\hat{f}_{-k} = \hat{f}_k^*$

4.1.1.A Math behind

Given a certain function $u(x)$ in the physical space, to have the same function in the Fourier (also called spectral) space $\hat{u}(k)$[1], it must be applied the direct Fourier transform (denoted hereafter by $\mathcal{F}$):

$$\hat{u}(k) = \mathcal{F}\left\{u(x)\right\} = \frac{1}{2\pi}\int_{-\infty}^{+\infty} u(x) \cdot e^{-\mathrm{i}kx} \cdot dx \tag{4.5}$$

In which, k is the wave number and it is computed as follows, being λ_w the wavelength (Figure 4.2):

$$k = \frac{2\pi}{\lambda_w} \tag{4.6}$$

---

[1] A function in the spectral space is identified with $\hat{\ }$.

The reverse is done with the inverse Fourier transform ($\mathcal{F}^{-1}$):

$$u(x) = \mathcal{F}^{-1}\left\{u(k)\right\} = \int_{-\infty}^{+\infty} \hat{u}(k) \cdot e^{\mathrm{i}kx} \cdot dk \tag{4.7}$$

So far, it is already known that in the physical space one works with the position (as independent variable) and in the spectral space with the wave number. It is also known that there are two operations that transport the function between spaces. This information is systematized in Figure 4.2.

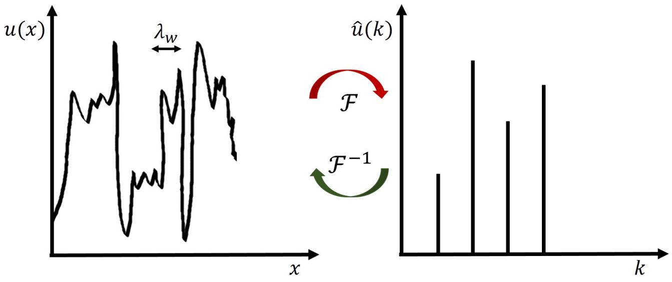

Figure 4.2: Function transport between spaces, physical and Fourier. Representation of the wavelength in the physical space.

One of the main advantages of this method, as it was already mentioned, is the simplicity of most of the terms whenever they are in the spectral space, even if they are complex in the physical space. Below, this characteristic is illustrated for a derivative computation:

$$\frac{du(x)}{dx} = \frac{d}{dx}\int_{-\infty}^{+\infty} \hat{u}(k) \cdot e^{\mathrm{i}kx} \cdot dk = \int_{-\infty}^{+\infty} \frac{d}{dx}\left[\hat{u}(k) \cdot e^{\mathrm{i}kx}\right] \cdot dk = \int_{-\infty}^{\infty} \mathrm{i}k\hat{u}(k) \cdot e^{\mathrm{i}kx} \cdot dk \tag{4.8}$$

Hence,

$$\mathcal{F}\left\{\frac{du}{dx}\right\} = \mathrm{i}k\hat{u}(k) \tag{4.9}$$

The most important math operations are summarized in Table 4.1 for both physical and spectral spaces.

Table 4.1: Fourier transform most important mathematical properties.

Physical space	Spectral space	Description
$af + bg$	$a\hat{f}(\mathbf{k},t) + b\hat{g}(\mathbf{k},t)$	
$\frac{\partial f}{\partial x_i}$	$\mathrm{i}k_i\hat{f}(\mathbf{k},t)$	
$\nabla^2 f$	$-k^2\hat{f}(\mathbf{k},t)$	
$\frac{\partial u_i}{\partial x_i}$	$\mathrm{i}k_i\hat{u}_i(\mathbf{k},t)$	
$\nabla \times \mathbf{u}$	$\mathrm{i}\mathbf{k} \times \hat{\mathbf{u}}(\mathbf{k},t)$	
$f(\mathbf{x},t) \times g(\mathbf{x},t)$	$\left[\hat{f} \star \hat{g}\right](\mathbf{k},t)$	$\star$ convolution product

4.1.1.B Applied to the Navier-Stokes equations

The equations to be solved with the pseudo-spectral method are the Navier-Stokes continuity and momentum conservation equations:

$$\frac{\partial u_i}{\partial x_i} = 0 \tag{4.10}$$

$$\frac{\partial u_i}{\partial t} + \frac{\partial (u_i u_j)}{\partial x_j} = \nu^{[s]}\frac{\partial^2 u_i}{\partial^2 x_j} - \frac{1}{\rho}\frac{\partial p}{\partial x_i} + \frac{\nu^{[p]}}{\tau_p}\frac{\partial}{\partial x_j}\left(f(r)C_{ij} - \delta_{ij}\right) \tag{4.11}$$

It is easy to see, according to what was seen in the previous sub-section, that:

$$\mathcal{F}\left\{\frac{\partial u_i}{\partial x_i}\right\} = \mathrm{i}k_i\hat{u}_i \tag{4.12}$$

Hence, the continuity equation in the spectral space is written as follows:

$$k_i\hat{u}_i = 0 \tag{4.13}$$

For the Navier-Stokes Momentum equation (4.11), the terms in the spectral space are the following:

$$\mathcal{F}\left\{\frac{\partial u_i}{\partial t}\right\} = \frac{d\hat{u}_i}{dt} \tag{4.14}$$

$$\mathcal{F}\left\{\nu^{[s]}\frac{\partial^2 u_i}{\partial^2 x_j}\right\} = -\nu^{[s]}k^2\hat{u}_i \tag{4.15}$$

$$\mathcal{F}\left\{-\frac{1}{\rho}\frac{\partial p}{\partial x_i}\right\} = -\frac{1}{\rho}\mathrm{i}k_i\hat{p} \tag{4.16}$$

$$\mathcal{F}\left\{\frac{\partial}{\partial x_j}\left(u_i u_j - \frac{\nu^{[p]}\left(f(r)C_{ij}-\delta_{ij}\right)}{\tau_p}\right)\right\} = \hat{G}_i \tag{4.17}$$

Rewriting the Navier-Stokes Momentum equation, now in the Fourier space, one has:

$$\frac{d\hat{u}_i}{dt} + \nu^{[s]}k^2\hat{u}_i = -\frac{1}{\rho}\mathrm{i}k_i\hat{p} - \hat{G}_i \tag{4.18}$$

If one multiplies the equation above by ik_i, which is the same as saying to apply the divergence in the physical space, one gets:

$$k^2\frac{1}{\rho}\hat{p} = \mathrm{i}k_i\hat{G}_i \tag{4.19}$$

From the equation (4.19) the pressure can be obtained:

$$\hat{p} = \rho\frac{\mathrm{i}k_j\hat{G}_j}{k^2} \tag{4.20}$$

Thus, the final expression for the Navier-Stokes Momentum equation in the spectral space is:

$$\frac{d\hat{u}_j}{dt} + \nu^{[s]}k^2\hat{u}_j = -\left(\delta_{jk} - \frac{k_j k_k}{k^2}\right)\hat{G}_k \tag{4.21}$$

It is important to notice that there is no pressure term in the equation above, or to be more precise although the pressure term is represented in equation (4.21), the pressure itself is not being computed directly.

4.1.2 Kurganov Tadmor (KT) method

In this section, it is presented a new central difference scheme for updating the conformation tensor **C**, based on the KT algorithm. The method is second-order accurate in space (arbitrary order in time) everywhere except where it leads to a loss of the SPD property. Where that occurs, the method automatically reverts to first-order for that grid point, ensuring the SPD property is maintained. This scheme is used for the discretization of the convective term, term $VIII$, of equation (4.3):

$$\mathbf{u}\cdot\nabla\mathbf{C} = \frac{\mathbf{H}^x_{i+1/2,j,k} - \mathbf{H}^x_{i-1/2,j,k}}{\Delta x} + \frac{\mathbf{H}^y_{i,j+1/2,k} - \mathbf{H}^y_{i,j-1/2,k}}{\Delta y} + \frac{\mathbf{H}^z_{i,j,k+1/2} - \mathbf{H}^z_{i,j,k-1/2}}{\Delta z} \tag{4.22}$$

where the convective flux **H** in each direction is given by:

$$\mathbf{H}^x_{i+1/2,j,k} = \frac{1}{2}u_{i+1/2,j,k}(\mathbf{C}^+_{i+1/2,j,k} + \mathbf{C}^-_{i+1/2,j,k}) - \frac{1}{2}|u_{i+1/2,j,k}|(\mathbf{C}^+_{i+1/2,j,k} + \mathbf{C}^-_{i+1/2,j,k}) \tag{4.23}$$

$$\mathbf{H}^y_{i,j+1/2,k} = \frac{1}{2}v_{i,j+1/2,k}(\mathbf{C}^+_{i,j+1/2,k} + \mathbf{C}^-_{i,j+1/2,k}) - \frac{1}{2}|v_{i,j+1/2,k}|(\mathbf{C}^+_{i,j+1/2,k} + \mathbf{C}^-_{i,j+1/2,k}) \tag{4.24}$$

$$\mathbf{H}^z_{i,j,k+1/2} = \frac{1}{2}w_{i,j,k+1/2}(\mathbf{C}^+_{i,j,k+1/2} + \mathbf{C}^-_{i,j,k+1/2}) - \frac{1}{2}|w_{i,j,k+1/2}|(\mathbf{C}^+_{i,j,k+1/2} + \mathbf{C}^-_{i,j,k+1/2}) \tag{4.25}$$

The superscripts '$+$' and '$-$' on the right-hand side in equations (4.23), (4.24) and (4.25) designate values of the conformation tensor at the interface obtained in the limit approaching the point of interest from the right ($+$) or left ($-$) side. The conformation tensor **C** at the interface is constructed from the following second-order, piecewise, linear approximations:

$$\mathbf{C}^{\pm}_{i+1/2,j,k} = \mathbf{C}_{i+1/2\pm1/2,j,k} \mp \left(\frac{\Delta x}{2}\right)\left(\frac{\partial \mathbf{C}}{\partial x}\right)_{i+1/2\pm1/2,j,k} \tag{4.26}$$

$$\mathbf{C}^{\pm}_{i,j+1/2,k} = \mathbf{C}_{i,j+1/2\pm1/2,k} \mp \left(\frac{\Delta y}{2}\right)\left(\frac{\partial \mathbf{C}}{\partial y}\right)_{i,j+1/2\pm1/2,k} \tag{4.27}$$

$$\mathbf{C}^{\pm}_{i,j,k+1/2} = \mathbf{C}_{i,j,k+1/2\pm1/2} \mp \left(\frac{\Delta z}{2}\right)\left(\frac{\partial \mathbf{C}}{\partial z}\right)_{i,j,k+1/2\pm1/2} \tag{4.28}$$

The potential candidates for approximating the gradients are:

$$\left(\frac{\partial \mathbf{C}}{\partial x}\right)_{i,j,k} = \left\{\begin{array}{c} \frac{\mathbf{C}_{i+1,j,k}-\mathbf{C}_{i,j,k}}{\Delta x} \\ \frac{\mathbf{C}_{i,j,k}-\mathbf{C}_{i-1,j,k}}{\Delta x} \\ \frac{\mathbf{C}_{i+1,j,k}-\mathbf{C}_{i-1,j,k}}{2\Delta x} \end{array}\right\} \tag{4.29}$$

It is selected a derivative approximation that can yield SPD results for $C^{+}_{i-1/2}$ and $C^{-}_{i+1/2}$. When two or more candidates satisfy the criterion, it is selected the one which maximizes the minimum eigenvalue for these two tensors. When none of them meet this criterion, the derivative is set to zero, reducing to first-order accurate.

The velocities needed to compute the convective flux **H** are given by the interpolation and filtering operations shown below:

$$u_{i\pm1/2,j,k} = \mathcal{F}^{-1}\left\{\hat{u}e^{\pm \mathrm{i}k_x\Delta x/2}\frac{sin(k_y\Delta y/2)}{k_y\Delta y/2}\frac{sin(k_z\Delta z/2)}{k_z\Delta z/2}\right\} \tag{4.30}$$

$$v_{i,j\pm1/2,k} = \mathcal{F}^{-1}\left\{\hat{v}e^{\pm \mathrm{i}k_y\Delta y/2}\frac{sin(k_z\Delta z/2)}{k_z\Delta z/2}\frac{sin(k_x\Delta x/2)}{k_x\Delta x/2}\right\} \tag{4.31}$$

$$w_{i,j,k\pm1/2} = \mathcal{F}^{-1}\left\{\hat{w}e^{\pm \mathrm{i}k_z\Delta z/2}\frac{sin(k_x\Delta x/2)}{k_x\Delta x/2}\frac{sin(k_y\Delta y/2)}{k_y\Delta y/2}\right\} \tag{4.32}$$

where k_x, k_y and k_z are the wave numbers in the respective directions.

4.1.3 Finite difference method

The code is developed for use with a finite difference approach in which the differential equations are approximated at each point, unlike finite volume methods where differential equations are averaged around a small control volume surrounding each point.

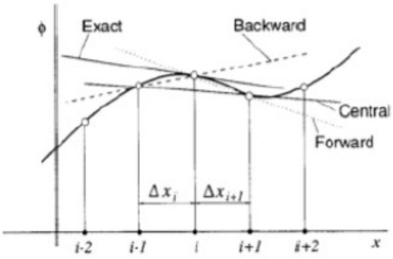

Figure 4.3: Graphical view of how finite difference method works for the first derivative, in case of non-uniform mesh. From Ferziger and Perić [68].

From Figure 4.3, it is possible to identify three types of finite difference:

BACKWARD:

$$\left(\frac{\partial \phi}{\partial x}\right)_i \approx \frac{\phi_i - \phi_{i-1}}{\Delta x_i} \tag{4.33}$$

CENTRAL:

$$\left(\frac{\partial \phi}{\partial x}\right)_i \approx \frac{\phi_{i+1} - \phi_{i-1}}{\Delta x_i + \Delta x_{i+1}} \tag{4.34}$$

FORWARD:

$$\left(\frac{\partial \phi}{\partial x}\right)_i \approx \frac{\phi_{i+1} - \phi_i}{\Delta x_{i+1}} \tag{4.35}$$

In the numerical simulation code, only central finite differences are used once they are second order accurate while backward and forward finite differences are just first order accurate.

For a better understanding, it is done below the spatial discretization of the term IX with $k = 1$ meaning that the derivative is done in the x-direction. It is important to notice that, in the code, the mesh is uniform. For this example, let us consider a generic point P with coordinates (I, J, K):

$$\left(C_{j1}\frac{\partial u_i}{\partial x_1}\right)_P \approx C_{j1}\frac{(u_i)_{I,J,K+1} - (u_i)_{I,J,K-1}}{2\Delta x_1} \tag{4.36}$$

For the other terms, VII and X, the process is similar.

4.2 Temporal advancement scheme

This code uses a fully explicit temporal advancement scheme (third order Runge-Kutta) for the Navier-Stokes equations and for the Conformation tensor transport equation.

The equations to be solved can be written as follows:

$$\frac{\partial \mathbf{u}}{\partial t} = N(\mathbf{u}) + L^{[s]}(\mathbf{u}) + L^{[p]}(\mathbf{C}) \tag{4.37}$$

$$\nabla \cdot \mathbf{u} = 0, \tag{4.38}$$

in which, $N(\mathbf{u})$, $L^{[s]}(\mathbf{u})$ and $L^{[p]}(\mathbf{C})$ are the convective term (term III) and the pressure term (term IV), the viscous term due to the solvent (term V) and the viscous term due to the polymer (term VI), respectively,

$$N(\mathbf{u}) = \mathbf{u} \times \omega - \frac{1}{\rho}\nabla p \tag{4.39}$$

$$L^{[s]}(\mathbf{u}) = \nu^{[s]}\nabla^2\mathbf{u} \tag{4.40}$$

$$L^{[p]}(\mathbf{C}) = \nu^{[p]}\nabla \cdot \left(\frac{f(r)\mathbf{C} - \mathbf{I}}{\tau_p}\right) \tag{4.41}$$

A 3^{rd} order Runge-Kutta time stepping scheme computes each new velocity and conformation tensor at the new sub-step $\mathbf{u}^k \equiv \mathbf{u}^n$, $\mathbf{C}^k \equiv \mathbf{C}^n$ from the last two sub-steps $\mathbf{u}^{k-1}$, $\mathbf{C}^{k-1}$ and $\mathbf{u}^{k-2} \equiv \mathbf{u}^{n-1}$, $\mathbf{C}^{k-2} \equiv \mathbf{C}^{n-1}$. Hence, equation (4.37) can be rewritten:

$$\begin{aligned}\frac{\mathbf{u}^k - \mathbf{u}^{k-1}}{\Delta t} =& \alpha_k \left[N\left(\mathbf{u}^{k-1}\right) + L^{[s]}\left(\mathbf{u}^{k-1}\right) + L^{[p]}\left(\mathbf{C}^{k-1}\right)\right] + \\ & \beta_k \left[N\left(\mathbf{u}^{k-2}\right) + L^{[s]}\left(\mathbf{u}^{k-2}\right) + L^{[p]}\left(\mathbf{C}^{k-2}\right)\right],\end{aligned} \tag{4.42}$$

and the coefficients α_k and β_k are (Williamson [69]):

$$\begin{aligned} \alpha_1 &= \frac{8}{15} & \beta_1 &= 0 \\ \alpha_2 &= \frac{5}{12} & \beta_2 &= -\frac{17}{60} \\ \alpha_3 &= \frac{3}{4} & \beta_3 &= -\frac{5}{12} \end{aligned} \tag{4.43}$$

4.2.1 Conformation-velocity coupling

To know each new velocity at each new sub-step, it is necessary to know the conformation tensor at the previous sub-step(s).

Equation (4.3) can be written in the following form:

$$\frac{\partial \mathbf{C}}{\partial t} = N'(\mathbf{u}, \mathbf{C}) + M(\mathbf{u}, \mathbf{C}) + {L^{[p]}}'(\mathbf{C}), \tag{4.44}$$

where $N'(\mathbf{u}, \mathbf{C})$, $M(\mathbf{u}, \mathbf{C})$ and ${L^{[p]}}'(\mathbf{C})$ are, respectively, the convective (term $VIII$), the production (terms IX and X) and the force (term XI) terms:

$$N'(\mathbf{u}, \mathbf{C}) = -\mathbf{u} \cdot \nabla\mathbf{C} \tag{4.45}$$

$$M\left(\mathbf{u},\mathbf{C}\right) = \mathbf{C}\cdot\nabla\mathbf{u} + \nabla\mathbf{u}^T\cdot\mathbf{C} \tag{4.46}$$

$$L^{[p]'}\left(\mathbf{C}\right) = -\frac{f(r)\mathbf{C}-\mathbf{I}}{\tau_p} \tag{4.47}$$

The same process that was applied before to the Navier-Stokes Momentum equation in equation (4.42), is done here. Thus, the following is obtained:

$$\begin{aligned}\frac{\mathbf{C}^k-\mathbf{C}^{k-1}}{\Delta t} =&\alpha_k\left[N'\left(\mathbf{u}^{k-1},\mathbf{C}^{k-1}\right)+M\left(\mathbf{u}^{k-1},\mathbf{C}^{k-1}\right)+L^{[p]'}\left(\mathbf{C}^{k-1}\right)\right]+\\ &\beta_k\left[N'\left(\mathbf{u}^{k-2},\mathbf{C}^{k-2}\right)+M\left(\mathbf{u}^{k-2},\mathbf{C}^{k-2}\right)+L^{[p]'}\left(\mathbf{C}^{k-2}\right)\right],\end{aligned} \tag{4.48}$$

where α_k and β_k are the coefficients of (4.43).

It is important to notice that the Runge-Kutta step of equation (4.48) is not the same as that of the equation (4.42). In equation (4.48), $\mathbf{C}^{k-2}\equiv\mathbf{C}^{n-2}$ and $\mathbf{C}^k\equiv\mathbf{C}^{n-1}$, whereas in equation (4.42), $\mathbf{C}^{k-2}\equiv\mathbf{C}^{n-1}$.

5

Verification and code to code comparison

Contents

In order to have full confidence that the results generated by the two codes, where all the programming work within this thesis was done, extensive validation tests with results already known were performed.

Firstly, the polymer constitutive model was coded in the 2D numerical simulation code, where it was easier to implement and easier to check the validity of the results obtained.

Secondly, a Couette flow test was performed. Special conditions were created so that the numerical schemes used can deal with the flow. For instance, the initial velocity profile was changed and was frozen in time, which means that the velocity profile was kept constant during all the simulation. The verification of the 2D code is minutely presented in section ”2D code: Verification”.

Thirdly, the verified 2D numerical simulation code was used to build the 3D numerical simulation code. After that, pseudo 2D tests were performed i.e. the test that was carried out for the 2D code was also done in the 3D code but for two directions each time - that is why the tests are called pseudo 2D. The results were the same as for the 2D code and they are not shown in this document.

Finally, to guarantee full reliability of the 3D numerical simulation code, it was compared with the code used in Cai et al. [70]. DHIT DNS were performed and some quantities are analysed comparing to Cai's results. As some parameters of Cai's simulations are omitted in the article (Cai et al. [70]), only the trends are comparable and that is what is done in section ”3D code: Code to code comparison”.

5.1 2D code: Verification

As already mentioned, in order to verify the 2D code, a test with the Couette flow was performed. Since the code is pseudo-spectral the initial velocity profile must be periodic[1]. Also, this profile is frozen in time forcing the conformation tensor to match the analytical solution. Thus, the velocity profile - constant in time - is shown in Figure 5.1.

---

[1] It is important to notice that also the conformation tensor entries have to be periodic because, although the equation that describes the transport of the conformation tensor is not discretized with a pseudo-spectral method, there is a term in the Navier-Stokes Momentum equation where they are accounted for.

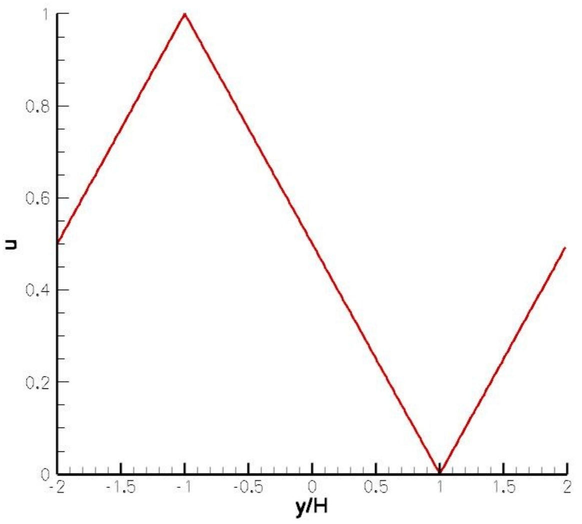

Figure 5.1: Velocity profile prescribed in the beginning and frozen during all the simulation. H is the unit of length used in the code.

The velocity profile was frozen during the simulation i.e. the update step that is done by the Runge-Kutta method was cancelled so that the numerical solution could converge to the analytical.

Table 5.1: Simulation parameters.

General properties			Polymer properties		
Reynolds number	Re	1000	Maximum molecular extensibility	L	100
Time-step (s)	Δt	0.1	Relaxation time (s)	τ_p	0.1
Box dimensions		$4H \times 4H$	Polymer concentration	β	0.9
Mesh		128×128			

The initial profile for the conformation was set to zero in each entry.

One could notice that the profile of Figure 5.1 is not the Couette profile, because of the numerical scheme. Hence, only in the range $-1 \leq y/H \leq +1$ the analytical and numerical solutions are comparable.

The analytical solution is derived with detail in this dissertation and is also documented in Pinho et al. [71] and in Mósca et al. [72].

The conformation tensor obeys an hyperbolic differential equation of the form:

$$f(C_{kk})C_{ij}+\tau_p\left(\frac{\partial C_{ij}}{\partial t}+u_k\frac{\partial C_{ij}}{\partial x_k}-C_{jk}\frac{\partial u_i}{\partial x_k}-C_{ik}\frac{\partial u_j}{\partial x_k}\right)=\delta_{ij} \tag{5.1}$$

At this point, it is important to notice that from equation (5.1) it comes out that $C_{ij}=C_{ji}$ in general, and not only for this particular case. Thus, there are only six independent components in the conformation tensor.

By continuity and because it is a two-dimensional flow, one has:

$$v=0,w=0 \tag{5.2}$$

Since the flow is steady, fully developed in the x direction and two-dimensional, it is easy to see that:

$$\frac{\partial}{\partial t}=0,\frac{\partial}{\partial x}=0,\frac{\partial}{\partial z}=0 \tag{5.3}$$

So far, equation (5.1) can be rewritten, for this particular flow, as follows:

$$f(C_{kk})C_{ij}-\tau_p\left(C_{jk}\frac{\partial u_i}{\partial x_k}+C_{ik}\frac{\partial u_j}{\partial x_k}\right)=\delta_{ij} \tag{5.4}$$

Writing down the equation above for each entry of the matrix **C**, one obtains:

For i=1, j=1:

$$f(C_{kk})C_{11}-2\tau_pC_{12}\frac{\partial U}{\partial y}=1 \tag{5.5}$$

For i=1, j=2:

$$f(C_{kk})C_{12}-\tau_pC_{22}\frac{\partial U}{\partial y}=0 \tag{5.6}$$

For i=1, j=3:

$$f(C_{kk})C_{13}-\tau_pC_{32}\frac{\partial U}{\partial y}=0 \tag{5.7}$$

For i=2, j=1:

$$f(C_{kk})C_{21}-\tau_pC_{22}\frac{\partial U}{\partial y}=0 \tag{5.8}$$

For i=2, j=2:

$$f(C_{kk})C_{22}=1 \tag{5.9}$$

For i=2, j=3:

$$f(C_{kk})C_{23}=0\Leftrightarrow C_{23}=0 \tag{5.10}$$

For i=3, j=1:

$$f(C_{kk})C_{31} - \tau_p C_{32}\frac{\partial U}{\partial y} = 0 \tag{5.11}$$

For i=3, j=2:

$$f(C_{kk})C_{32} = 0 \Leftrightarrow C_{32} = 0 \tag{5.12}$$

For i=3, j=3:

$$f(C_{kk})C_{33} = 1 \tag{5.13}$$

Taking into account that $C_{23} = C_{32} = 0$, from equations (5.7) and (5.11) one has $C_{13} = 0$ and $C_{31} = 0$, respectively. Rewriting equation (5.6) isolating C_{12}, one has:

$$C_{12} = \frac{\tau_p C_{22}\frac{\partial U}{\partial y}}{f(C_{kk})} \tag{5.14}$$

From equation (5.9), one gets:

$$\frac{L^2-3}{L^2-(C_{11}+C_{22}+C_{33})}C_{22} = 1 \Leftrightarrow L^2C_{22}-3C_{22} = L^2-C_{11}-C_{22}-C_{33} \Leftrightarrow C_{11} = C_{22}(1-L^2)+L^2 \tag{5.15}$$

Comparing equations (5.9) and (5.13) one sees that for this particular flow, $C_{22} = C_{33}$.

Also from equation (5.9) one sees that the Peterlin function $f(C_{kk})$ can be written as function only of C_{22}:

$$f(C_{kk}) = \frac{1}{C_{22}} \tag{5.16}$$

From equation (5.5), one obtains:

$$C_{12} = \frac{f(C_{kk})C_{11}-1}{2\tau_p\frac{\partial U}{\partial y}} \tag{5.17}$$

Substituting equation (5.17) in equation (5.6), one has:

$$f(C_{kk})\left(\frac{f(C_{kk})C_{11}-1}{2\tau_p\frac{\partial U}{\partial y}}\right) - \tau_p C_{22}\frac{\partial U}{\partial y} = 0 \tag{5.18}$$

Replacing $f(C_{kk})$ by $\frac{1}{C_{22}}$, in equation (5.18), one gets:

$$\frac{C_{11}}{C_{22}^2} - \frac{1}{C_{22}} = 2\tau_p^2 C_{22}\left(\frac{\partial U}{\partial y}\right)^2 \tag{5.19}$$

Substituting equation (5.17) in equation (5.6), one obtains a cubic polynomial in function of C_{22}:

$$C_{22}^3 + \frac{L^2}{2\tau_p^2\left(\frac{\partial U}{\partial y}\right)^2} C_{22} - \frac{L^2}{2\tau_p^2\left(\frac{\partial U}{\partial y}\right)^2} = 0 \tag{5.20}$$

The only real solution for this cubic equation is given by:

$$C_{22} = \left[\frac{L^2}{4\tau_p^2\left(\frac{\partial U}{\partial y}\right)^2} + \sqrt{\frac{L^4}{16\tau_p^4\left(\frac{\partial U}{\partial y}\right)^4} + \frac{L^6}{216\tau_p^6\left(\frac{\partial U}{\partial y}\right)^6}}\right]^{1/3} + \left[\frac{L^2}{4\tau_p^2\left(\frac{\partial U}{\partial y}\right)^2} - \sqrt{\frac{L^4}{16\tau_p^4\left(\frac{\partial U}{\partial y}\right)^4} + \frac{L^6}{216\tau_p^6\left(\frac{\partial U}{\partial y}\right)^6}}\right]^{1/3} \tag{5.21}$$

Thus, for the verification test, given the properties of Table 5.1, the analytical solution for **C** is the following:

$$\mathbf{C} \approx \begin{bmatrix} 1 & -0.0318 & 0 \\ -0.0318 & 1 & 0 \\ 0 & 0 & 1 \end{bmatrix} \tag{5.22}$$

In Figure 5.2, the analytical solution for each entry of **C** is presented.

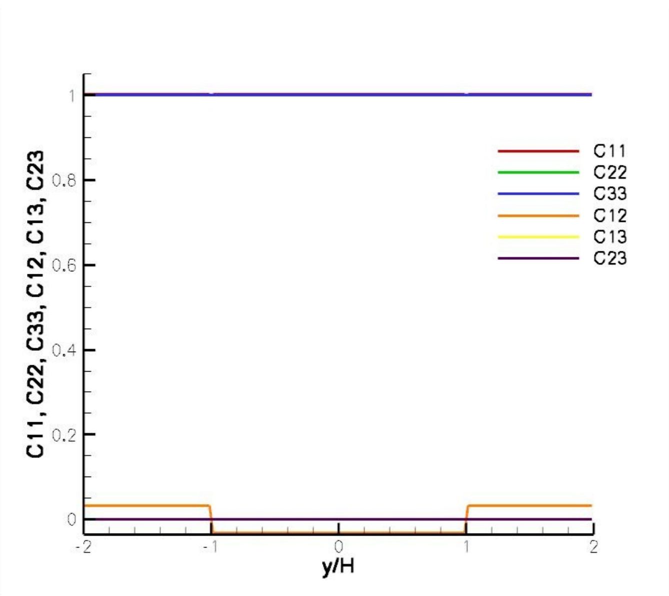

Figure 5.2: Analytical solution for the six independent components of the conformation tensor.

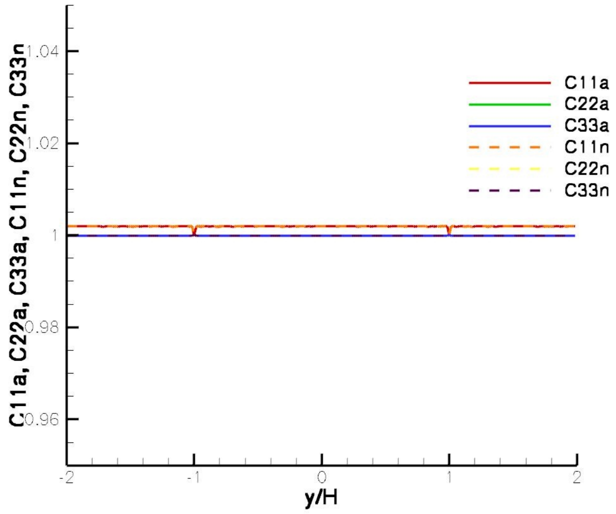

Figure 5.3: C_{ii} values for analytical (**a**) and numerical (**n**) solutions.

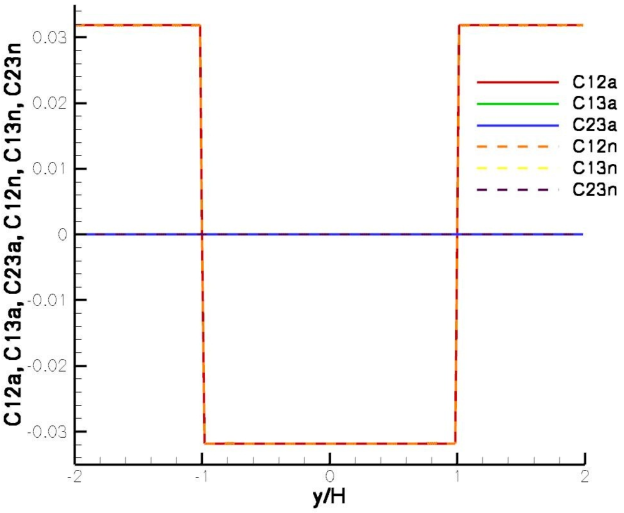

Figure 5.4: $C_{ij}, i \neq j$ values for analytical (**a**) and numerical (**n**) solutions.

In Figures 5.3 and 5.4, the diagonal components and the non-diagonal components, respectively, are computed analytical and numerically.

From Figures 5.3 and 5.4, it is possible to see that the dashed lines and the solid lines, i.e. the numerical and the analytical solutions, respectively, follow the same trend and the same values.

The 2D code is therefore verified!

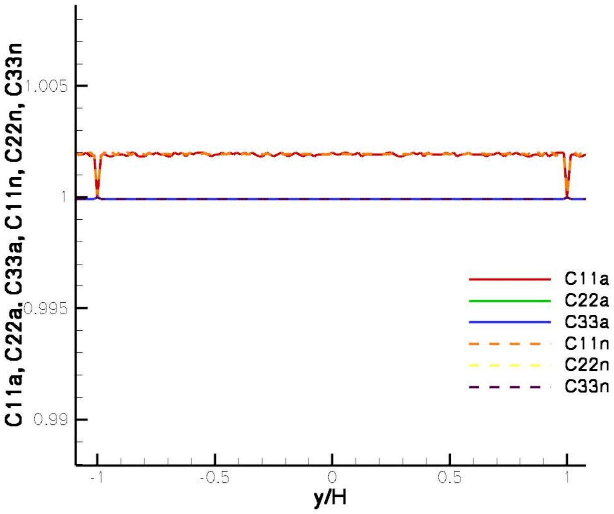

Figure 5.5: Detail of: C_{ii} values for analytical (**a**) and numerical (**n**) solutions.

Figure 5.5 shows well the precision of the numerical solution.

5.2 3D code: Code to code comparison

At this point, it is important to make a few remarks about homogeneous isotropic turbulence. A flow is said to be homogeneous and isotropic when:

- there are no spatial gradients in any averaged quantity
- there is no mean flow

In spite of being possible to create conditions to have an homogeneous isotropic flow experimentally, it is important to keep in mind that homogeneous isotropic turbulence is an idealized flow. The challenge is then to understand what aspects of these theories apply to natural flows and what are pathological.

More recently, with the development of numerical simulation many researchers have carried out DNS for forced HIT (FHIT) and decaying HIT (DHIT) to study the additives-turbulence interaction and physical mechanism of drag reduction (DR).

In FHIT with the presence of polymers, the energy cascade is deeply altered, i.e. a substantial part of the energy income does not follow the classical Kolmogorov cascade towards viscous dissipation. Instead, it is moved to the micro-structures to feed an additional cascade (Vaithianathan and Collins [31], De Angelis et al. [50, 73], Jin [74]). A new component in the energy flux is introduced according to the Kármán-Howarth equation (De Angelis et al. [50, 73]) and the turbulent kinetic energy spectra at intermediate scales is reduced, while at high wavenumbers it is increased with the presence of polymers (Vaithianathan and Collins [31]). However, the DNS results of Berti et al. [75] suggested that polymers only partially suppress the turbulent cascade below the Lumley scale, and the velocity at large scales is found to be unaffected and small-scale statistics, such as acceleration, display features typical of Newtonian fluid turbulence.

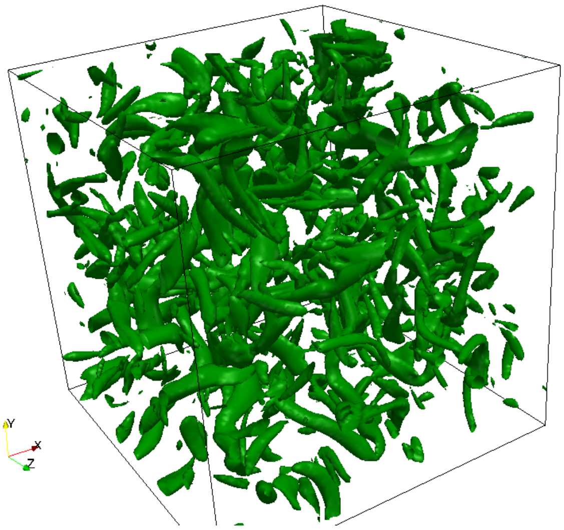

Figure 5.6: Iso-surfaces of the coherent structures in a periodic box of decaying homogeneous isotropic turbulence, for the Newtonian fluid case.

In DHIT with polymer additives, a remarkable alteration of the turbulent kinetic energy spectrum similar to that in FHIT (Vaithianathan and Collins [31]) appeared, and was interpreted based on the effective scale-dependent viscosity (Perlekar et al. [76]). Moreover, numerical simulation results showed that both the energy dissipation rate and intermittency in the dissipation range are reduced compared to its Newtonian fluid counterpart, and small-scale structures are suppressed (Perlekar et al. [76], Kalelkar et al. [77]). Based on the decrease in energy dissipation rate, Kalelkar et al. [77] proposed a definition of DR rate and found that DR rate increases with the polymer concentration, but decreases with Weissenberg number, inconsistent with that in turbulent channel flow. In a nutshell, the above numerical simulation results also show DR exists in HIT, and the important turbulence parameters change remarkably due to the addition of polymers which are qualitatively consistent with experimental results. These important previous studies were mainly focused on the DR phenomenon and the characteristics of HIT with polymer additives. However, how the flow structures interact with polymer micro-structures has still not been investigated in detail.

For the code to code comparison, DNS of low-Reynolds-number DHIT in a dilute polymer solution were carried out.

Table 5.2: Parameters for the simulations.

Cases	**Mesh** $(\mathbb{L}^3)$	$\nu^{[s]}(cm^2s^{-1})$	L	$\tau_p(s)$	β
A: Newt	64^3	10^{-2}	0	0	1
B: Visc-06	64^3	10^{-2}	100	0.1	0.6
C: Visc-07	64^3	10^{-2}	100	0.1	0.7
D: Visc-08	64^3	10^{-2}	100	0.1	0.8
E: Visc-09	64^3	10^{-2}	100	0.1	0.9

Table 5.2 shows the several runs and their parameters (similar to Cai et al. [70]).

As Cai did, here the initial energy spectrum and the initial conformation field were set to:

$$E_0(k) = 0.01k^4e^{-0.014k^2}, C_{ij}^0 = \delta_{ij} \tag{5.23}$$

In order to compare the code developed within this dissertation with the code of Cai et al. [70], different quantities are going to be addressed hereafter. These quantities are: Taylor microscale λ, energy dissipation rate ε, total turbulent kinetic energy ξ, conformation tensor trace r^2, turbulent kinetic energy spectra $E(k)$ and enstrophy Ω.

It is important to emphasize that the comparison done within this dissertation is just qualitative, once in Cai et al. [70] the definitions of some quantities are not disclosed and the time normalization is not clear. Giving this fact, for the quantities referred above, only the behaviours are comparable. Also, for a simpler and more efficient comparison all the quantities, with exception of energy spectra, are normalized by their initial value.

5.2.1 Taylor microscale

Starting from the beginning, Taylor microscale is a very important parameter in DHIT and is computed as follows:

$$\lambda = \sqrt{\frac{15\nu\xi}{\varepsilon}} \tag{5.24}$$

in which ε and ξ are given by:

FOURIER SPACE:

$$\varepsilon(t) = \nu^{[s]} \sum_k k^2 E(k,t) \tag{5.25}$$

$$\xi(t) = \sum_k E(k,t) \tag{5.26}$$

PHYSICAL SPACE:

$$\varepsilon(t) = \int_{\mathbb{L}^3} \nu^{[s]} \left(\frac{\partial u_i}{\partial x_j}\right)^2 dV \tag{5.27}$$

$$\xi(t) = \int_{\mathbb{L}^3} \frac{1}{2} u_i^2(\mathbf{x}, t) dV \tag{5.28}$$

The turbulent kinetic energy spectra, $E(k,t)$, is defined as follows:

$$E(k,t) = \frac{1}{2} \sum_{k-1/2<k'\leq k+1/2} |u_i(k,t)|^2 \tag{5.29}$$

As it is possible to see in Figure 5.7, Taylor microscale decreases at first and then grows quickly which implies the development of small-scale structures occurring in the energy propagation period (EPP) and the decay of small-scale structures in the energy decay period (EDP) (Kraichnan [78]). Further, in EPP $\lambda^{[P]} \approx \lambda^{[N]}$ (the superscripts 'P' and 'N' represent, respectively, the polymer solution case and the Newtonian fluid case) and in EDP $\lambda^{[P]} > \lambda^{[N]}$, suggesting that the decay of small-scale structures in the polymer solution case is faster than that in the Newtonian fluid case, i.e. an inhibition of turbulent motions at small scales. It can be regarded as the polymer's effect on flow structures and an origin of DR.

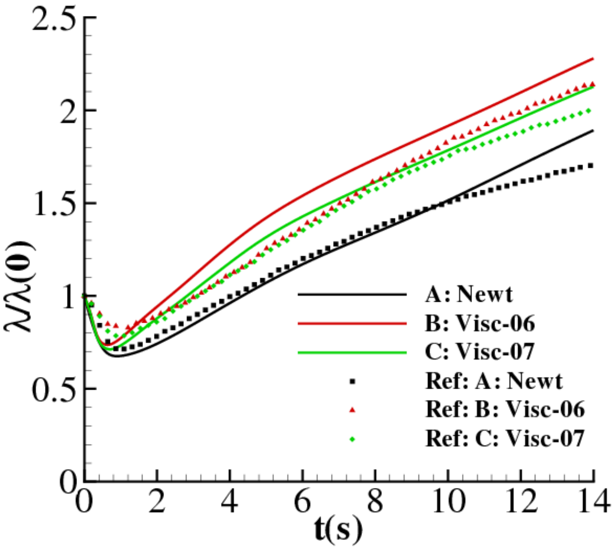

Figure 5.7: Temporal evolution of the Taylor microscale λ for cases A: Newt, B: Visc-06 and C: Visc-07 (see Table 5.2). Comparison with results obtained by Cai et al. [70].

Comparing the results obtained with the code developed within this thesis and the code here used as reference, the trends are the same, which means that the results are reasonably identical.

From Figure 5.7, it is possible to see that the minimum values occur later in Cai's results which is due to the time normalization Cai does. Other point that can also be a consequence of the normalization, now in λ, is that in EPP the results are below the reference and in EDP above the reference. This difference is more evident as time increases, which is consistent with what was said before.

5.2.2 Energy dissipation rate

Another quantity that is important to compare is the energy dissipation rate, ε, defined in equations (5.25) and (5.27).

Figure 5.8 clearly shows that, due to the energy-absorption effect of polymers, the viscous dissipation rate in the polymer solution case is smaller. The decrease of energy dissipation rate corresponding to the non-linearity of turbulence further proves the existence of the DR effect from another point.

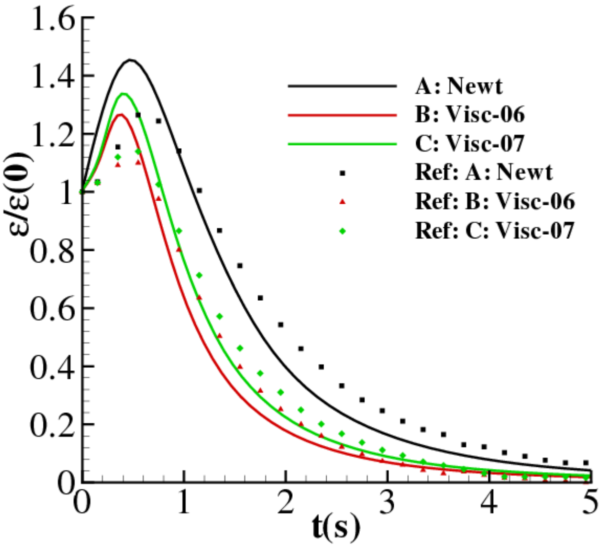

Figure 5.8: Temporal evolution of the energy dissipation rate ε. See Table 5.2 with the parameters of the simulations.

From Figure 5.8, as it was mentioned for Taylor microscale, there is a difference in t and in ε between the maximum values of both solutions which, on one hand, is justified by the normalization taken here and, on the other hand, is due to different definitions for this quantity. Despite these differences, the results here obtained follow well the reference and, qualitatively, the results of the three simulations behave as expected when comparing the position of each curve in relation with the other two.

5.2.3 Turbulent kinetic energy

Figure 5.9 gathers the results got from the code and the reference results, for the turbulent kinetic energy, ξ (see equations (5.26) and (5.28)).

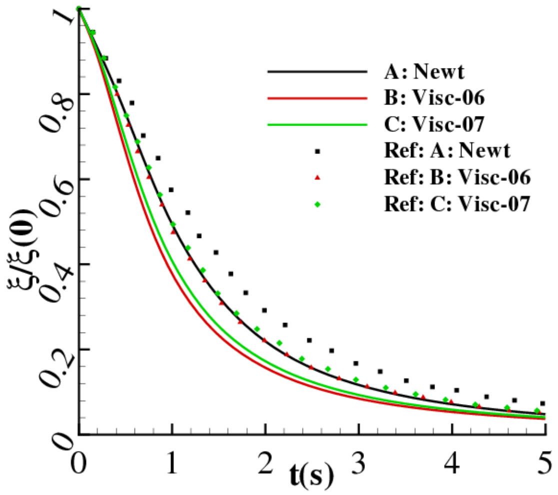

Figure 5.9: Temporal evolution of the total turbulent kinetic energy ξ. See Table 5.2 with the parameters of the simulations.

It is possible to identify two different regions in Figure 5.9 which correspond to different slopes. In the first region, the viscoelastic simulations tend to increase the distance to the Newtonian simulation. This means the turbulent kinetic energy decreases faster when in presence of polymer than in the absence of it, because polymers shift from the equilibrium to a stretched state, due to the development of small-scale structures, and absorb part of the turbulent kinetic energy (Cai et al. [70], De Angelis et al. [73]). In the second region, it is observed the reverse, i.e. the slopes of the viscoelastic simulations are lower (absolute value) than the newtonian's slope. This happens because polymers can not be stretched as much as in the first region so that polymers may release a part of the elastic energy and absorb less energy from flow structures. Globally, the results show that turbulent kinetic energy is always lower with polymer additives, except in the beginning (all simulations start from the same point and conditions) and in the end because the effect of the polymer decreases with time.

About the trends, having into account what was said before with respect to quantitative comparisons, they seem very good and equal to the reference.

5.2.4 Conformation tensor trace

It was also compared the temporal evolution of mean conformation tensor trace with different concentrations, as shown in Figure 5.10. It shows that during the EPP the mean relative extension is almost the same and decreases with the polymer concentration during the EDP. The reason is that for larger polymer concentration more marked DR occurs, and at the same time the mean velocity gradient generated by turbulent fluctuations weakens, leading to a smaller polymer extension.

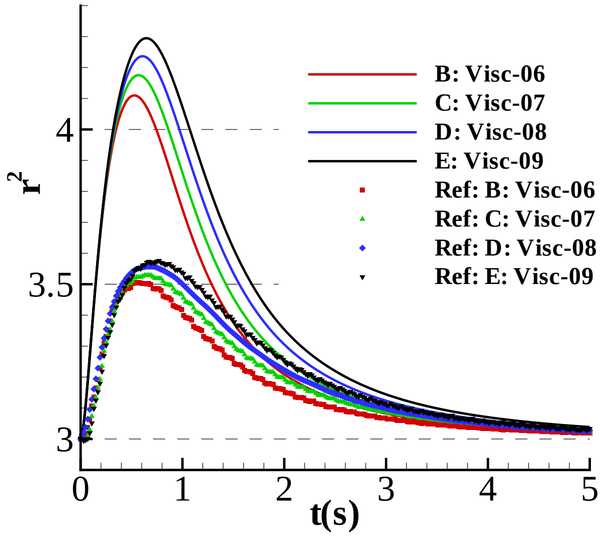

Figure 5.10: Temporal evolution of the mean conformation tensor trace r^2. See Table 5.2 with the parameters of the simulations.

In the beginning $r^2 = 3$ (see equation (5.23)) because it is the equilibrium state and the initial conformation field is set in that way. As time increases, the turbulent energy decays, the contribution of the polymer stresses will eventually become smaller than the Newtonian solvent stress, at which point the system reverts back to a Newtonian fluid. This is clear in Figure 5.10, which shows that r^2 approaches 3 (i.e., the equilibrium value) at long times.

5.2.5 Energy spectra

For the classical turbulent energy cascade in the Newtonian fluid turbulent flow, larger-scale structures transfer the turbulent kinetic energy into smaller-scale structures until the smallest scale (dissipative scale), where the energy is exhausted as heat loss due to viscosity.

To investigate the multiscale interaction between flow structures and polymer microstructures, Cai et al. [70] pays attention to the energy spectra, $E(k)$, in Fourier space.

He observes that, during the EPP, non-linear energy transfer dominates and the energy is transferred from small wavenumbers to large wavenumbers so as to raise the tail of energy spectra, but during the EDP, the viscous effect dominates so that the dissipation always lowers the tail of energy spectra. However, Cai shows that $E^{[P]}(k)$ is apparently different from $E^{[N]}(k)$, especially in the EDP, where $E^{[P]}(k) < E^{[N]}(k)$ at large and intermediate scales and $E^{[P]}(k) > E^{[N]}(k)$ at small scales. Besides, Cai obtains a nearly constant $E^{[P]}(k)$ at some scales range, i.e. the polymer dominant scale range, and this range becomes wider with advancing time, indicating that the turbulent kinetic energy transfer process for the Newtonian fluid flow which has been modified in DHIT with polymer additives is consistent with the experimental results of Fabula [40], van Doorn et al. [43] and numerical results of Vaithianathan and Collins [31], Perlekar et al. [76], De Angelis et al. [79].

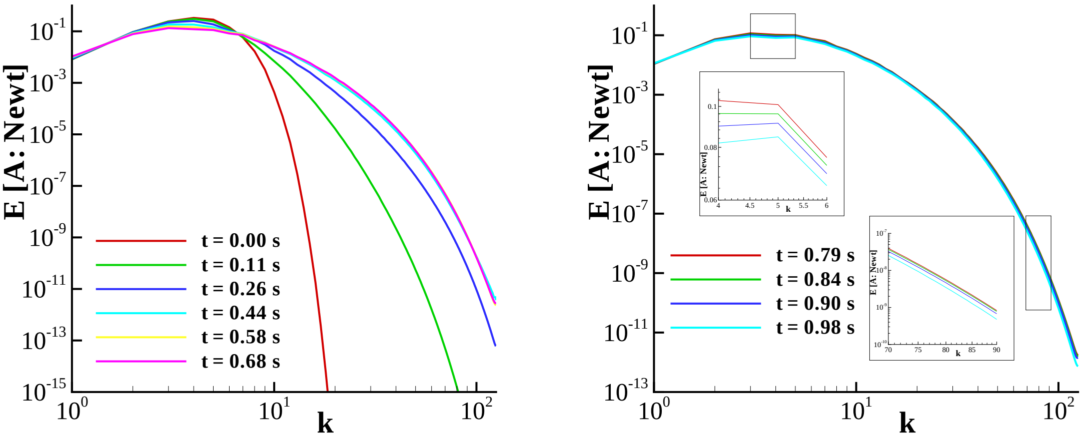

(a) Energy propagation period.

(b) Energy decay period.

Figure 5.11: Turbulent kinetic energy spectra $E(k)$ for the Newtonian fluid case. See Table 5.2 with the parameters of the simulations.

The temporal evolution of $E(k)$ in the Newtonian fluid and polymer solution cases obtained within this dissertation are shown in Figures 5.11 and 5.12, respectively. It is important to notice that this energy spectra were obtained with a finer mesh (256^3) than the mesh used for the other results. All the parameters indicated in Table 5.2 are valid except the mesh. Hence, all the results present in this subsection, "Energy spectra", were obtained for a mesh with 256 points in each direction. The reason behind this is that with finer meshes, more scales, and smaller, are present and this is crucial to compare the Newtonian fluid and polymer solution cases, once the major role of the polymer is played in the smallest scales.

From Figures 5.11 and 5.12, one can easily conclude that, for the EPP (Figure 5.11(a) for the Newtonian fluid case and Figure 5.12(a) for the polymer solution case), energy is being transferred from the large scales to the small scales. This is true in the presence and absence of polymer additives and it is possible to see because, as time increases, the energy spectrum becomes flatter, with less energy for small/intermediate wavenumbers and more energy for large wavenumbers.

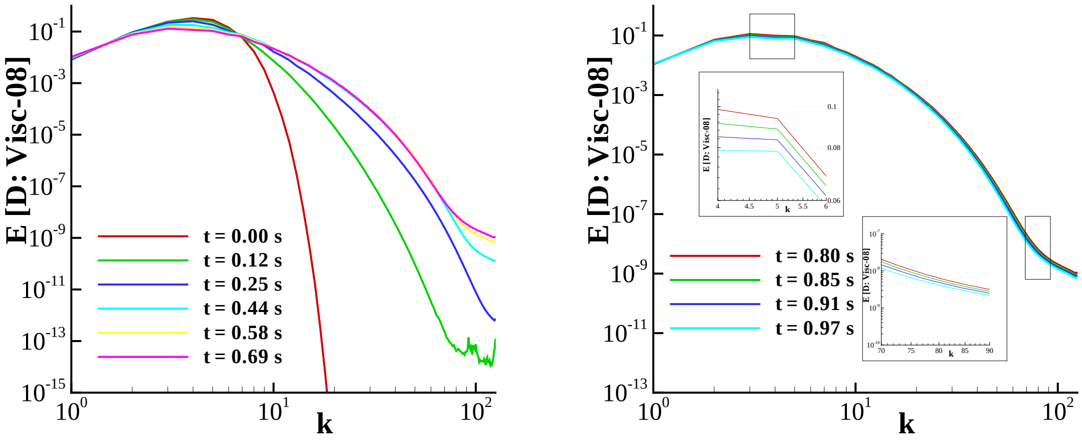

(a) Energy propagation period.

(b) Energy decay period.

Figure 5.12: Turbulent kinetic energy spectra $E(k)$ for D: Visc-08. See Table 5.2 with the parameters of the simulations.

In the EDP period - Figures 5.11(b) and 5.12(b) - a different process occurs, i.e. as time increases all scales lose energy comparing with the previous spectrum. This is according to what is the classic idea of energy cascade (for the Newtonian fluid case) and with Cai et al. [70].

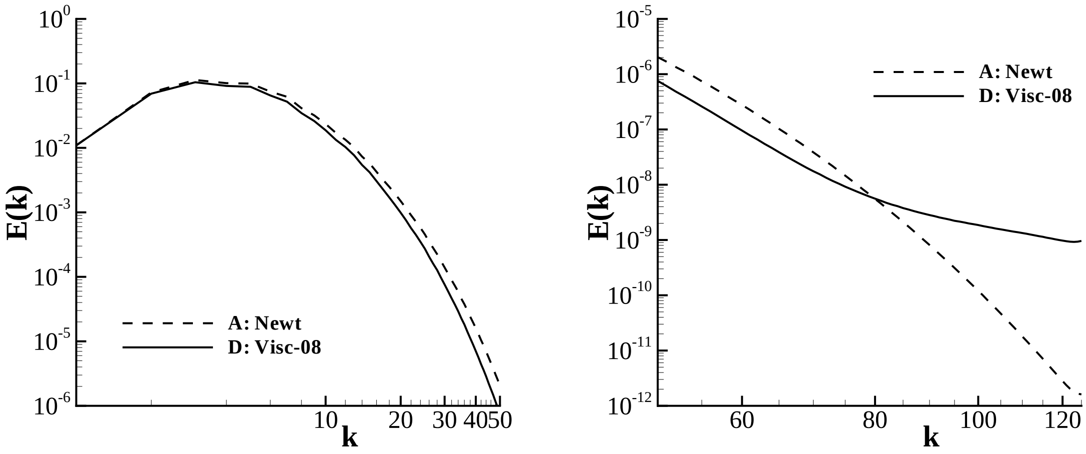

(a) Largest scales.

(b) Smallest scales.

Figure 5.13: Energy spectra for A: Newt and D: Visc-08, with $\mathrm{Re}_\lambda = 26$ ($t = 0.78s$, already in the EDP). See Table 5.2 with the parameters of the simulations.

In order to compare both cases, Newtonian fluid and polymer solution cases, one energy spectrum of each case is shown in Figures 5.13(a) and 5.13(b) for $\mathrm{Re}_\lambda = 26$. Figure 5.13(a) shows that in the Newtonian fluid case there is more energy in the largest scales than in the viscoelastic case. However, a completely different thing happens when analysing the behaviour of the smallest scales. Figure 5.13(b) shows that for the smallest scales, there is more energy in the viscoelastic case than in the Newtonian case, unlike what was seen for the largest scales. This is consistent with the results obtained by Vaithianathan and Collins [31], Cai et al. [70], De Angelis et al. [79].

5.2.6 Enstrophy

The temporal evolution of the enstrophy, Ω, in both the Newtonian fluid and polymer solution cases are shown in Figure 5.14.

The enstrophy is given by:

$$\Omega = \frac{\omega_i \omega_i}{2}, \tag{5.30}$$

where, ω_i is the vorticity defined as follows:

$$\omega = \nabla \times \mathbf{u} \tag{5.31}$$

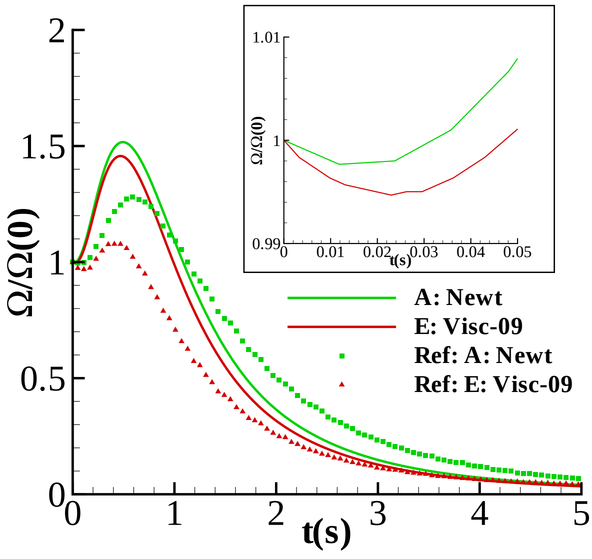

Figure 5.14: Temporal evolution of the enstrophy Ω. See Table 5.2 with the parameters of the simulations.

In the EPP, Ω increases and vortex structures are stretched, indicating the generation of the small-scale vortex structures. In the EDP, Ω decreases, indicating the suppression and dissipation of the vortex structures. It is consistent with the temporal evolution of the turbulent kinetic energy spectra (showing in the EPP the turbulent kinetic energy of small-scale structures increases and in the EDP the turbulent kinetic energy of all scales decreases, as mentioned previously - see Figures 5.11 and 5.12). In both EPP and EDP, the enstrophy in polymer solution case is remarkably weak compared with its Newtonian counterpart.

In summary, adding polymer additives to DHIT reduces the intensity of the growth of the enstrophy, so as to produce the drag-reducing phenomenon.

Comparing the results obtained here with the reference, all the comments already done about this fit perfectly here.

6

Results

Contents

This chapter is fully dedicated to new results obtained with the code developed within this thesis and can be divided in two main sections: general results and energy cascade analysis.

As the codes are validated - see chapter ”Verification and code to code comparison” - according to what was said before and is being shown in the next sections, new studies were carried out.

In the same trend of DHIT, new DNS of low Reynolds number were carried out for both solutions, with and without polymer additives.

At first place, general results are presented so that it is possible to see what are the main topological differences when comparing Newtonian and viscoelastic solutions.

To explore how the flow is influenced by drag-reduction polymer additives and how polymers contact with flow structures, the energy cascade is analysed in detail. This analysis enables a deeper knowledge about how much energy goes to the polymer, or how much comes from it, and what happens to the classical cascade. To do this, the transport equations, with polymer additives, for both the grid-scale (GS) and subgrid-scale (SGS) kinetic energy are derived and some terms are analysed in detail.

Table 6.1 summarizes the parameters of the simulations used in this chapter.

Table 6.1: Parameters for the simulations.

Cases	**Mesh** $(\mathbb{L}^3)$	$\nu^{[s]}(cm^2 s^{-1})$	L	$\tau_p(s)$	β
A: Newt	128^3	10^{-2}	0	0	1
B: Visc-06	128^3	10^{-2}	100	0.1	0.6
C: Visc-07	128^3	10^{-2}	100	0.1	0.7
D: Visc-08	128^3	10^{-2}	100	0.1	0.8

6.1 General results

As all the quantitative results were already shown and discussed in the previous chapter, ”Verification and code to code comparison”, this section is completely dedicated to the qualitative analysis of the coherent structures for both Newtonian fluid and polymer solution cases, with different values of β.

Two time instants in the EDP are analysed. Figures 6.1(a), 6.1(b) and 6.1(c) are related to the first time instant whereas Figures 6.2(a), 6.2(b) and 6.2(c) are related to the second. These figures show iso-surfaces of positive Qi criterion which is the second invariant of the velocity gradient tensor, $Qi = (1/2)\left(\Omega_{ij}\Omega_{ij} - S_{ij}S_{ij}\right)$.

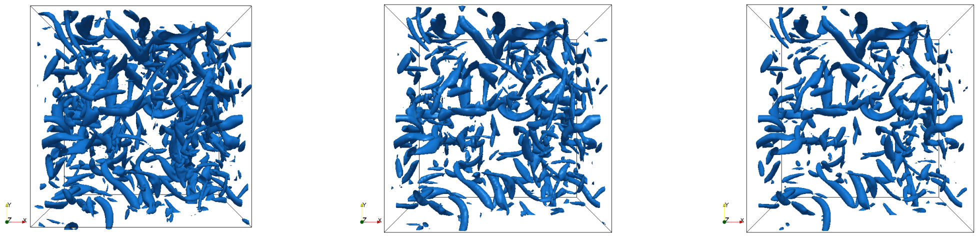

(a) A: Newt - $t = 0.61s$ and $\mathrm{Re}_\lambda = 28.4$.
(b) D: Visc-08 - $t = 0.70s$ and $\mathrm{Re}_\lambda = 27.0$.
(c) C: Visc-07 - $t = 0.71s$ and $\mathrm{Re}_\lambda = 27.0$.

Figure 6.1: The threshold of Qi criterion is: **(a)** 100; **(b)** 100; **(c)** 100.

It can be observed that for the polymer solution cases, an inhibition of the small-scale structures occurs. And this is more evident for lower values of β. With advancing time, the strength of the tube-like vortex structures decreases for all the cases, but decreases faster for the viscoelastic cases, i.e. the lower the β the faster the decay. Hence, the presence of polymer additives in the solutions suppresses the smallest resolved scales of motion.

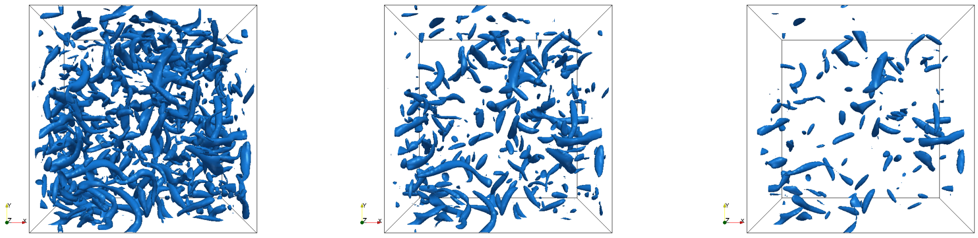

(a) A: Newt - $t = 1.52s$ and $\mathrm{Re}_\lambda = 18.9$.
(b) D: Visc-08 - $t = 1.55s$ and $\mathrm{Re}_\lambda = 19.3$.
(c) C: Visc-07 - $t = 1.61s$ and $\mathrm{Re}_\lambda = 19.4$.

Figure 6.2: The threshold of Qi criterion is: **(a)** 50; **(b)** 50; **(c)** 50.

6.2 Energy cascade analysis

Energy cascade was introduced by Richardson in 1922 and briefly the idea is that kinetic energy enters the turbulence (through the production mechanism) at the largest scales of motion. This energy is then transferred (by inviscid processes) to smaller and smaller scales until, at smallest scales, the energy is dissipated by viscous action.

Richardson summarized the idea of the energy cascade in the following way (Pope [80]):

`Big whorls have little whorls,`
`Which feed on their velocity;`
`And little whorls have lesser whorls,`
`And so on to viscosity`
`(in the molecular sense).`

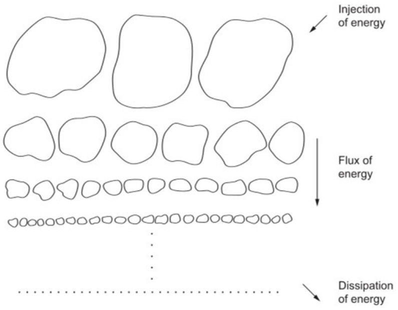

Figure 6.3: Illustration of the energy cascade described on the left.

With the presence of polymers, the energy cascade is different from the one described earlier. As it was already mentioned, and based on Cai et al. [70], Casciola and De Angelis [81], polymers absorb turbulent kinetic energy from large and intermediate scales flow structures to feed the micro-structure at a different scale and dissipate it by elasticity and at small scales the energy is transferred from polymer micro-structures to the small-scale flow structures.

The main goal of this section, and of this dissertation in general, is to understand the routes of the turbulent kinetic energy, i.e. the interaction between GS and SGS, between SGS and the polymer.

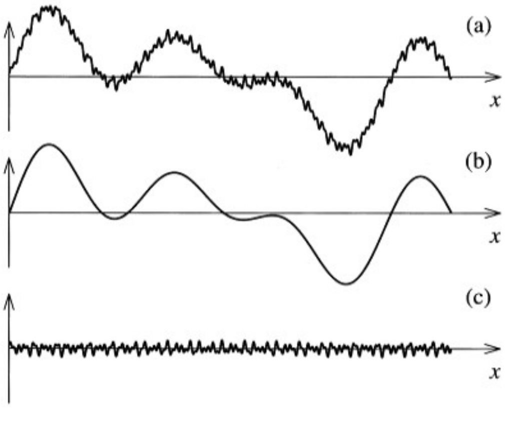

Figure 6.4: Filtering operator applied to the function represented in (a). (a) function $f(x)$ (b) GS part $\overline{f(x)}$ (c) SGS part $f(x)'$. From Frisch [82].

In order to understand the interaction between GS and SGS, all the scales are decomposed into a GS part ($\overline{f}$) and a SGS part (f') by applying a spatial filtering operator to the equations to be solved.

The filtering operator is defined by:

$$\overline{f(x)} = \int_{\mathbb{L}^3} f(s) G_\Delta(x-s) ds \tag{6.1}$$

$$\int_{\mathbb{L}^3} G_\Delta(x) dx = 1, \tag{6.2}$$

where $G_\Delta(x)$ is a filter of width Δ, $f(x)$ represents any flow variable and the integration is carried out over the whole domain, $\mathbb{L}$. Hence, it is necessary to do the following decomposition:

$$u_i = \overline{u_i} + u_i' \tag{6.3}$$

$$p = \overline{p} + p' \tag{6.4}$$

Once in presence of polymer additives, one more decomposition must be done:

$$T_{ij}^{[p]} = \overline{T_{ij}^{[p]}} + T_{ij}^{[p]\prime} \tag{6.5}$$

By now, it is important to notice that, at first place, the analysis has to be macroscopic and that is why the decomposition is done in $T_{ij}^{[p]}$ and not in C_{ij}. With this decomposition it is possible to look to the energy cascade and see what are the main influences caused by the presence of polymer. With the decomposition in C_{ij}, macroscopic informations - as GS/SGS interactions due to classical cascade and polymer induced cascade and SGS/polymer interactions - are still present but a lot more information is also in the scope - as interactions between polymer GS and SGS. The microscopic analysis is not done in this thesis due to the level of detail required and because it was considered more important to have first a full scope. However, the equations derived for the microscopic analysis can be found in Appendix A.

The resulting filtered Navier-Stokes equations are:

$$\frac{\partial \overline{u_i}}{\partial t} + \frac{\partial \overline{u_i} \cdot \overline{u_j}}{\partial x_j} = -\frac{1}{\rho}\frac{\partial \overline{p}}{\partial x_i} + \nu^{[s]} \frac{\partial}{\partial x_j}\left(\frac{\partial \overline{u_i}}{\partial x_j} + \frac{\partial \overline{u_j}}{\partial x_i}\right) - \frac{\partial \tau_{ij}}{\partial x_j} + \frac{1}{\rho}\frac{\partial \overline{T_{ij}^{[p]}}}{\partial x_j} \tag{6.6}$$

$$\frac{\partial \overline{u_i}}{\partial x_i} = 0 \tag{6.7}$$

In equation (6.6), τ_{ij} is the unknown subgrid-stress tensor responsible for the momentum exchanges between the subgrid and the filtered scales. In a LES approach, this term has to be modelled. τ_{ij} is given by:

$$\tau_{ij} = \overline{u_i u_j} - \overline{u_i} \cdot \overline{u_j} \tag{6.8}$$

After decomposing the flow variables and writing out the Navier-Stokes equations, in order to study GS/SGS interaction, the next step consists of writing out the transport equations for (twice) the total GS and SGS kinetic energy (Piomelli et al. [83], Piomelli and Chasnov [84], da Silva and Métais [85]).

The transport equation for (twice) the GS kinetic energy, $\overline{u_i} \cdot \overline{u_i}$, is given by:

$$\underbrace{\frac{\partial \overline{u_i} \cdot \overline{u_i}}{\partial t}}_{A} + \underbrace{\frac{\partial \overline{u_i} \cdot \overline{u_i} \cdot \overline{u_j}}{\partial x_j}}_{B} = \underbrace{-\frac{2}{\rho} \frac{\partial \overline{p} \cdot \overline{u_i}}{\partial x_i}}_{C} \underbrace{+ \nu^{[s]} \frac{\partial}{\partial x_j} \left(\frac{\partial \overline{u_i} \cdot \overline{u_i}}{\partial x_j} \right)}_{D} \underbrace{-2\nu^{[s]} \frac{\partial \overline{u_i}}{\partial x_j} \frac{\partial \overline{u_i}}{\partial x_j}}_{E} \underbrace{-2 \frac{\partial \tau_{ij} \overline{u_i}}{\partial x_j}}_{F} + \underbrace{2 \tau_{ij} \overline{S_{ij}}}_{G} + \\ \underbrace{+ \frac{2}{\rho} \frac{\partial \overline{T_{ij}^{[p]}} \cdot \overline{u_i}}{\partial x_j}}_{H} \underbrace{- \frac{2}{\rho} \overline{T_{ij}^{[p]}} \cdot \overline{S_{ij}}}_{I} \tag{6.9}$$

The transport equation for the SGS kinetic energy, τ_{ii}, is:

$$\underbrace{\frac{\partial \tau_{ii}}{\partial t}}_{J} + \underbrace{\frac{\partial \tau_{ii} \overline{u_j}}{\partial x_j}}_{K} = \underbrace{\frac{\partial}{\partial x_j} \left(\overline{u_i u_i} \cdot \overline{u_j} - \overline{u_i u_i u_j} \right)}_{L} + \underbrace{\frac{2}{\rho} \frac{\partial}{\partial x_i} \left(\overline{p} \cdot \overline{u_i} - \overline{p u_i} \right)}_{M} + \underbrace{\frac{\partial}{\partial x_j} \left(\nu^{[s]} \frac{\partial \tau_{ii}}{\partial x_j} \right)}_{N} + \\ \underbrace{-2\nu^{[s]} \left(\overline{\frac{\partial u_i}{\partial x_j} \frac{\partial u_i}{\partial x_j}} - \frac{\partial \overline{u_i}}{\partial x_j} \frac{\partial \overline{u_i}}{\partial x_j} \right)}_{O} + \underbrace{2 \frac{\partial \tau_{ij} \overline{u_i}}{\partial x_j}}_{P} \underbrace{-2 \tau_{ij} \overline{S_{ij}}}_{Q} + \\ \underbrace{+ \frac{2}{\rho} \frac{\partial \overline{T_{ij}^{[p]} u_i}}{\partial x_j}}_{R} \underbrace{- \frac{2}{\rho} \frac{\partial \overline{T_{ij}^{[p]}} \cdot \overline{u_i}}{\partial x_j}}_{S} \underbrace{- \frac{2}{\rho} \overline{T_{ij}^{[p]} S_{ij}}}_{T} + \underbrace{\frac{2}{\rho} \overline{T_{ij}^{[p]}} \cdot \overline{S_{ij}}}_{U} \tag{6.10}$$

It is important to recall the physical meaning of these equations and their respective terms. In equation (6.9), terms A and B account for the total (local and convective) variation of GS kinetic energy. Terms C and D account for the redistribution (diffusion) of GS kinetic energy by pressure/velocity interactions and molecular viscosity, respectively. Term E is the local GS kinetic energy dissipation due to the molecular viscosity. The terms F and G are the only terms involving the subgrid-stress tensor τ_{ij} and are directly related to the kinetic energy exchanges between GS and SGS. These two terms define the classical energy cascade, i.e. the cascade that exists in a viscoelastic turbulent flow but is not induced directly by the polymer. Term F (GS/SGS diffusion) represents a redistribution of GS kinetic energy by interactions between the GS velocity and the SGS stresses. The GS/SGS transfer (term G) also called subgrid-scale dissipation, represents the transfer of kinetic energy between GS and SGS. If term G is positive, kinetic energy goes from SGS to GS (also called backward scatter), otherwise, GS give energy to SGS (forward scatter). In Newtonian fluid case, although there are both cascades occurring at the same time, forward scatter is dominant - roughly speaking, 40% of the points have positive values of G which is a good indicator that backward scatter exists and can not be neglected. When in presence of polymer additives, two new terms must be accounted to study GS kinetic energy and specially GS/SGS interactions. Terms H and I are topologically similar to terms F and

G, respectively. Term H, hereafter called GS/SGS diffusion induced by the polymer, represents local energy transfer between GS and SGS in which polymer plays the major role. The same happens with term I, GS/SGS transfer induced by the polymer, which accounts for kinetic energy exchanges between GS and SGS induced by the presence of polymer in the solution. Again, term I positive means backward scatter, and term I negative means forward scatter. So far, two energy cascades are present concerning viscoelastic turbulent flows.

In equation (6.10), terms J and K represent the local and convective variation of the SGS kinetic energy, respectively. The diffusion caused by the local turbulence level on the SGS kinetic energy is represented by term L (SGS turbulent transport). Term M is the SGS pressure/velocity interactions and N is the SGS viscous diffusion. Term O (SGS viscous dissipation) represents the end of the classical energy cascade process where molecular viscosity finally dissipates the remaining SGS kinetic energy. This term accounts only for the energy dissipated, by viscosity, by SGS. Hence, this term does not mean all dissipation because polymer dissipation is not taken into account in equation (6.10). It is important to notice that the terms P and Q are, respectively, the opposites of the terms F and G. Since these terms appear in both equations with opposite signs, they represent the kinetic energy exchange between GS and SGS, as stressed above. The same happens with terms H, I and S, U, respectively. However, there are two new terms in equation (6.10), R and T, that seem like diffusion and transfer terms but they do not have correspondence in equation (6.9). Term R quantifies the SGS/Polymer diffusion, i.e. local energy transfer between flow small scales and polymer structure. Finally, term T represents the SGS/Polymer transfer.

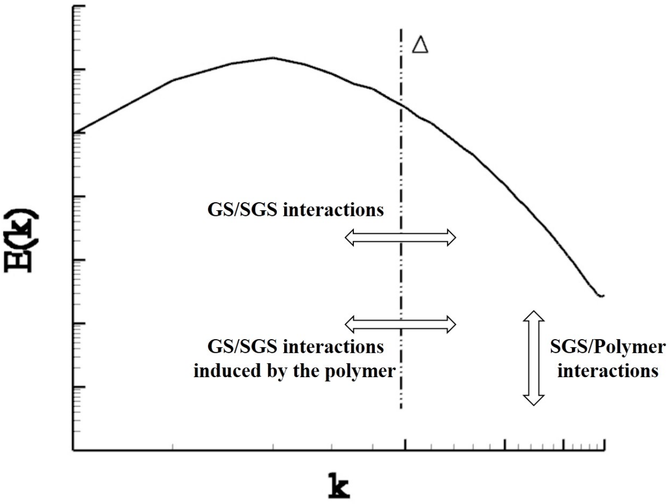

Figure 6.5: Schematic representation of the interactions among GS, SGS and polymer, in the energy spectrum.

In Figure 6.5, it is represented the interactions among GS, SGS and polymer. In order to classify better these interactions, a deeper analysis is necessary. In this section, terms P and

Q (classical energy cascade), S and U (GS/SGS interaction induced by the polymer), R and T (SGS/Polymer interaction) are studied minutely. The rest of the terms are not addressed in this thesis.

At first place, terms P, Q, S and T are analysed and comparisons between them are done. With this first analysis, the aim is to get an idea about how the cascades work, classical and viscoelastic, and what is the relative importance of them in the overall cascade.

After this, terms R and T are analysed and compared with the other terms mentioned previously. With this analysis, the goal is to get a better perception of the interactions between the SGS and the polymer.

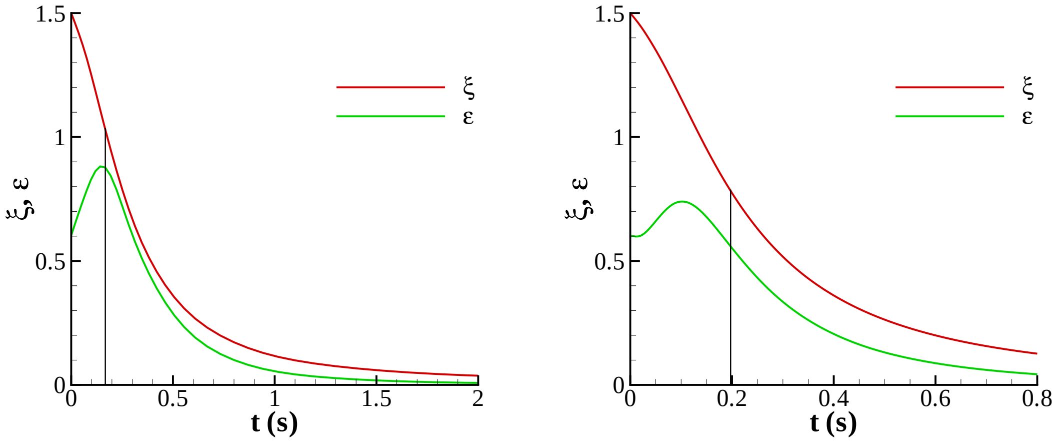

(a) A: Newt - Time instant picked for the analysis ($\mathrm{Re}_\lambda = 28.4$).

(b) B: Visc-06 - Time instant picked for the analysis ($\mathrm{Re}_\lambda = 27.0$).

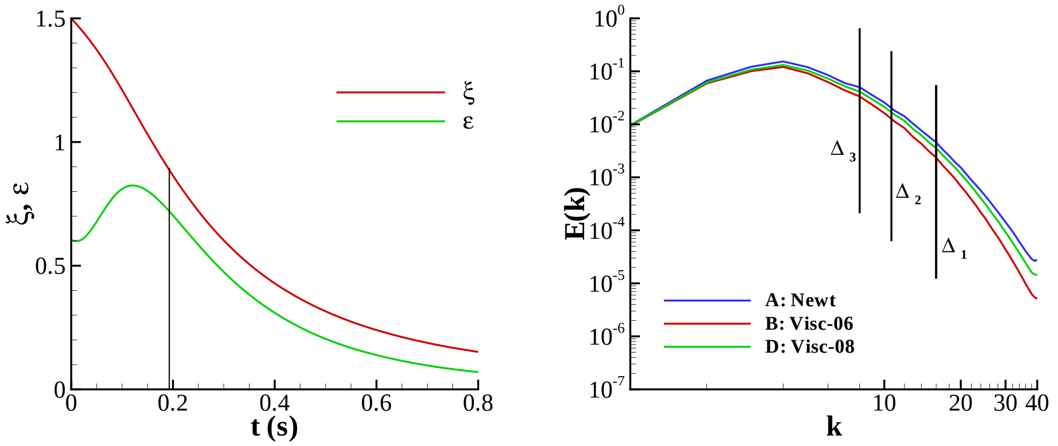

(c) D: Visc-08 - Time instant picked for the analysis ($\mathrm{Re}_\lambda = 27.0$).

(d) Energy spectra for the instants shown in subfigures **(a)**, **(b)** and **(c)** with all filters.

Figure 6.6: Time instants picked for the analysis and position of the filters in the energy spectra, for the three DHIT DNS of interest.

By now, it is important to refer how the GS and the SGS are going to be split, within this thesis. As this work is aimed at the study of the interactions between large and small scales, only a spatial filter can be used. Here, it is used a box or top-hat filter defined as follows:

$$G_{\Delta}(x-s)=\begin{cases} 1/\Delta & \text{if } |x-s|<\frac{1}{2}\Delta \\ 0 & \text{otherwise} \end{cases}$$

As pointed out by da Silva and Métais [85], using such a filter, in the subgrid-scales kinetic energy, there is a dominant contribution from the small scales, but also a smaller contribution from the grid scales, and vice versa for the grid-scale kinetic energy. Furthermore, a box filter is used because it is often used in large-eddy simulations.

The analysis referred before are done for three DHIT, DNS of low Reynolds number (A: Newt, B: Visc-06 and D: Visc-08 of Table 6.1) and for three filters, $\Delta_1/\Delta x = 4$, $\Delta_2/\Delta x = 6$ and $\Delta_3/\Delta x = 8$ (see Figure 6.6(d)).

Figures 6.6(a), 6.6(b) and 6.6(c) show the time evolution of the total turbulent kinetic energy ξ and the energy dissipation rate ε. These figures show the time instants picked for the analysis of each DNS. It is important to notice that the three instants belong to the EDP.

6.2.1 GS/SGS interactions

In this subsection, one-point statistics - see Figure 6.6 for the time instants - from simulations in Table 6.1 are presented in order to analyse the GS/SGS interactions. The terms that are going to be analysed are: F, G, H and I. However, to simplify further comparisons that are going to be done in this chapter, all the text, figures and tables are referred to the symmetric terms, i.e. terms P, Q, S and U that appear in equation (6.10).

For the selected time instants and for each term, mean, variance, skewness and flatness are computed. Using the classical Reynolds decomposition of each term $V = \langle V \rangle + V'$, where $\langle\rangle$ and the prime designate mean and fluctuating values, respectively, the skewness s_f and the flatness f_f factors were made non-dimensional by the variance,

$$s_f = \frac{\langle V'^3 \rangle}{\left[\langle V'^2 \rangle^{1/2}\right]^3}, \tag{6.11}$$

$$f_f = \frac{\langle V'^4 \rangle}{\left[\langle V'^2 \rangle^{1/2}\right]^4} \tag{6.12}$$

In addition to this, probability density functions (PDFs), joint PDFs and correlation coefficients were computed with the mentioned terms. The correlation coefficient between two variables X and Y is given by,

$$C_{(X,Y)} = \frac{\langle X'Y' \rangle}{\left[\langle X'^2 \rangle \langle Y'^2 \rangle\right]^{1/2}} \tag{6.13}$$

Table 6.2: Mean, variance, skewness and flatness values for each DNS and each term, with $\Delta/\Delta x = 4$ (top table), $\Delta/\Delta x = 6$ (table in the middle) and $\Delta/\Delta x = 8$ (bottom table).

	A: Newt	B: Visc-06	D: Visc-08
P	$(\sim 0, 2.673, 1.144, 20.140)$	$(\sim 0, 0.777, 1.189, 19.758)$	$(\sim 0, 1.523, 1.146, 19.714)$
Q	$(0.451, 0.695, 4.346, 43.750)$	$(0.258, 0.216, 3.904, 30.626)$	$(0.346, 0.407, 4.169, 37.273)$
S	-	$(\sim 0, 0.505, 0.080, 7.195)$	$(\sim 0, 0.115, 0.064, 9.994)$
U	-	$(0.539, 0.227, 2.472, 14.504)$	$(0.249, 0.054, 2.893, 20.670)$
P	$(\sim 0, 4.658, 0.723, 13.796)$	$(\sim 0, 1.543, 0.687, 13.660)$	$(\sim 0, 2.755, 0.655, 13.504)$
Q	$(0.646, 1.263, 3.498, 27.327)$	$(0.388, 0.441, 3.367, 23.207)$	$(0.502, 0.763, 3.439, 24.787)$
S	-	$(\sim 0, 0.285, 0.203, 5.609)$	$(\sim 0, 0.061, 0.193, 6.725)$
U	-	$(0.423, 0.115, 2.010, 10.320)$	$(0.191, 0.025, 2.247, 13.000)$
P	$(\sim 0, 5.379, 0.486, 10.940)$	$(\sim 0, 1.959, 0.361, 10.341)$	$(\sim 0, 3.251, 0.351, 10.163)$
Q	$(0.728, 1.502, 2.940, 18.898)$	$(0.454, 0.571, 3.048, 20.181)$	$(0.570, 0.924, 3.002, 19.520)$
S	-	$(\sim 0, 0.160, 0.321, 5.069)$	$(\sim 0, 0.033, 0.311, 5.634)$
U	-	$(0.324, 0.058, 1.738, 8.403)$	$(0.143, 0.012, 1.888, 10.067)$

Mean, variance, skewness and flatness factors are in Table 6.2. Table 6.3 has all the computed correlation coefficients.

Table 6.3: Correlation coefficients for **(left)** $\Delta/\Delta x = 4$ and **(right)** $\Delta/\Delta x = 8$.

	A: Newt	B: Visc-06	D: Visc-08
(Q, ε)	-0.84	-0.86	-0.84
(Q, P)	-0.31	-0.31	-0.31
(U, ε)	-	-0.87	-0.83
(U, S)	-	-0.61	-0.61

	A: Newt	B: Visc-06	D: Visc-08
(Q, O)	-0.66	-0.71	-0.67
(Q, P)	-0.43	-0.43	-0.44
(U, O)	-	-0.75	-0.70
(U, S)	-	-0.64	-0.63

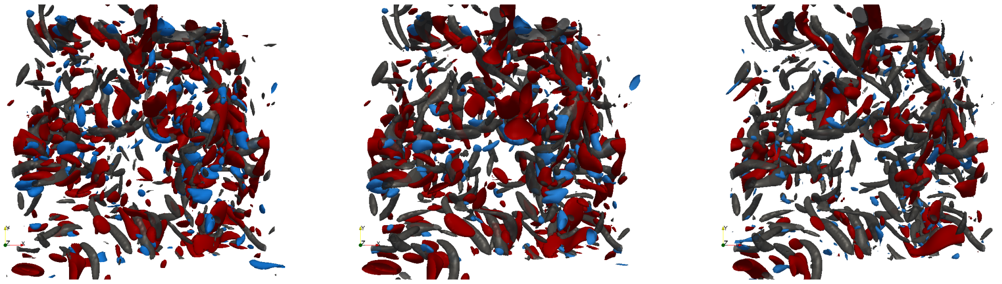

(a) A: Newt - Visualizations of term Q (positive/red and negative/blue) and positive Qi criterion (grey), for $\Delta/\Delta x = 6$.

(b) B: Visc-06 - Visualizations of term Q (positive/red and negative/blue) and positive Qi criterion (grey), for $\Delta/\Delta x = 6$.

(c) B: Visc-06 - Visualizations of term U (positive/red and negative/blue) and positive Qi criterion (grey), for $\Delta/\Delta x = 6$.

Figure 6.7: The threshold for term Q is the following: **(a)** red corresponds to 4, blue corresponds to -1; **(b)** red corresponds to 2.3, blue corresponds to -0.6. The threshold of term U is: **(c)** red is 1.5, blue is -0.01. Finally, the threshold of Qi criterion is: **(a)** 150; **(b)** 80; **(c)** 80.

As already stressed, terms P, Q, S and U represent the kinetic energy exchanges between GS and SGS. To have a first clue about how these terms behave, Figures 6.7(a) and 6.7(b) show iso-surfaces of term Q (red/positive and blue/negative) and positive Qi (coherent structures), for Newtonian fluid and polymer solution cases. As before, positive and negative surfaces of term Q - as well as for the others - represent forward and backward scatter, respectively. The first observation is that Q shows no clear sign of correlation with the coherent structures. This happens for both Newtonian and viscoelastic cases. A possible explanation for this fact can be the low Reynolds number. A different picture can be seen regarding term P, in Figures 6.8(a) and 6.8(b), because in this case, it is possible to see that the shape of the structures are similar and intense regions of term P are located next to the vortex cores (not in their centres). It is also interesting to highlight that, in Figures 6.8(a) and 6.8(b), the forward scatter (red iso-surfaces) is of comparable magnitude to backward scatter (blue iso-surfaces) as expected. In Figures 6.7(a) and 6.7(b), red surfaces are clearly dominant in the picture because forward scatter is the most relevant, but the backward scatter can not be neglected as it can be seen by the figures. For the Newtonian case, 23% of the points have negative values of term Q and this percentage can go to 40% in a flow with higher Reynolds number. When in presence of polymer additives, the ratio of negative/positive values is almost the same but lower (see Table 6.2), 21%. Figures 6.7(c) and 6.8(c), show the correlation between terms U and S with coherent structures. It is interesting to see that, again, the transfer term U does not show any clear correlation. As for P, also S is correlated with the presence of coherent structures.

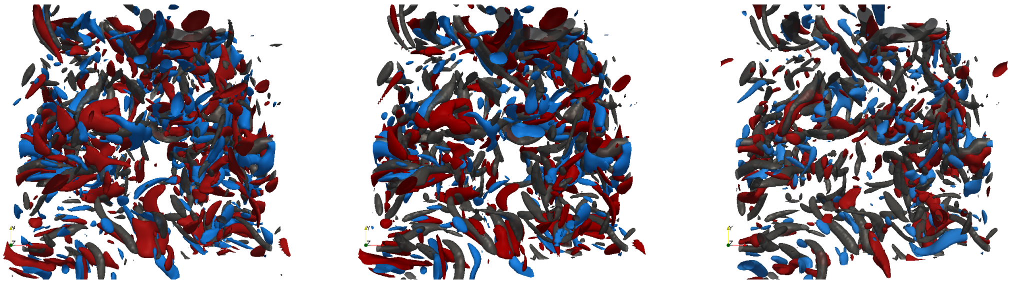

(a) A: Newt - Visualizations of term P (positive/red and negative/blue) and positive Qi criterion (grey), for $\Delta/\Delta x = 6$.

(b) B: Visc-06 - Visualizations of term P (positive/red and negative/blue) and positive Qi criterion (grey), for $\Delta/\Delta x = 6$.

(c) B: Visc-06 - Visualizations of term S (positive/red and negative/blue) and positive Qi criterion (grey), for $\Delta/\Delta x = 6$.

Figure 6.8: The threshold for term P is the following: **(a)** red corresponds to 5, blue corresponds to -5; **(b)** red corresponds to 3.2, blue corresponds to -3.2. The threshold of term U is: **(c)** red is 1.4, blue is -1.4. Finally, the threshold of Qi criterion is: **(a)** 150; **(b)** 80; **(c)** 80.

Figures 6.9(a) and 6.9(b) show values of the terms considered in this section, in one line along the domain, for both Newtonian and viscoelastic cases. Diffusion terms P and S have higher amplitudes, comparing to the transfer terms Q and U. Table 6.2 shows that diffusion terms have always higher variance values (measure the local fluctuating intensities) than transfer terms have. This is coherent with what Figures 6.9(a) and 6.9(b) show. Also, from Table 6.2, it is possible to see that diffusion terms have mean values very close to zero (as Figures 6.8(a) and 6.8(b) illustrate), which is patent in Figures 6.9(a) and 6.9(b). Comparing variance values of P for A: Newt and B: Visc-06 (see Table 6.2), it is clear that they are much smaller in the presence of polymer additives. Figures 6.9(a) and 6.9(b) also show this in the magnitudes of the peaks that are significantly lower in viscoelastic computations. These comments are still valid for terms S and U. Figure 6.9(b), and based on variance values of Q and U, shows that the classical cascade is the most relevant for this filter. However, it can be seen that as the filter size decreases, the relative importance of term U grows, because its variance value increases and the variance value of Q decreases.

Term Q represents the transfer between GS and SGS, and thus, the classical energy cascade. PDFs of Q are shown in Figures 6.10(a) and 6.10(b). Forward scatter dominates in both cases, but the backward scatter is also present, and can not be ignored. Backward scatter does not seem very sensitive to the filter size.

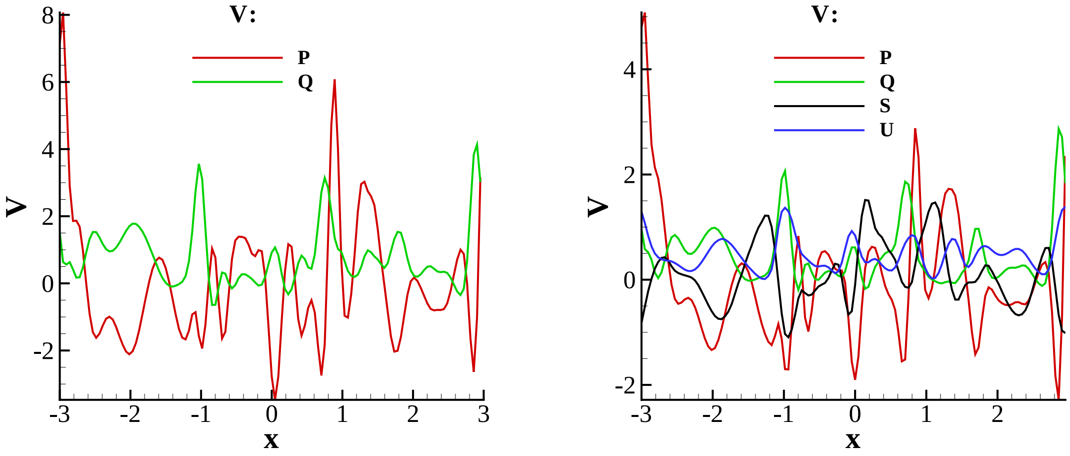

(a) A: Newt - One line in the middle of the domain with values of the terms P and Q, for $\Delta/\Delta x = 6$.

(b) B: Visc-06 - One line in the middle of the domain with values of the terms P, Q, S and U, for $\Delta/\Delta x = 6$.

Figure 6.9: Relevance of the terms directly related to GS/SGS interactions in Newtonian fluid and polymer solution cases.

With respect to the forward scatter, it seems obvious that extreme events are more likely to happen for smaller filters in which the small scales are more intermittent (higher flatness values). Also, it is interesting to see that for higher filters, more kinetic energy, in average, travels to the SGS and the PDF is more symmetric (skewness value closer to zero). When in the presence of polymer additives, one difference is obvious. The forward scatter seems less sensitive to the filter, the mean values increase less with the filter than in the Newtonian fluid case. Also, the flatness values are lower in viscoelastic and this can be seen in the behaviour smoother of the small scales in the extreme events (related with the highest gradients).

Figures 6.11(a) and 6.11(b) show PDFs of P. The largest scales behave almost independently of the filter size, because for the events with higher probability the curves are almost coincident. But for extreme events, the curves are different. Again, lower filter leads to higher intermittent nature (higher flatness values). Also, as the filter size decreases, variance values decrease as well, meaning that the intensity decreases. With lower filters size, higher values of skewness occur, and this is visible in Figures 6.11(a) and 6.11(b).

Terms U and S are shown in Figures 6.12(a) and 6.12(b), respectively. From Figure 6.12(a), it is possible to see that the topology of the curves are similar to the curves of the term Q. The figure unambiguously shows that the energy cascade induced by the polymer is, predominantly, from the GS to the SGS, as the classical energy cascade.

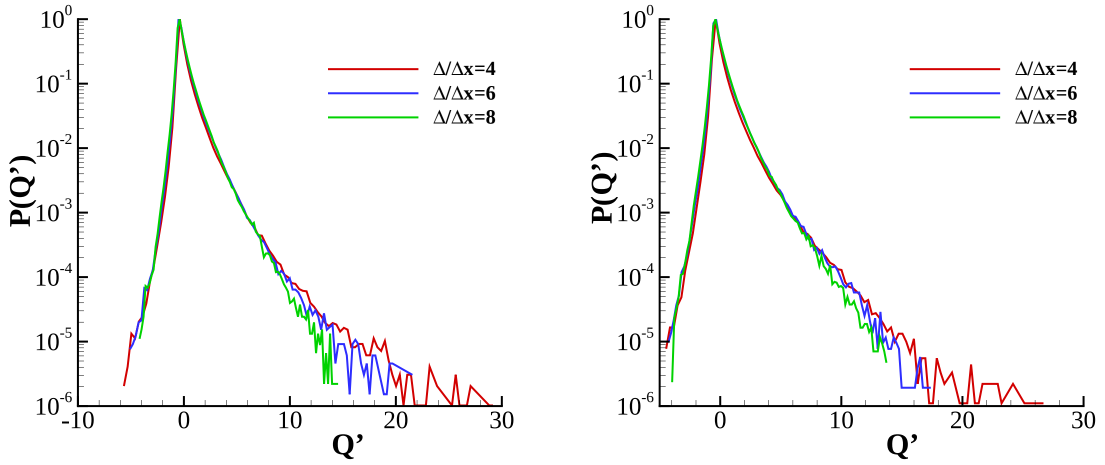

(a) A: Newt - GS/SGS transfer for all filters. **(b)** D: Visc-08 - GS/SGS transfer for all filters.

Figure 6.10: Probability density functions for the term Q, GS/SGS transfer, comparing the three filters.

However, there is a big difference between the two cascades: while Q increases in average with the filter, U decreases. This means that the polymer induces, in average, less energy to the SGS as the SGS range increases. This is very interesting because the polymer is expected to act mainly in the smallest scales of the SGS - as it is clearly shown in Figures 5.13(a) and 5.13(b) - and once the SGS range is enlarged, the polymer's effect is lower - as it can be seen in the decrease of the variance values.

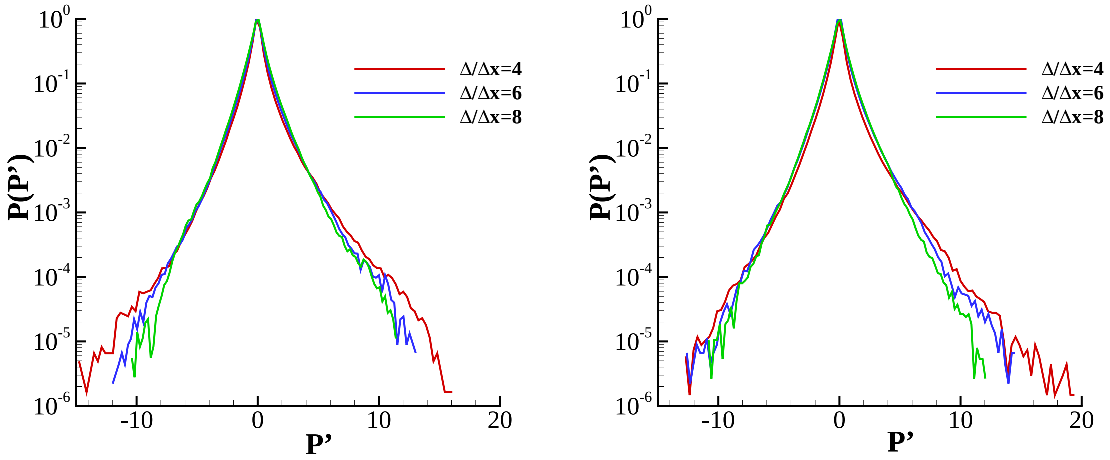

(a) A: Newt - GS/SGS diffusion for all filters.

(b) D: Visc-08 - GS/SGS diffusion for all filters.

Figure 6.11: Probability density functions for the term P, GS/SGS diffusion, comparing the three filters.

Regarding the term S, it is important to refer that the mean value is zero, as it is expected for a diffusion term.

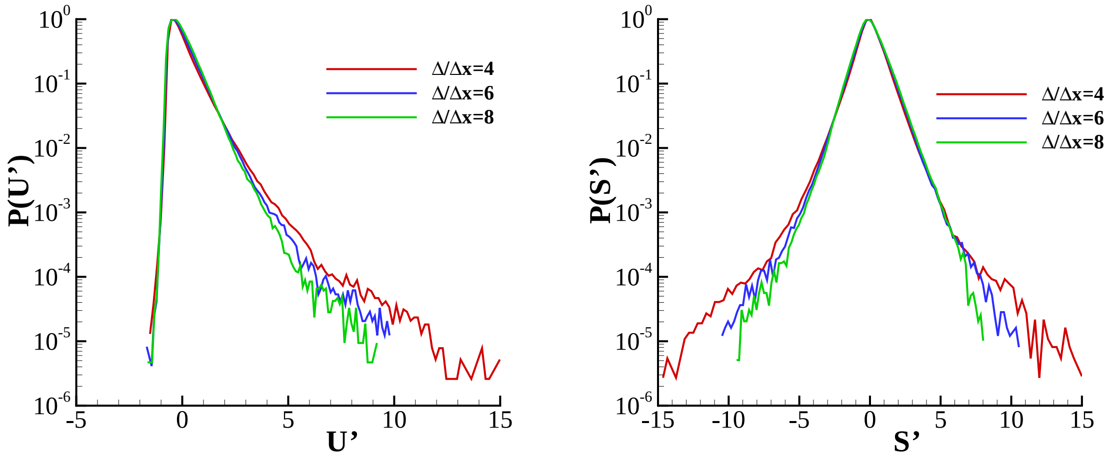

(a) D: Visc-08 - GS/SGS transfer induced by the polymer for all filters.

(b) D: Visc-08 - GS/SGS diffusion induced by the polymer for all filters.

Figure 6.12: Probability density functions for the terms U, GS/SGS transfer induced by the polymer, and S, GS/SGS diffusion induced by the polymer, comparing the three filters.

Comparing the two transfer terms, classical term Q and polymer induced term U, it is interesting to see that these terms have clearly different flatness values, having Q the highest. In

Figures 6.13(a) and 6.13(b), the intermittent nature of Q is visible, specially for extreme events. Also, Q has stronger fluctuations for the same probability. The only exception to this are the low-magnitude events, the most likely to happen. For these events, the cascade induced by the polymer is more likely to happen than the classical cascade. And this occurs for both forward and backward scatter - with the mean value added to the fluctuation. It is also curious to see, and it was somehow expected due to the analysis done before, that the differences in the PDFs of both terms are higher when the filter size is larger. The higher probability of term U comparing to term Q for low-magnitude events is more evident for the largest filter.

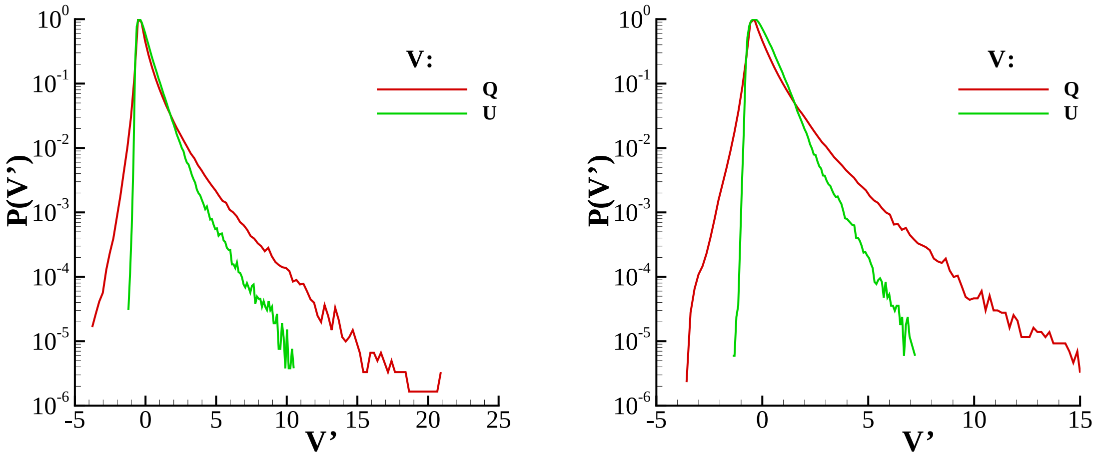

(a) B: Visc-06 - GS/SGS transfer terms Q and U with the smallest filter.

(b) B: Visc-06 - GS/SGS transfer terms Q and U with the largest filter.

Figure 6.13: Probability density functions comparing the terms Q and U with two filters.

Paying attention to the PDFs, Figures 6.14(a) and 6.14(b), of the diffusion terms, P and S, again the diffusion induced by the polymer is more likely for the low-magnitude events. From Table 6.2, it is possible to see that term P has higher variance values for larger filter sizes, and with S the opposite happens. Also, comparing different DNS, the variance values of term P increase as the solution approaches the Newtonian fluid case, and the inverse happens with term S. From Figures 6.14(a) and 6.14(b), it is possible to see that the high-magnitude events of S become more likely to happen, when comparing to P, as β increases, specially for the backward scatter.

Figure 6.15(a) shows the joint PDF of terms P and Q. From Table 6.3, it is possible to see that the correlations between these two terms are not meaningful (below 60%). However, it is important to see that the correlations are negative which means that events with P positive are related with events with S negative and vice-versa. In Figure 6.15(a) this is also clear. For the similar terms in the polymer induced cascade (see Figure 6.16(a)), the correlation coefficient is higher. The main difference of the two joint PDFs is for the backward scatter. For the polymer induced cascade, in average, 2% of the points have negative values of U which is very different from 23% in the classical cascade.

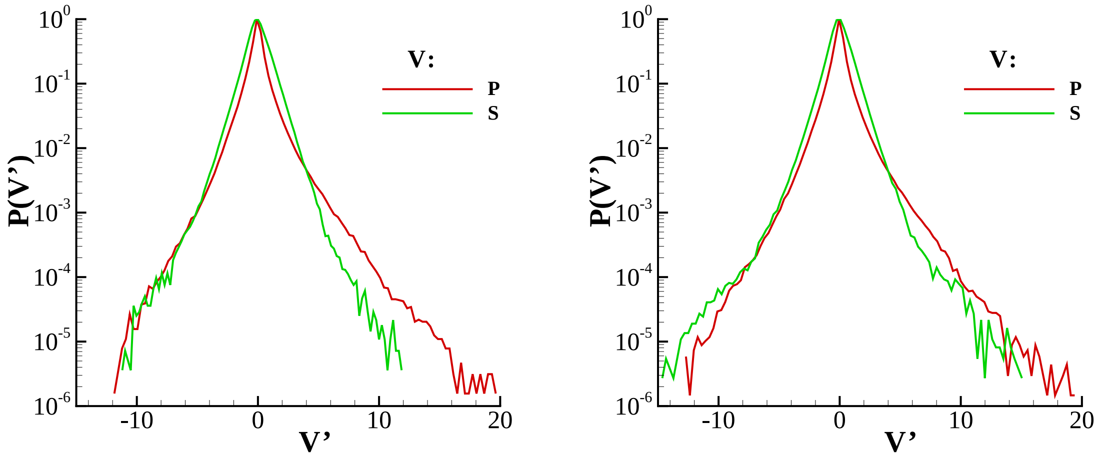

(a) B: Visc-06 - GS/SGS diffusion terms P and S with the smallest filter.

(b) D: Visc-08 - GS/SGS diffusion terms P and S with the smallest filter.

Figure 6.14: Probability density functions comparing the terms P and S with different values of β.

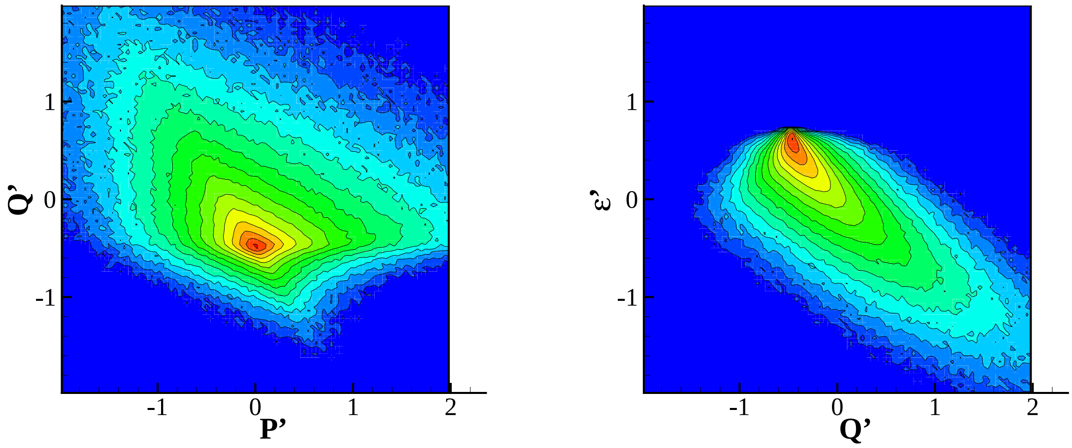

(a) B: Visc-06 - GS/SGS diffusion and transfer terms P and Q, respectively, with the smallest filter.

(b) A: Newt - GS/SGS transfer term Q and energy dissipation rate ε with the smallest filter.

Figure 6.15: Joint probability density functions regarding the terms P and Q and ε. The contour lines are spaced by a factor of 1.636, in the range 1×10^{-3} (blue) to 0.98 (red).

Figure 6.15(b) shows the joint PDF of Q and ε. Forward scatter is highly correlated with the energy dissipation rate. This is according to what was expected and it is not a new result. In the classical energy cascade, GS feed SGS and the latter dissipate part of the energy by viscosity. This is the reason for this correlation. However, it is interesting to see that for the most probable events, these two terms are not correlated. A different result is found when comparing ε with U (see Figure 6.16(b)). Again, once the polymer induces a forward cascade, the terms have a negative correlation coefficient. But, the main difference concerns the most likely events. For these events, as for the majority of them, the energy transfer from the GS to the SGS induced by the polymer is highly correlated with the energy dissipation rate.

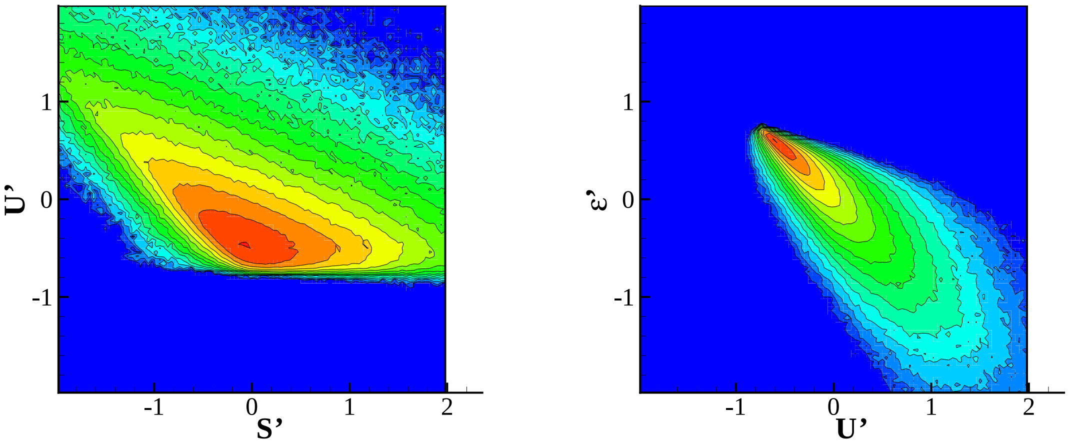

(a) B: Visc-06 - GS/SGS diffusion and transfer induced by the polymer terms S and U, respectively, with the smallest filter.

(b) B: Visc-06 - GS/SGS transfer induced by the polymer term U and energy dissipation rate ε with the smallest filter.

Figure 6.16: Joint probability density functions regarding the terms S and U and ε. The contour lines are spaced by a factor of 1.636, in the range 1×10^{-3} (blue) to 0.98 (red).

In summary, in viscoelastic computations there are two energy cascades: the classical inviscid energy cascade (the only cascade in the Newtonian fluid case) and the energy cascade induced by the presence of polymer additives. Both are mainly forward scatter, being the backward scatter present in both but more evidently in the classical cascade. As the polymer solution case approaches the Newtonian fluid case, the importance of the induced cascade vanishes. For the majority of the filters the most relevant cascade is the classical cascade (larger variance values). The exception are the small filters in which the variance values of the induced and the classical cascades are comparable.

6.2.2 SGS/Polymer interactions

In this subsection, the terms responsible for the SGS/Polymer interactions (R and T) are analysed in detail. As in the previous subsection, it is interesting to start the analysis by looking to the coherent structures (positive Qi criterion) and the relation between them and the terms of transfer and diffusion of kinetic energy between the SGS and the polymer. Figure 6.17(a) shows the term T (blue) and the positive criterion Qi (grey). Firstly, term T is always negative (for this case), that is why it is represented by only one color. This means that this term acts as a sink of SGS kinetic energy, i.e. term T represents the energy that goes from the SGS to the polymer. However, it is important to realise that this is not always true. As the filter size decreases, polymer tends to give more energy to the SGS and this is also true when β increases. For instance, for B: Visc-06 with $\Delta/\Delta x = 4$ and D: Visc-08 with $\Delta/\Delta x = 4$, there are positive values of T. Figure 6.17(a) shows no obvious correlation between SGS/Polymer transfer and coherent structures. The same conclusion was also drawn in the analysis of the two transfer terms in GS dynamics. Unlike transfer terms, diffusion terms have been showing high correlations with the vortical structures. This is again verified for the term R, as it is shown in Figure 6.17(b). In this figure, it is possible to see that the shapes of the structures are very similar and regions with high intensity of R are usually located close to the vortex cores. Also, it is possible to see that red iso-surfaces and blue iso-surfaces have similar magnitudes, as it is expected for a diffusion term. Comparing both figures, Figure 6.17(a), although intense regions of T correspond to intense regions of Qi, the first seems to have a random nature, whereas Figure 6.17(b) shows a more clear pattern and the shape of the structures are very similar.

To have an idea of the relative importance of the terms analysed so far in the SGS dynamics, Figures 6.18(a) and 6.18(b) show one line in the middle of the domain of each quantity. In Figure 6.18(a), terms U and T seem to be the symmetric of each other, which, on one hand, means that they have similar magnitudes and behaviours along the line and, on the other hand, means that the energy received by the SGS and induced by the polymer, is dissipated by the SGS to the polymer. Figure 6.18(b) shows again that the diffusion terms S and R have similar behaviours, and almost symmetric.

Table 6.4: Mean, variance, skewness and flatness values with each filter and for each term, for B: Visc-06 (top table) and D: Visc-08 (bottom table).

	$\Delta/\Delta x = 4$	$\Delta/\Delta x = 6$	$\Delta/\Delta x = 8$
T	$(-0.702, 0.318, -2.448, 14.351)$	$(-0.702, 0.217, -1.927, 9.789)$	$(-0.702, 0.152, -1.590, 7.700)$
R	$(\sim 0, 0.479, -0.117, 8.129)$	$(\sim 0, 0.271, -0.282, 6.497)$	$(\sim 0, 0.155, -0.403, 5.753)$
T	$(-0.338, 0.083, -2.963, 21.813)$	$(-0.338, 0.055, -2.264, 13.361)$	$(-0.338, 0.038, -1.867, 10.103)$
R	$(\sim 0, 0.113, -0.111, 12.341)$	$(\sim 0, 0.061, -0.314, 8.838)$	$(\sim 0, 0.034, -0.433, 7.322)$

Table 6.4 shows the mean, variance, skewness and flatness values for the terms T and R. As terms P and S, term R also has zero average. Variance values are higher for R than for T, meaning that term R plays the major role, higher intensity, in the SGS/Polymer interactions. This also happens with the other pairs, P, Q and S, U. Hence, in general, diffusion terms have more

relevance than transfer terms in the dynamics of the GS and the SGS. When comparing terms P, S and R (also based on Tables 6.2 and 6.4) term P is the most relevant whereas terms S and R have similar variance values.

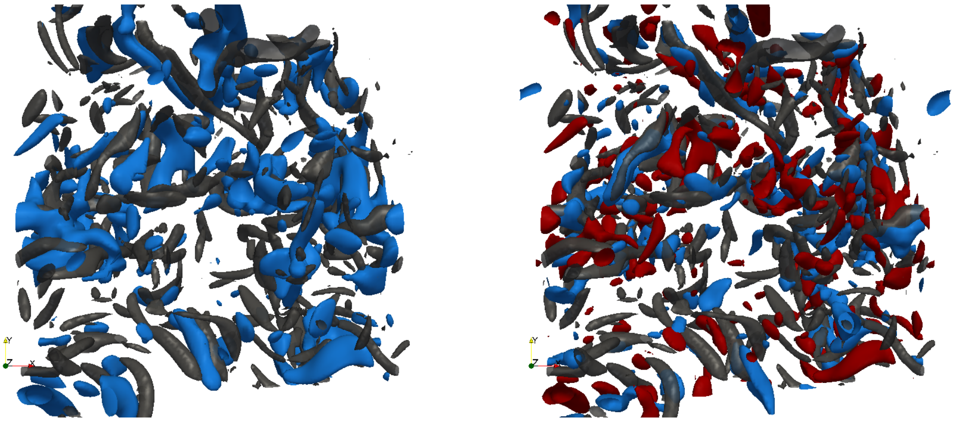

(a) B: Visc-06 - Visualizations of term T (blue) and positive Qi criterion (grey), for $\Delta/\Delta x = 6$.

(b) B: Visc-06 - Visualizations of term R (positive/red and negative/blue) and positive Qi criterion (grey), for $\Delta/\Delta x = 6$.

Figure 6.17: The threshold for term T is -1.8. The threshold of term R is the following: red corresponds to $+1.2$ and blue corresponds to -1.3. Finally, the threshold of Qi criterion is: **(a)** 80; **(b)** 80.

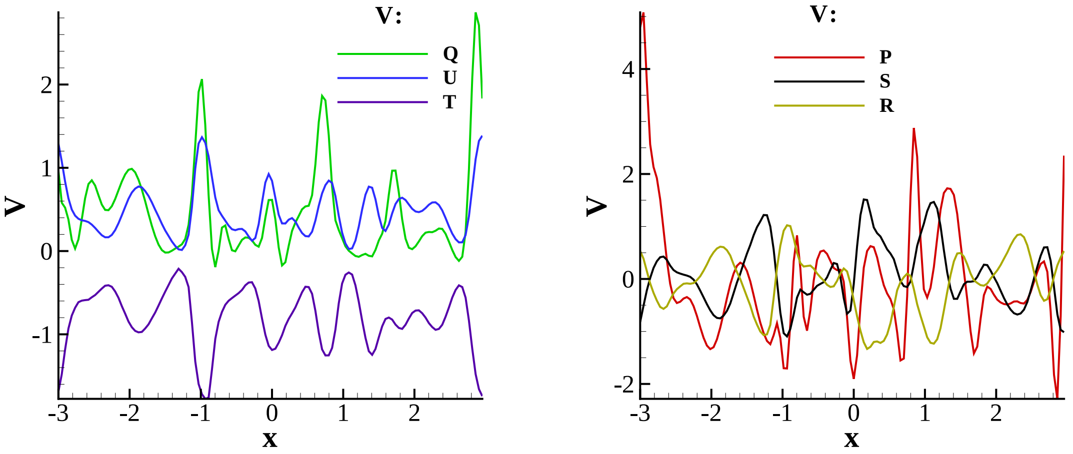

(a) B: Visc-06 - One line in the middle of the domain with values of the terms Q, U and T, for $\Delta/\Delta x = 6$.

(b) B: Visc-06 - One line in the middle of the domain with values of the terms P, S and R, for $\Delta/\Delta x = 6$.

Figure 6.18: Relevance of the terms directly related to GS/SGS and SGS/Polymer interactions, for B: Visc-06.

Figure 6.19(a) shows the PDF of term T for the different sizes of filter. The figure clearly shows, as already referred, that the energy flows predominantly to the polymer. As The PDF is based on the fluctuations, the average value of the term has to be added to get the real value. It is interesting to see that as the size of the filter decreases, stronger fluctuations can be found (which is consistent with the flatness values in Table 6.4). Also, this is consistent with the fact that for smaller sizes of filter, positive events of T are more likely to happen. Table 6.4 shows that for the same filter size, higher β means higher flatness values and stronger fluctuations (positive and negative) appear in the PDF (see Figure 6.20(a)). Hence positive events of T (kinetic energy that flows form the polymer to the SGS) are more likely to happen as the solution approaches the Newtonian fluid case. A curious fact is that the mean value is not changed by the filter size, as it is possible to see in Table 6.4 for both viscoelastic solutions.

As the solution is approaching the Newtonian fluid case the variance values decrease, i.e. the kinetic energy exchanges between SGS and Polymer, which makes all the sense because in the limit, for $\beta = 1$, the term T does not exist.

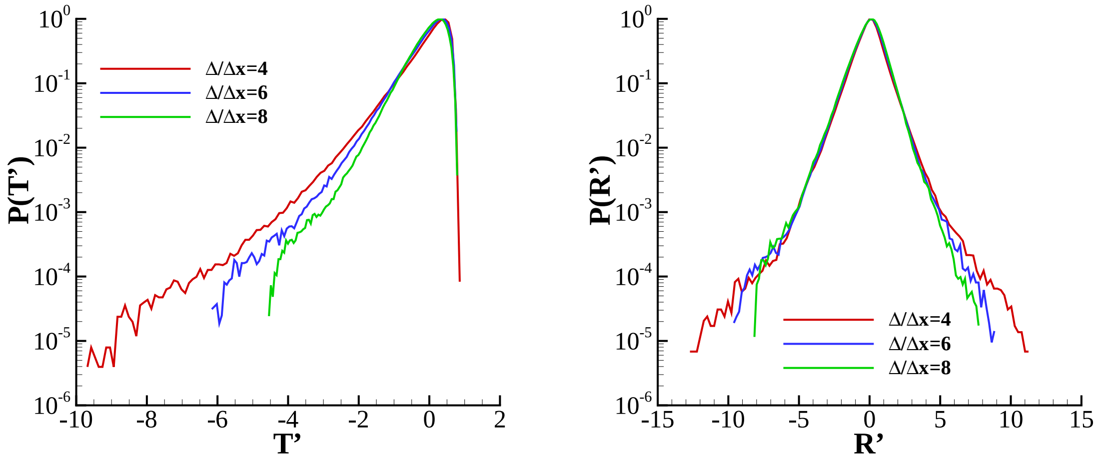

(a) B: Visc-06 - SGS/Polymer transfer, term T, for all filters.

(b) B: Visc-06 - SGS/Polymer diffusion, term R, for all filters.

Figure 6.19: Probability density functions for the terms T, SGS/Polymer transfer, and R, SGS/Polymer diffusion, comparing the three filters.

Similar conclusions can be drawn for term R, represented in Figure 6.19(b).

Figures 6.20(a) and 6.20(b) show, respectively, terms T and R for two DNS and two filters. The first figure shows that for higher values of β (comparing red and blue curves) kinetic energy transfer from the polymer to the SGS is more likely to happen, as mentioned before. The strongest fluctuations are present in the solution with the largest flatness value. It is interesting to see that values closer to the mean are more likely to happen for higher filter sizes, and this is still a consequence of the flatness values because the PDF is more flattened.

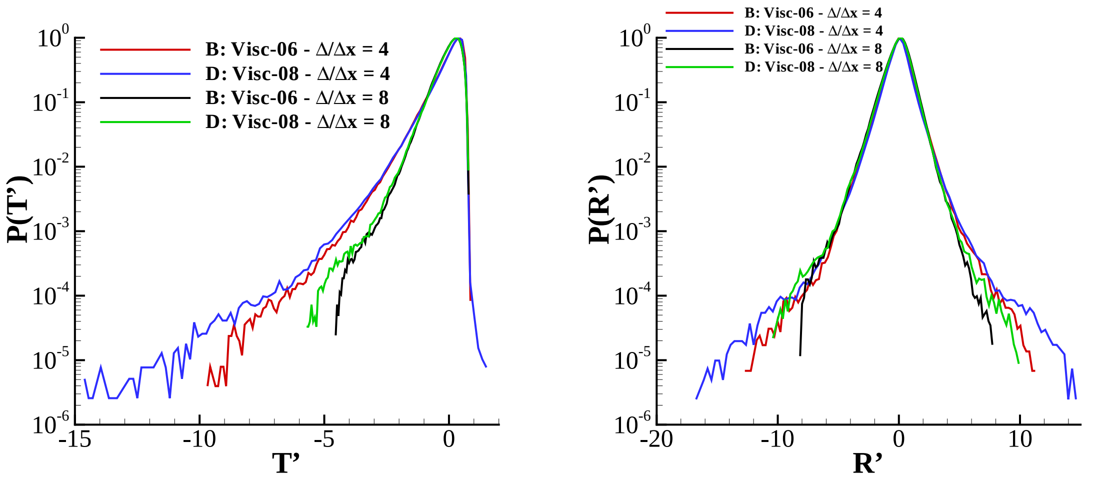

(a) SGS/Polymer transfer: Two polymer solution cases for two filters.

(b) SGS/Polymer diffusion: Two polymer solution cases for two filters.

Figure 6.20: Probability density functions for the terms T and R comparing two cases with two filters.

The same comments are applicable for term R. However, it is interesting to notice that all curves (Figure 6.20(b)) have higher negative fluctuations than positive fluctuations. This is consistent with the skewness values, in Table 6.4, that are always negative.

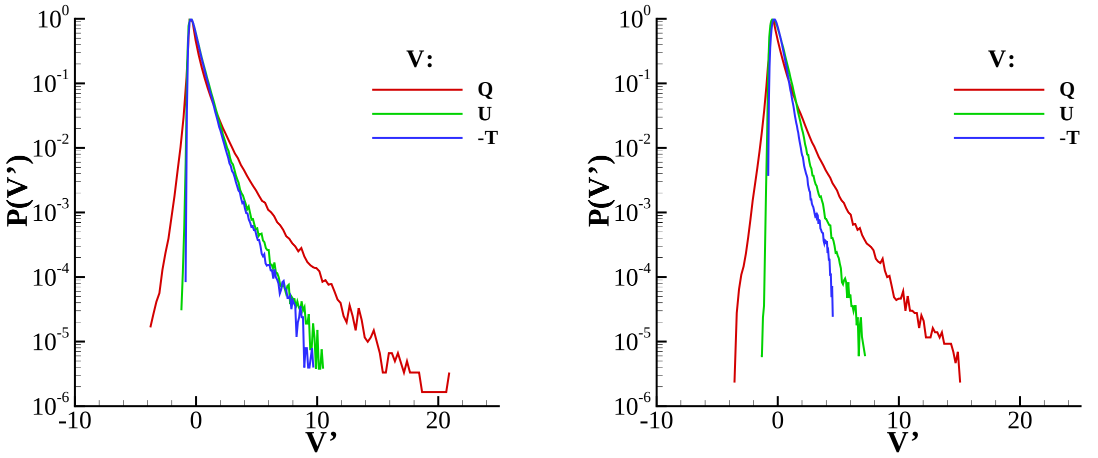

(a) B: Visc-06 - Terms Q, U and T with the smallest filter.

(b) B: Visc-06 - Terms Q, U and T with the largest filter.

Figure 6.21: Probability density functions comparing the terms Q, U and T with two filters.

Figures 6.21(a) and 6.21(b) show the three transfer terms, Q, U and T, with two filters. In order to get a more accurate comparison, the term that is presented in the figures is $-T$ instead of

T. Stronger fluctuations happen in the classical cascade. Terms U and $-T$ are almost coincident for the smallest filter. For the largest filter, this does not happen (the correlation coefficient is not so high). The correlation coefficient between these two terms is about 90% (see Table 6.5 and Figure 6.23(b)).

Figures 6.22(a) and 6.22(b) show the PDF of the diffusion terms, P, S and R, with two filters. As for Figures 6.21(a) and 6.21(b), here the term presented is $-R$ and not R. The first interesting point is that the magnitudes of the fluctuations of the three are similar. Actually, terms S and $-R$ present higher negative fluctuations with the smallest filter. Terms S and $-R$ have similar PDFs, specially for negative fluctuations, but for stronger positive events the terms behave differently, and this difference increases with the filter size.

For the low-magnitude events terms S and $-R$ have higher probability than term P has. This is more evident as the filter size decreases.

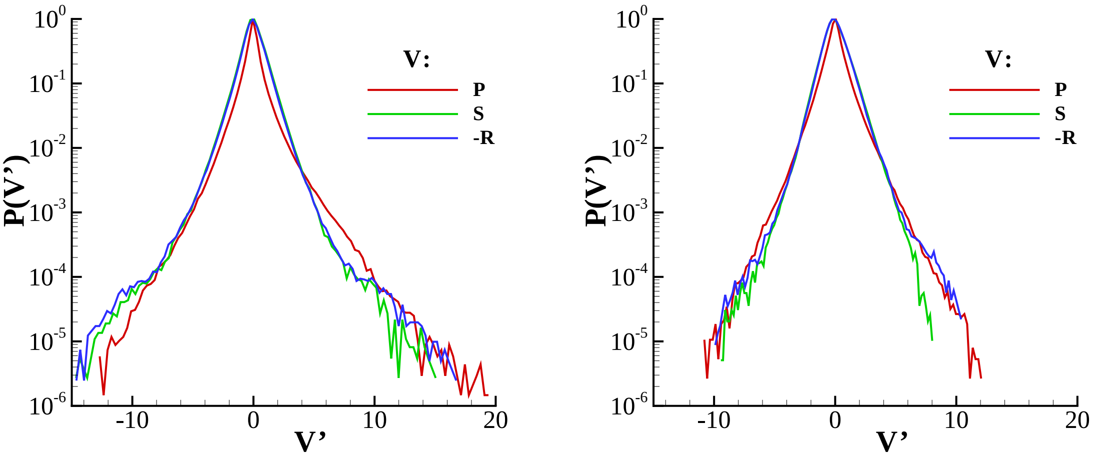

(a) D: Visc-08 - Terms P, S and R with the smallest filter.

(b) D: Visc-08 - Terms P, S and R with the largest filter.

Figure 6.22: Probability density functions comparing the terms P, S and R with two filters.

In Table 6.5, the correlation coefficients between the terms analysed in this section are computed. For the meaningful correlation coefficients, joint PDFs are shown (Figures 6.23(a), 6.23(b), 6.24(a) and 6.24(b)).

Table 6.5: Correlation coefficients for **(left)** $\Delta/\Delta x = 4$, **(middle)** $\Delta/\Delta x = 6$ and **(right)** $\Delta/\Delta x = 8$.

	B: Visc-06	D: Visc-08	B: Visc-06	D: Visc-08	B: Visc-06	D: Visc-08
(Q, T)	-0.71	-0.68	-0.67	-0.64	-0.61	-0.58
(P, T)	$+0.03$	$+0.02$	$+0.05$	$+0.04$	$+0.06$	$+0.05$
(U, T)	-0.98	-0.98	-0.94	-0.93	-0.87	-0.85
(S, T)	$+0.54$	$+0.52$	$+0.49$	$+0.46$	$+0.42$	$+0.39$
(ε, T)	$+0.86$	$+0.83$	$+0.81$	$+0.78$	$+0.74$	$+0.71$
(R, T)	-0.53	-0.52	-0.47	-0.45	-0.39	-0.35
(Q, R)	$+0.38$	$+0.36$	$+0.31$	$+0.29$	$+0.24$	$+0.22$
(P, R)	-0.18	-0.14	-0.12	-0.09	-0.09	-0.06
(U, R)	$+0.60$	$+0.59$	$+0.59$	$+0.58$	$+0.56$	$+0.55$
(S, R)	-0.98	-0.97	-0.94	-0.93	-0.89	-0.87
(ε, R)	-0.45	-0.42	-0.38	-0.34	-0.29	-0.25

It is interesting to see that there is a negative and meaningful correlation (71%) between terms Q and T (see Table 6.5 and Figure 6.23(a)). These terms are not correlated for the most likely events, but for the less frequent, there is a clear correlation between the kinetic energy that the GS gives to the SGS and the kinetic energy that the polymer receives from the latter. The correlation between these two terms decreases as β increases and this was expected to happen, once the relevance of term T decreases steeply (see Table 6.23(a)).

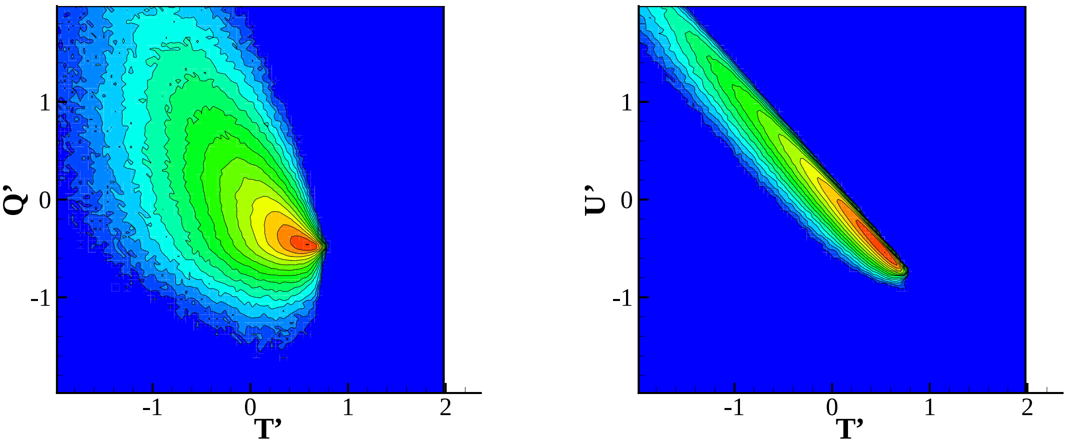

(a) B: Visc-06 - SGS/Polymer and GS/SGS transfer terms T and Q, respectively, with the smallest filter.

(b) B: Visc-06 - SGS/Polymer transfer and GS/SGS transfer induced by the polymer terms T and U, respectively, with the smallest filter.

Figure 6.23: Joint probability density functions regarding the terms T, Q and U. The contour lines are spaced by a factor of 1.636, in the range 1×10^{-3} (blue) to 0.98 (red).

In Figure 6.23(b), the joint PDF of U and T is shown. These terms have a correlation coefficient of 98% and are correlated strongly in all the events, meaning this that almost all the energy that goes from the GS to the SGS induced by the polymer, goes in the end to the polymer. The correlation coefficient decreases as the filter size increases. A possible explanation for this is that when the filter size increases, the SGS range increases as well, and this attenuates the polymer's effect, as already mentioned. Figure 6.24(b) shows a joint PDF for the terms S and R. These terms are also strongly correlated for all the events, as U and T. These correlation coefficients mean, unambiguously, that the energy cascade between GS and SGS induced by the polymer has a substantial impact on the SGS/Polymer interactions. More than that, once the coefficients are negative, it is still possible to refer that positive values of U and S are correlated with negative values of T and R, respectively, and vice-versa.

The joint PDF of T and ε, Figure 6.24(a), shows a clear correlation between the energy that goes from the SGS to the polymer and the energy that is dissipated, with a coefficient of 0.86 (Table 6.5). This makes all the sense because the energy that the SGS gives to the polymer is dissipated by the latter. The correlation coefficient decreases as the filter increases because, again, the effect of the polymer is reduced and the energy is dissipated in other ways. The terms are correlated for all the scales, i.e. for all the events, as Figure 6.24(a) shows.

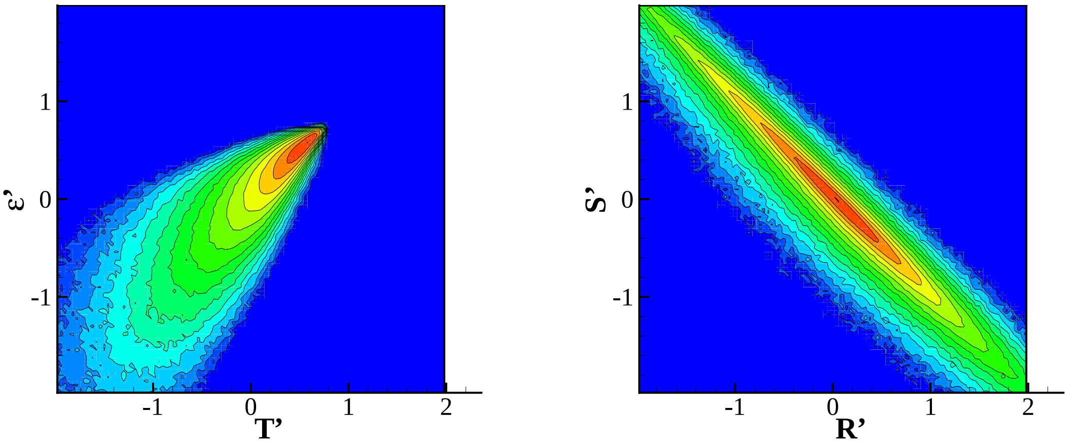

(a) B: Visc-06 - SGS/Polymer transfer, terms T, and energy dissipation rate ε with the smallest filter.

(b) B: Visc-06 - SGS/Polymer diffusion R and GS/SGS diffusion induced by the polymer S with the smallest filter.

Figure 6.24: Joint probability density functions regarding the terms T, ε and R, S. The contour lines are spaced by a factor of 1.636, in the range 1×10^{-3} (blue) to 0.98 (red).

In summary, terms T, SGS/Polymer transfer, and R, SGS/Polymer diffusion, were found to have the same relevance of terms U and S in the dynamics of the SGS. Terms T and U, GS/SGS transfer induced by the polymer, as well as terms R and S, GS/SGS diffusion induced by the polymer, behave similarly. Moreover, term T is predominantly negative but positive events gain impact for lower filters and higher β.

7

Conclusions

Contents

A three dimensional pseudo-spectral code for DNS with polymer additives was developed and the results were first compared to one analytical solution (provided by the Couette flow, see ”2D code: Verification” in ”Verification and code to code comparison”) and then compared with the results obtained in Cai et al. [70] in DHIT (see ”3D code: Code to code comparison”). With the code to code comparison, the first meaningful results were obtained. In addition, the GS and SGS kinetic energy transport equations were derived for the polymer solution case. Four new terms appeared and were analysed minutely in ”Energy cascade analysis”.

7.1 General results for DHIT with polymer additives

The temporal evolutions of Taylor microscale, energy dissipation rate, turbulent kinetic energy, conformation tensor trace and enstrophy were computed. Moreover, the energy spectra with and without polymer additives were analysed.

Regarding the Taylor microscale, the difference between Newtonian fluid and polymer solution cases is obvious in the EDP. Taylor microscale is larger with polymer additives which indicates that the decay of small-scales structures is faster. The energy dissipation rate is smaller for the polymer solution case due to the energy-absorption effect of the polymers, which proves the drag-reduction phenomenon. For the turbulent kinetic energy, there are unambiguously two different regions. In the first region, the decay of ξ for the polymer solutions cases is faster than for the Newtonian case, because, due to the development of small-scale structures, polymers absorb part of the turbulent kinetic energy. In the second region, the opposite is observed, because polymers release part of the elastic energy and absorb less energy from the flow structures. The evolution of the conformation tensor trace shows, in an initial phase, that polymers are stretched because they absorb part of the turbulent kinetic energy. As polymers release the elastic energy stored previously, their mean elongation decreases and polymers tend to the equilibrium state, at which point the system reverts back to a Newtonian fluid. The enstrophy increases, in EPP, and vortex structures are stretched and decreases, in EDP, indicating the suppression and dissipation of the vortex structures. With polymer additives, the enstrophy is remarkably weaker than for the Newtonian fluid.

In addition to this, the energy spectra were analysed. In the EPP, energy is transferred from the large and intermediate scales to the small scales for both Newtonian fluid and polymer solution cases. In the EDP, all scales lose energy, and polymers absorb energy from the large scales and release energy to the small scales (this was also observed when analysing the energy cascade).

Besides, there is a marked inhibition of small-scale structures in polymer solutions cases. In the EDP, the decrease of tube-like vortex is faster in viscoelastic computations due to the suppression of the smallest resolved scales of motion by polymer additives.

7.2 Energy cascade analysis in a viscoelastic turbulent flow in DHIT

In the GS and SGS kinetic energy transport equations there are four new terms, responsible for the interactions between GS and SGS induced by the polymer and between SGS and polymer.

The two new terms, in the GS kinetic energy transport equation, represent the diffusion and transfer of energy between the GS and the SGS, caused by the polymer. Thus, in viscoelastic turbulence there are two energy cascades: the classical inviscid energy cascade (which is the classical cascade in the Newtonian fluid case) and the energy cascade induced by the presence of polymer additives. Both are dominated by forward scatter, but backward scatter is present in both but more evidently in the classical cascade. As the polymer solution case approaches the Newtonian fluid case, the importance of the induced viscoelastic cascade vanishes. For the majority of the filters the most relevant cascade is the classical cascade (larger variance values). The exception are the small filters in which the variance values of the induced and the classical cascades are comparable.

In the SGS dynamics, there are four new terms. Two of them are the symmetric of the terms present in the GS kinetic energy equation, because these two terms represent the interactions between GS and SGS, and thus they have to appear in both equations. The other two terms describe the interactions between the SGS and the polymer (diffusion and transfer). These terms were found to have the same relevance as the terms responsible for the energy cascade induced by the polymer, in the dynamics of the SGS. The GS/SGS transfer induced by the polymer and the SGS/Polymer transfer have similar behaviours, as well as for the respective diffusion terms. Moreover, the term that quantifies the energy transfer between the SGS and the polymer is predominantly negative, i.e. the energy goes mainly from the SGS to the polymer and not in the opposite way. However, positive events gain impact, kinetic energy transfer from the polymer to the SGS, for lower filters and higher values of β.

7.3 Future work

In order to continue the work done within this thesis, several interesting topics can be addressed:

1. to develop SGS closures for viscoelastic turbulence based on the present results.
2. to do the same study as presented here, but for finer meshes. As mentioned, polymer has the highest impact in the smallest scales - the energy spectra clearly shows that. By carrying out DNS, for DHIT, with finer meshes, it would be possible to catch smaller scales. The terms that represent the interactions between SGS and polymer are the most interesting to analyse.

3. to analyse with more detail the interactions between GS, SGS and polymer. For this, the kinetic energy transport equations for the GS and the SGS were derived (Appendix A). The filtering was done in the conformation tensor and not in the polymer stress, as before, meaning this that more detailed equations are derived. A better understanding of the interactions between GS, SGS and polymer can be achieved analysing the statistics of each term of interest.

References

[1] B.A. Toms. Some observations on the flow of linear polymer solutions through straight tubes at large Reynolds numbers. P. of the 1st International Congress on Rheology, 2:135–141, 1949.

[2] P. Diamond, J. Harvey, J. Katz, D. Nelson, and P. Steinhardt. Drag reduction by polymer additives. Technical report, DTIC Document, 1992.

[3] C.M. White and M.G. Mungal. Mechanics and prediction of turbulent drag reduction with polymer additives. Annu. Rev. Fluid Mech., 40:235–256, 2008.

[4] C.D. Dimitropoulos, R. Sureshkumar, and A.N. Beris. Direct numerical simulation of viscoelastic turbulent channel flow exhibiting drag reduction: effect of the variation of rheological parameters. J. Non-Newt. Fluid Mech., 79(2):433–468, 1998.

[5] I. Sher and G. Hetsroni. A mechanistic model of turbulent drag reduction by additives. Chemical Engineering Science, 63(7):1771–1778, 2008.

[6] P.S. Virk, E.W. Merrill, H.S. Mickley, K.A. Smith, and E.L. Mollo-Christensen. The Toms phenomenon: turbulent pipe flow of dilute polymer solutions. J. Fluid Mech., 30(02):305–328, 1967.

[7] A. Gyr and H.W. Bewersdorff. Drag Reduction of Turbulent Flows by Additives. Fluid Mechanics and Its Applications. Springer, 1995. ISBN 9780792334859. URL `http://books.google.pt/books?id=GLYSM1Cm7p8C`.

[8] P.S. Virk. Drag reduction fundamentals. American Institute of Chemical Engineers, Journ of, 21(4), 1975.

[9] V. Brederode. Fundamentos de Aerodinâmica Incompressível. 1997.

[10] J.L. Lumley. Drag reduction by additives. Annu. Rev. Fluid Mech., 1(1):367–384, 1969.

[11] J.L. Lumley. Drag reduction in two phase and polymer flows. Phys. Fluids, 20:S64, 1977.

[12] R. Sureshkumar, A.N. Beris, and R.A. Handler. Direct numerical simulation of the turbulent channel flow of a polymer solution. Phys. Fluids, 9(3):743–755, 1997.

[13] T. Min, H. Choi, and J.Y. Yoo. Maximum drag reduction in a turbulent channel flow by polymer additives. J. Fluid Mech., 492(1):91–100, 2003.

[14] B.H. Zimm. Dynamics of polymer molecules in dilute solution: viscoelasticity, flow birefringence and dielectric loss. The Journal of Chemical Physics, 24:269, 1956.

[15] P.G. De Gennes. Introduction to polymer dynamics. Cambridge University Press, 1990.

[16] P. Pincus. Excluded volume effects and stretched polymer chains. Macromolecules, 9(3): 386–388, 1976.

[17] K.R. Sreenivasan and C.M. White. The onset of drag reduction by dilute polymer additives, and the maximum drag reduction asymptote. J. Fluid Mech., 409:149–164, 2000.

[18] M.T. Landahl. Dynamics of boundary layer turbulence and the mechanism of drag reduction. Phys. Fluids, 20:S55, 1977.

[19] V.S. L'vov, A. Pomyalov, I. Procaccia, and V. Tiberkevich. Drag reduction by polymers in wall bounded turbulence. Phys. Review Lett., 92(24):244503, 2004.

[20] E. De Angelis, C.M. Casciola, V.S. L'vov, A. Pomyalov, I. Procaccia, and V. Tiberkevich. Drag reduction by a linear viscosity profile. Physical Review E, 70(5):055301, 2004.

[21] R. Benzi, E. De Angelis, V.S. L'vov, I. Procaccia, and V. Tiberkevich. Maximum drag reduction asymptotes and the cross-over to the Newtonian plug. J. Fluid Mech., 551(1):185, 2006.

[22] R.J. Hansen. The reduced drag of polymer solutions in turbulent and transient laminar shear flows. J. Fluids Eng., 95:23, 1973.

[23] G. Ryskin. Turbulent drag reduction by polymers: a quantitative theory. Phys. Review Lett., 59(18):2059–2062, 1987.

[24] J.M.J. Den Toonder, M.A. Hulsen, G.D.C. Kuiken, and F.T.M. Nieuwstadt. Drag reduction by polymer additives in a turbulent pipe flow: numerical and laboratory experiments. J. Fluid Mech., 337(1):193–231, 1997.

[25] C.D. Dimitropoulos, Y. Dubief, E.S.G. Shaqfeh, P. Moin, and S.K. Lele. Direct numerical simulation of polymer-induced drag reduction in turbulent boundary layer flow. Phys. Fluids, 17:011705, 2005.

[26] C.D. Dimitropoulos, R. Sureshkumar, A.N. Beris, and R.A. Handler. Budgets of Reynolds stress, kinetic energy and streamwise entropy in viscoelastic turbulent channel flow. Phys. Fluids, 13:1016, 2001.

[27] M. Fichman and G. Hetsroni. Electrokinetic aspects of turbulent drag reduction in surfactant solutions. Phys. Fluids, 16:4346, 2004.

[28] T. Vaithianathan, A. Robert, J.G. Brasseur, and L.R. Collins. An improved algorithm for simulating three-dimensional, viscoelastic turbulence. J. Non-Newt. Fluid Mech., 140(1):3–22, 2006.

[29] F. Dupret and J.M. Marchal. Loss of evolution in the flow of viscoelastic fluids. J. Non-Newt. Fluid Mech., 20:143–171, 1986.

[30] R. Sureshkumar and A.N. Beris. Effect of artificial stress diffusivity on the stability of numerical calculations and the flow dynamics of time-dependent viscoelastic flows. J. Non-Newt. Fluid Mech., 60(1):53–80, 1995.

[31] T. Vaithianathan and L.R. Collins. Numerical approach to simulating turbulent flow of a viscoelastic polymer solution. J. Comp. Phys., 187(1):1–21, 2003.

[32] A.N. Beris and B.J. Edwards. Thermodynamics of Flowing Systems: With Internal Structure. Oxford Engineering Science Series. Oxford University Press, 1994. ISBN 9780195076943. URL `http://www.google.pt/books?id=dqxFUy7_vhsC`.

[33] S.K. Lele. Compact finite difference schemes with spectral-like resolution. J. Comp. Phys., 103(1):16–42, 1992.

[34] C.B. Laney. Computational Gasdynamics. Cambridge University Press, 1998. ISBN 9780521625586. URL `http://books.google.pt/books?id=r-bYw-JjKGAC`.

[35] A.W. El-Kareh and L. Gary Leal. Existence of solutions for all Deborah numbers for a non-Newtonian model modified to include diffusion. J. Non-Newt. Fluid Mech., 33(3):257–287, 1989.

[36] D. Gottlieb and J.S. Hesthaven. Spectral methods for hyperbolic problems. J. Comput. Appl. Math., 128(1):83–131, 2001.

[37] B. Van Leer. Towards the ultimate conservative difference scheme. V. A second-order sequel to Godunov's method. J. Comp. Phys., 32(1):101–136, 1979.

[38] H. Nessyahu and E. Tadmor. Non-oscillatory central differencing for hyperbolic conservation laws. J. Comp. Phys., 87(2):408–463, 1990.

[39] A. Kurganov and E. Tadmor. New high-resolution central schemes for nonlinear conservation laws and convection–diffusion equations. J. Comp. Phys., 160(1):241–282, 2000.

[40] A.G. Fabula. An experimental study of grid turbulence in dilute high-polymer solutions. Technical report, DTIC Document, 1966.

[41] W.D. McComb, J. Allan, and C.A. Greated. Effect of polymer additives on the small-scale structure of grid-generated turbulence. Phys. Fluids, 20:873, 1977.

[42] C.A. Friehe and W.H. Schwarz. Grid-generated turbulence in dilute polymer solutions. J. Fluid Mech., 44(173-193):1, 1970.

[43] E. van Doorn, C.M. White, and K.R. Sreenivasan. The decay of grid turbulence in polymer and surfactant solutions. Phys. Fluids, 11:2387, 1999.

[44] B.J.S. Barnard and R.H.J. Sellin. Grid turbulence in dilute polymer solutions. 1969.

[45] A.M. Crawford, N. Mordant, H. Xu, and E. Bodenschatz. Fluid acceleration in the bulk of turbulent dilute polymer solutions. New Journal of Physics, 10(12):123015, 2008.

[46] N.T. Ouellette, H. Xu, and E. Bodenschatz. Bulk turbulence in dilute polymer solutions. J. Fluid Mech., 629:375, 2009.

[47] N. Tabor and P.G. De Gennes. A cascade theory of drag reduction. Europhys. Lett., 2(7): 519–522, 1986.

[48] P.G. De Gennes. Towards a scaling theory of drag reduction. Physica A: Statistical Mechanics and its Applications, 140(1):9–25, 1986.

[49] J.L. Lumley. Drag reduction in turbulent flow by polymer additives. Journal of Polymer Science, Part D: Macromol Rev, 7, 1973.

[50] E. De Angelis, C.M. Casciola, and R. Piva. DNS of wall turbulence: dilute polymers and self-sustaining mechanisms. Computers and Fluids, 31(4):495–507, 2002.

[51] B. Yu and Y. Kawaguchi. Direct numerical simulation of viscoelastic drag-reducing flow: a faithful finite difference method. J. Non-Newt. Fluid Mech., 116(2):431–466, 2004.

[52] E. De Angelis, C.M. Casciola, V.S. L'vov, R. Piva, and I. Procaccia. Drag reduction by polymers in turbulent channel flows: Energy redistribution between invariant empirical modes. Physical Review E, 67(5):056312, 2003.

[53] Y. Dubief, C.M. White, V.E. Terrapon, E.S.G. Shaqfeh, P. Moin, and S.K. Lele. On the coherent drag-reducing and turbulence-enhancing behaviour of polymers in wall flows. J. Fluid Mech., 514:271–280, 2004.

[54] P.K. Ptasinski, B.J. Boersma, F.T.M. Nieuwstadt, M.A. Hulsen, B. Van den Brule, and J.C.R. Hunt. Turbulent channel flow near maximum drag reduction: simulations, experiments and mechanisms. J. Fluid Mech., 490(1):251–291, 2003.

[55] S. Sibilla and A. Baron. Polymer stress statistics in the near-wall turbulent flow of a drag-reducing solution. Phys. Fluids, 14:1123, 2002.

[56] R.B. Bird, C.F. Curtiss, R.C. Armstrong, and O. Hassager. Dynamics of polymeric liquids. Vol. 2: Kinetic theory. Wiley-Interscience, 1987,, page 450, 1987.

[57] P.M.R. Resende. Turbulence models for viscoelastic fluids. PhD thesis, Faculdade de Engenharia da Universidade do Porto, 2010.

[58] M. Somasi, B. Khomami, N.J. Woo, J.S. Hur, and E.S.G. Shaqfeh. Brownian dynamics simulations of bead-rod and bead-spring chains: numerical algorithms and coarse-graining issues. J. Non-Newt. Fluid Mech., 108(1):227–255, 2002.

[59] A.P.G. Van Heel, M.A. Hulsen, and B. Van Den Brule. On the selection of parameters in the FENE-P model. J. Non-Newt. Fluid Mech., 75(2):253–271, 1998.

[60] D. Vincenzi, S. Jin, E. Bodenschatz, and L.R. Collins. Stretching of polymers in isotropic turbulence: a statistical closure. Phys. Review Lett., 98(2):24503, 2007.

[61] L.E. Wedgewood, D.N. Ostrov, and R.B. Bird. A finitely extensible bead-spring chain model for dilute polymer solutions. J. Non-Newt. Fluid Mech., 40(1):119–139, 1991.

[62] Q. Zhou and R. Akhavan. A comparison of FENE and FENE-P dumbbell and chain models in turbulent flow. J. Non-Newt. Fluid Mech., 109(2):115–155, 2003.

[63] V.N. Kalashnikov. Shear-rate dependent viscosity of dilute polymer solutions. Journal of Rheology, 38(5):1385–1403, 1994.

[64] J. Azaiez and G.M. Homsy. Numerical simulation of non-Newtonian free shear flows at high Reynolds numbers. J. Non-Newt. Fluid Mech., 52(3):333–374, 1994.

[65] T. Min, J.Y. Yoo, H. Choi, and D.D. Joseph. Drag reduction by polymer additives in a turbulent channel flow. J. Fluid Mech., 486:213–238, 2003.

[66] M.A. Hulsen. A sufficient condition for a positive definite configuration tensor in differential models. J. Non-Newt. Fluid Mech., 38(1):93–100, 1990.

[67] C.F. da Silva. The role of coherent structures in the control and interscale interactions of round, plane and coaxial jets. PhD thesis, Institut National Polytechnique de Grenoble, 2001.

[68] J.H. Ferziger and M. Perić. Computational methods for fluid dynamics, volume 2. Springer Berlin etc, 1999.

[69] J.H. Williamson. Low-storage runge-kutta schemes. J. Comp. Phys., 35(1):48–56, 1980.

[70] W.-H. Cai, F.-C. Li, and H.-N. Zhang. DNS study of decaying homogeneous isotropic turbulence with polymer additives. J. Fluid Mech., 665:334–356, 2010.

[71] F.T. Pinho, C.F. Li, B.A. Younis, and R. Sureshkumar. A low Reynolds number turbulence closure for viscoelastic fluids. J. Non-Newt. Fluid Mech., 154(2):89–108, 2008.

[72] A.P. Mósca, R.D.B. Marques, C.B. da Silva, and F. Pinho. Estudo da cascata de energia em escoamentos turbulentos viscoelásticos. page 169. LNEC, IV Conferência Nacional em Mecânica dos Fluídos, Termodinâmica e Energia, 2012.

[73] E. De Angelis, C.M. Casciola, R. Benzi, and R. Piva. Homogeneous isotropic turbulence in dilute polymers. J. Fluid Mech., 531:1–10, 2005.

[74] S. Jin. Numerical simulations of a dilute polymer solution in isotropic turbulence. PhD thesis, Cornell University, 2007.

[75] S. Berti, A. Bistagnino, G. Boffetta, A. Celani, and S. Musacchio. Small-scale statistics of viscoelastic turbulence. Europhys. Lett., 76(1):63–69, 2006.

[76] P. Perlekar, D. Mitra, and R. Pandit. Manifestations of drag reduction by polymer additives in decaying, homogeneous, isotropic turbulence. Phys. Review Lett., 97(26):264501, 2006.

[77] C. Kalelkar, R. Govindarajan, and R. Pandit. Drag reduction by polymer additives in decaying turbulence. Physical Review E, 72(1):017301, 2005.

[78] R.H. Kraichnan. Decay of isotropic turbulence in the direct-interaction approximation. Phys. Fluids, 7:1030, 1964.

[79] E. De Angelis, C.M. Casciola, and R. Piva. Energy spectra in viscoelastic turbulence. Physica D: Nonlinear Phenomena, 241(3):297–303, 2012.

[80] S.B. Pope. Turbulent Flows. Cambridge University Press, 2000. ISBN 9780521598866. URL `http://books.google.pt/books?id=HZsTw9SMx-0C`.

[81] C.M. Casciola and E. De Angelis. Energy transfer in turbulent polymer solutions. J. Fluid Mech., 581:419, 2007.

[82] U. Frisch. Turbulence: the legacy of AN Kolmogorov. Cambridge University Press, 1995.

[83] U. Piomelli, W.H. Cabot, P. Moin, and S. Lee. Subgrid-scale backscatter in turbulent and transitional flows. Physics of Fluids A: Fluid Dynamics, 3:1766, 1991.

[84] U. Piomelli and J.R. Chasnov. Large-eddy simulations- theory and applications. Turbulence and transition modelling, pages 269–336, 1996.

[85] C.B. da Silva and O. Métais. On the influence of coherent structures upon interscale interactions in turbulent plane jets. J. Fluid Mech., 473(1):103–145, 2002.

A

Equations for the microscopic energy cascade analysis in a viscoelastic turbulent flow

The Navier-Stokes equations, in a viscoelastic turbulent flow, are given by:

$$\frac{\partial u_i}{\partial x_i} = 0, \tag{A.1}$$

$$\frac{\partial u_i}{\partial t} + u_j \frac{\partial u_i}{\partial x_j} = -\frac{1}{\rho}\frac{\partial p}{\partial x_i} + \nu^{[s]} \frac{\partial}{\partial x_j}\left(\frac{\partial u_i}{\partial x_j} + \frac{\partial u_j}{\partial x_i}\right) + \frac{1}{\rho}\frac{\partial T_{ij}^{[p]}}{\partial x_j} \tag{A.2}$$

However, $T_{ij}^{[p]}$ is given as follows:

$$T_{ij}^{[p]} = \frac{\mu^{[p]}}{\tau_p}(f(r)C_{ij} - \delta_{ij}), \tag{A.3}$$

and the transport equation for the conformation tensor is:

$$\frac{\partial C_{ij}}{\partial t} + u_k \frac{\partial C_{ij}}{\partial x_k} = C_{jk}\frac{\partial u_i}{\partial x_k} + C_{ik}\frac{\partial u_j}{\partial x_k} - \frac{f(r)C_{ij} - \delta_{ij}}{\tau_p} \tag{A.4}$$

Hence, equation (A.2) can be rewritten in the following form:

$$\begin{split}\frac{\partial u_i}{\partial t} + u_j \frac{\partial u_i}{\partial x_j} + \nu^{[p]} \frac{\partial}{\partial x_j}\left(\frac{\partial C_{ij}}{\partial t} + u_k \frac{\partial C_{ij}}{\partial x_k}\right) = -\frac{1}{\rho}\frac{\partial p}{\partial x_i} + \nu^{[s]} \frac{\partial}{\partial x_j}\left(\frac{\partial u_i}{\partial x_j} + \frac{\partial u_j}{\partial x_i}\right) + \\ + \nu^{[p]} \frac{\partial}{\partial x_j}\left(C_{jk}\frac{\partial u_i}{\partial x_k} + C_{ik}\frac{\partial u_j}{\partial x_k}\right)\end{split} \tag{A.5}$$

In order to obtain the equations for the kinetic energy transport for the GS and for the SGS, a filtering process is necessary. As it was already referred, the following decomposition must be done:

$$u_i = \overline{u_i} + {u_i}' \tag{A.6}$$

$$p = \overline{p} + p' \tag{A.7}$$

$$C_{ij} = \overline{C_{ij}} + {C_{ij}}' \tag{A.8}$$

Thus, the resulting filtered Navier-Stokes equations are:

$$\frac{\partial \overline{u_i}}{\partial x_i} = 0, \tag{A.9}$$

$$\begin{split}\frac{\partial \overline{u_i}}{\partial t} + \overline{u_j} \frac{\partial \overline{u_i}}{\partial x_j} + \nu^{[p]} \frac{\partial}{\partial x_j}\left(\frac{\partial \overline{C_{ij}}}{\partial t} + \overline{u_k} \frac{\partial \overline{C_{ij}}}{\partial x_k}\right) = -\frac{1}{\rho}\frac{\partial \overline{p}}{\partial x_i} + \nu^{[s]} \frac{\partial}{\partial x_j}\left(\frac{\partial \overline{u_i}}{\partial x_j} + \frac{\partial \overline{u_j}}{\partial x_i}\right) - \frac{\partial \tau_{ij}}{\partial x_j} + \\ + \nu^{[p]} \frac{\partial}{\partial x_j}\left(\frac{\partial \overline{C_{jk}} \cdot \overline{u_i}}{\partial x_k} + \frac{\partial \overline{C_{ik}}\overline{u_j}}{\partial x_k}\right) - \nu^{[p]}\left(\overline{u_i \frac{\partial C_{jk}}{\partial x_k}} + \overline{u_j \frac{\partial C_{ik}}{\partial x_k}}\right) - \\ - \nu^{[p]} \frac{\partial}{\partial x_j}\left(\frac{\partial}{\partial x_k}\left(\tau_{ijk}^{[p]} - \tau_{jki}^{[p]} - \tau_{ikj}^{[p]}\right)\right)\end{split} \tag{A.10}$$

In equation (A.10), τ_{ij} is the unknown subgrid-stress tensor and is given by:

$$\tau_{ij} = \overline{u_i u_j} - \overline{u_i} \cdot \overline{u_j}, \tag{A.11}$$

and $\tau_{ijk}^{[p]}$ is the analogous tensor for the polymer, hereafter called subgrid-stress polymer tensor, and is the following:

$$\tau_{ijk}^{[p]} = \overline{C_{ij} u_k} - \overline{C_{ij}} \cdot \overline{u_k} \tag{A.12}$$

Hence, multiplying equation (A.10) by $\overline{u_i}$, the transport equation for the GS kinetic energy is obtained:

$$\begin{aligned}
&\underbrace{\frac{\partial \overline{u_i} \cdot \overline{u_i}}{\partial t}}_{N.I} + \underbrace{\frac{\partial \overline{u_i} \cdot \overline{u_i} \cdot \overline{u_j}}{\partial x_j}}_{N.II} + \underbrace{2\nu^{[p]} \frac{\partial}{\partial x_j} \left(\frac{\partial \overline{C_{ij}} \cdot \overline{u_i}}{\partial t} \right)}_{V.I} \underbrace{-2\nu^{[p]} \left(\frac{\partial}{\partial x_j} \left(\overline{C_{ij}} \frac{\partial \overline{u_i}}{\partial t} \right) + \frac{\partial \overline{u_i}}{\partial x_j} \frac{\partial \overline{C_{ij}}}{\partial t} \right)}_{V.II} + \\
&+ \underbrace{2\nu^{[p]} \frac{\partial}{\partial x_j} \left(\frac{\partial \overline{C_{ij}} \cdot \overline{u_i} \cdot \overline{u_k}}{\partial x_k} \right)}_{V.III} = \underbrace{-\frac{2}{\rho} \frac{\partial \overline{p} \cdot \overline{u_i}}{\partial x_i}}_{N.III} + \underbrace{\nu^{[s]} \frac{\partial}{\partial x_j} \left(\frac{\partial \overline{u_i} \cdot \overline{u_i}}{\partial x_j} \right)}_{N.IV} \underbrace{-2\nu^{[s]} \frac{\partial \overline{u_i}}{\partial x_j} \frac{\partial \overline{u_i}}{\partial x_j}}_{N.V} \underbrace{-2 \frac{\partial \tau_{ij} \overline{u_i}}{\partial x_j}}_{N.VI} + \\
&+ \underbrace{2\tau_{ij} \overline{S_{ij}}}_{N.VII} + \underbrace{2\nu^{[p]} \frac{\partial}{\partial x_j} \left(\frac{\partial \overline{C_{ij}} \cdot \overline{u_i} \cdot \overline{u_i}}{\partial x_k} + \frac{\partial \overline{C_{ik}} \cdot \overline{u_j} \cdot \overline{u_i}}{\partial x_k} \right)}_{V.IV} \underbrace{-2\nu^{[p]} \frac{\partial \overline{u_i}}{\partial x_j} \left(\frac{\partial \overline{C_{jk}} \cdot \overline{u_i}}{\partial x_k} + \frac{\partial \overline{C_{ik}} \cdot \overline{u_j}}{\partial x_k} - \frac{\partial \overline{C_{ij}} \cdot \overline{u_k}}{\partial x_k} \right)}_{V.V} \\
&\underbrace{-2\nu^{[p]} \frac{\partial}{\partial x_j} \left(\frac{\partial}{\partial x_k} \left(\overline{u_i} \left(\tau_{ijk}^{[p]} - \tau_{jki}^{[p]} - \tau_{ikj}^{[p]} \right) \right) \right)}_{V.VI} + \underbrace{2\nu^{[p]} \frac{\partial}{\partial x_j} \left(\frac{\partial \overline{u_i}}{\partial x_k} \left(\tau_{ijk}^{[p]} - \tau_{jki}^{[p]} \right) - \tau_{ikj}^{[p]} \overline{S_{ik}} \right)}_{V.VII} + \\
&+ \underbrace{2\nu^{[p]} \frac{\partial \overline{u_i}}{\partial x_j} \frac{\partial}{\partial x_k} \left(\tau_{ijk}^{[p]} - \tau_{jki}^{[p]} - \tau_{ikj}^{[p]} \right)}_{V.VIII} \underbrace{-2\nu^{[p]} \frac{\partial}{\partial x_j} \left(\frac{\partial \overline{u_i}}{\partial x_k} \left(\overline{C_j k} \cdot \overline{u_i} + \overline{C_i k} \cdot \overline{u_j} - \overline{C_i j} \cdot \overline{u_k} \right) \right)}_{V.IX} \\
&\underbrace{-2\nu^{[p]} \frac{\partial}{\partial x_j} \left(\overline{u_i} \left(\overline{u_i \frac{\partial C_{jk}}{\partial x_k} + u_j \frac{\partial C_{ik}}{\partial x_k}} \right) \right)}_{V.X} + \underbrace{2\nu^{[p]} \frac{\partial \overline{u_i}}{\partial x_j} \left(\overline{u_i \frac{\partial C_{jk}}{\partial x_k}} + \overline{u_j \frac{\partial C_{ik}}{\partial x_k}} \right)}_{V.XI}
\end{aligned} \tag{A.13}$$

The transport equation for the SGS kinetic energy, τ_{ii} is the following:

$$\begin{aligned}
&\underbrace{\frac{\partial \tau_{ii}}{\partial t}}_{N.VIII} + \underbrace{\frac{\partial \tau_{ii} \overline{u_j}}{\partial x_j}}_{N.IX} + \underbrace{2\nu^{[p]} \frac{\partial}{\partial x_j} \left(\frac{\partial \tau_{iji}^{[p]}}{\partial t} \right)}_{V.XII} + \underbrace{2\nu^{[p]} \frac{\partial}{\partial x_j} \left(\frac{\partial \tau_{iji}^{[p]} \overline{u_k}}{\partial x_k} \right)}_{V.XIII} \underbrace{-2\nu^{[p]} \frac{\partial}{\partial x_j} \left(\overline{C_{ij} \frac{\partial u_i}{\partial t}} - \overline{C_{ij}} \frac{\partial \overline{u_i}}{\partial t} \right)}_{V.XIV} \\
&\underbrace{-2\nu^{[p]} \left(\overline{\frac{\partial u_i}{\partial x_j} \frac{\partial C_{ij}}{\partial t}} - \frac{\partial \overline{u_i}}{\partial x_j} \frac{\partial \overline{C_{ij}}}{\partial t} \right)}_{V.XV} = \underbrace{\frac{\partial}{\partial x_j} \left(\overline{u_i u_i} \cdot \overline{u_j} - \overline{u_i u_i u_j} \right)}_{N.X} + \underbrace{\frac{2}{\rho} \frac{\partial}{\partial x_i} \left(\overline{p} \cdot \overline{u_i} - \overline{p u_i} \right)}_{N.XI} + \underbrace{\frac{\partial}{\partial x_j} \left(\nu^{[s]} \frac{\partial \tau_{ii}}{\partial x_j} \right)}_{N.XII} + \\
&\underbrace{-2\nu^{[s]} \left(\overline{\frac{\partial u_i}{\partial x_j} \frac{\partial u_i}{\partial x_j}} - \frac{\partial \overline{u_i}}{\partial x_j} \frac{\partial \overline{u_i}}{\partial x_j} \right)}_{N.XIII} + \underbrace{2 \frac{\partial \tau_{ij} \overline{u_i}}{\partial x_j}}_{N.XIV} \underbrace{-2\tau_{ij} \overline{S_{ij}}}_{N.XV} + \underbrace{2\nu^{[p]} \frac{\partial}{\partial x_j} \left(\frac{\partial}{\partial x_k} \left(\overline{C_{ij} u_i} \cdot \overline{u_k} - \overline{C_{ij} u_i u_k} \right) \right)}_{V.XVI} +
\end{aligned}$$

$$
\underbrace{+2\nu^{[p]}\frac{\partial}{\partial x_j}\left(\frac{\partial\overline{C_{jk}u_iu_i}}{\partial x_k}-\frac{\partial\overline{C_{ij}}\cdot\overline{u_i}\cdot\overline{u_i}}{\partial x_k}+\frac{\partial\overline{C_{ik}u_ju_i}}{\partial x_k}-\frac{\partial\overline{C_{ik}}\cdot\overline{u_j}\cdot\overline{u_i}}{\partial x_k}\right)}_{V.XVII}
$$

$$
\underbrace{-2\nu^{[p]}\left(\overline{\frac{\partial u_i}{\partial x_j}\frac{\partial C_{jk}u_i}{x_k}}-\frac{\partial\overline{u_i}}{\partial x_j}\frac{\partial\overline{C_{jk}}\cdot\overline{u_i}}{\partial x_k}+\overline{\frac{\partial u_i}{\partial x_j}\frac{C_{ik}u_j}{\partial x_k}}-\frac{\partial\overline{u_i}}{\partial x_j}\frac{\partial\overline{C_{ik}}\cdot\overline{u_j}}{\partial x_k}-\left(\overline{\frac{\partial u_i}{\partial x_j}\frac{\partial C_{ij}u_k}{\partial x_k}}-\frac{\partial\overline{u_i}}{\partial x_j}\frac{\partial\overline{C_{ij}}\cdot\overline{u_k}}{\partial x_k}\right)\right)}_{V.XVIII}+
$$

$$
\underbrace{+2\nu^{[p]}\frac{\partial}{\partial x_j}\left(\frac{\partial}{\partial x_k}\left(\overline{u_i}\left(\tau^{[p]}_{ijk}-\tau^{[p]}_{jki}-\tau^{[p]}_{ikj}\right)\right)\right)}_{V.XIX}\underbrace{-2\nu^{[p]}\frac{\partial}{\partial x_j}\left(\frac{\partial\overline{u_i}}{\partial x_k}\left(\tau^{[p]}_{ijk}-\tau^{[p]}_{jki}\right)-\tau^{[p]}_{ikj}\overline{S_{ik}}\right)}_{V.XX}
$$

$$
\underbrace{-2\nu^{[p]}\frac{\partial\overline{u_i}}{\partial x_j}\frac{\partial}{\partial x_k}\left(\tau^{[p]}_{ijk}-\tau^{[p]}_{jki}-\tau^{[p]}_{ikj}\right)}_{V.XXI}
$$

$$
\underbrace{-2\nu^{[p]}\frac{\partial}{\partial x_j}\left(\overline{\frac{\partial u_i}{\partial x_k}C_{jk}u_i}-\frac{\partial\overline{u_i}}{\partial x_k}\cdot\overline{C_{jk}}\cdot\overline{u_i}+\overline{\frac{\partial u_i}{\partial x_k}C_{ik}u_j}-\frac{\partial\overline{u_i}}{\partial x_k}\overline{C_{ik}}\cdot\overline{u_j}-\left(\overline{\frac{\partial u_i}{\partial x_k}C_{ij}u_k}-\frac{\partial\overline{u_i}}{\partial x_k}\overline{C_{ij}}\cdot\overline{u_k}\right)\right)}_{V.XXII}
$$

$$
\underbrace{-2\nu^{[p]}\frac{\partial}{\partial x_j}\left(\overline{u_iu_i\frac{C_{jk}}{\partial x_k}}-\overline{u_i}\,\overline{u_i\frac{\partial C_{jk}}{\partial x_k}}+\overline{u_iu_j\frac{\partial C_{ik}}{\partial x_k}}-\overline{u_i}\,\overline{u_j\frac{C_{ik}}{\partial x_k}}\right)}_{V.XXIII}+
$$

$$
\underbrace{2\nu^{[p]}\left(\overline{\frac{\partial u_i}{\partial x_j}u_i\frac{\partial C_{jk}}{\partial x_k}}-\frac{\partial\overline{u_i}}{\partial x_j}\overline{u_i\frac{\partial C_{jk}}{\partial x_k}}+\overline{\frac{\partial u_i}{\partial x_j}u_j\frac{\partial C_{ik}}{\partial x_k}}-\frac{\partial\overline{u_i}}{\partial x_j}\overline{u_j\frac{\partial C_{ik}}{\partial x_k}}\right)}_{V.XXIV}
\tag{A.14}
$$

In equations (A.13) and (A.14), the terms that already existed in the Newtonian case are denoted with "N" whereas the new terms, originated by the presence of the polymer, are denoted with "V". It is possible to see that most of the terms that appear due to the presence of polymer additives are, topologically, similar to the classical terms. Terms $V.I$ and $V.II$ account for the local and convective variation of $\overline{C_{ij}}\cdot\overline{u_i}$, respectively, as terms $N.I$ and $N.II$ account for the total (local and convective, respectively) variation of the GS kinetic energy. Terms $V.IV$ and $V.V$ are, respectively, diffusion and dissipation terms similar to $N.IV$ and $N.V$. Terms $V.VI$, $V.VII$ and $V.VIII$ are the only terms (among the terms introduced by the presence of polymer) that account for the interactions between the GS and the SGS. Terms $V.VI$ and $V.VII$ are, topologically, similar to terms $N.VI$ and $N.VII$, respectively. Term $V.VI$ accounts for the diffusion of energy between GS and SGS, whereas term $V.VII$ represents the energy transfer. It is interesting to see that, in viscoelastic turbulence, a new term ($V.VIII$), topologically different from the terms of the Newtonian case, describes the interactions between GS and SGS.

It is important to refer that the meaning of each new term derived in this appendix is not clear, since no further studies were carried out so far. Thus, the comments done in this appendix are not conclusive but introductory. Moreover, there are new terms with no counterpart in the Newtonian case, and for these terms the physical meaning is more difficult to advance.

In equation (A.14), terms $V.XII$ and $V.XIII$ represent, respectively, the local and convective variation of the subgrid-stress polymer tensor. These terms, $V.XII$ and $V.XIII$, are similar to terms $N.VIII$ and $N.IX$, respectively. Term $V.XVI$, similar to $N.X$, is the SGS turbulent transport of $\tau_{ijk}^{[p]}$. The SGS diffusion and dissipation is represented by the terms $V.XVII$ (similar to $N.XII$) and $V.XVIII$ (similar to $N.XIII$), respectively. Terms $V.XIX$, $V.XX$ and $V.XXI$ are the symmetric of the terms $V.VI$, $V.VII$ and $V.VIII$, respectively.

In order to clarify the physical meaning of each term and its relevance for the dynamics of the GS and/or the SGS, these terms (in equations (A.13) and (A.14)) should be analysed in a future work.